Molecular Simulations of Zeolites:
Heterogeneous Systems at Equilibrium and Non-Equilibrium

Sondre Kvalvåg Schnell

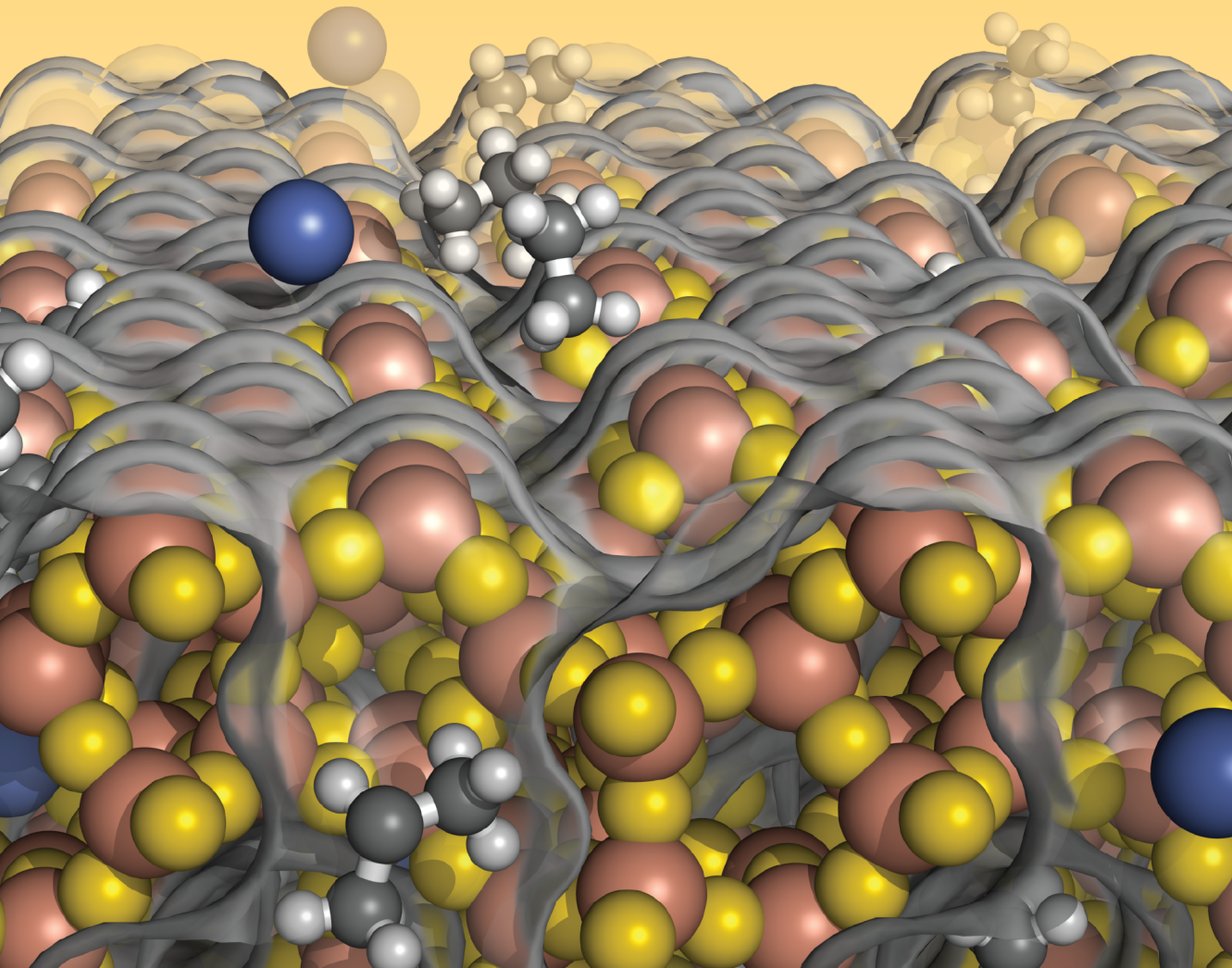

Sondre Kvalvåg Schnell

Molecular Simulations of Zeolites:

Heterogeneous Systems at Equilibrium and Non-Equilibrium

Delft University of Technology

Molecular Simulations of Zeolites: Heterogeneous Systems at Equilibrium and Non-Equilibrium

Proefschrift

ter verkrijging van de graad van doctor
aan de Technische Universiteit Delft,
op gezag van de Rector Magnificus prof. ir. K.C.A.M. Luyben,
voorzitter van het College voor Promoties,
in het openbaar te verdedigen op 1 november 2013 om 12.30 uur

door Sondre Kvalvåg SCHNELL
Master of Science (Sivilingeniør), Norwegian University of Science and Technology, geboren te Kristiansund, Norway.

Dit proefschrift is goedgekeurd door de promotoren:
Prof. Dr. Ir. Thijs J. H. Vlugt
Prof. Dr. Ing. et Dr. techn. Signe Kjelstrup

Samenstelling promotiecommissie:

Rector Magnificus	voorzitter
Prof. Dr. Ir. T.J.H. Vlugt	Promotor, Technische Universiteit Delft
Prof. Dr. Ing. et Dr. techn. S. Kjelstrup	Promotor, Norwegian University of Science and Technology and Technische Universiteit Delft
Prof. Dr. N. van der Vegt	Technische Universität Darmstadt
Prof. Dr. A. E. Rodrigues	Universidade do Porto
Prof. Dr. Ir. B.J. Boersma	Technische Universiteit Delft
Prof. Dr. B. J. Thijsse	Technische Universiteit Delft
Dr. D. Dubbeldam	Universiteit van Amsterdam

This work was sponsored by NWO-CW through an ECHO-grant # 700.58.042, and computational resources through NCF grants MP-213-11, MP-213-12, and MP-213-13.

ISBN: 978-94-6186-211-2
Printed by CPI-Wöhrmann Print Service – Zutphen

'A satisfied customer. We should have him stuffed'

Basil Fawlty

Contents

1 Introduction **1**

1.1 Background 2
1.2 Gas/Solid Surfaces 3
1.3 Non-Equilibrium Thermodynamics for Heterogeneous Systems . . 5
1.4 Molecular Simulation 9
1.5 Outline of This Thesis 12

2 Thermodynamic Properties from Small Scale Fluctuations **15**

2.1 Introduction 16
2.2 Small System Scaling to Obtain Thermodynamic Properties 18
2.2.1 Pure Component Systems 19
2.2.2 Binary and Multicomponent Systems 20
2.3 Systems Studied 22
2.3.1 Homogeneous Systems 22
2.3.2 Heterogeneous System 23
2.4 Results and Discussion 23
2.4.1 Homogeneous Systems 23
2.4.2 Heterogeneous System 29
2.5 Conclusions 32

3 External Surface Adsorption **35**

3.1 Introduction 36
3.2 Methodology 38

3.3 Results and Discussion 41
3.4 Conclusions 45

4 Adsorption of Argon on MFI-Nanosheets 47
4.1 Introduction 48
4.2 Excess Adsorption and Surface Excess Adsorption 53
4.3 Simulations 54
4.4 Results and Discussion 56
4.4.1 Adsorption Isotherms 56
4.4.2 Argon Density Profiles 59
4.4.3 Surface Excess Adsorption 60
4.5 Conclusions 62

5 Thermal Conductivity in Zeolites 63
5.1 Introduction 64
5.1.1 Thermal Conductivities from Experiments 65
5.1.2 Modelling 66
5.1.3 NEMD Approach 67
5.1.4 Outline 68
5.2 NEMD Simulation Method 68
5.3 Simulation Technique 71
5.4 Results and Discussion 72
5.4.1 Finite-size Effects, and Size Effect of Hot/Cold Zone 72
5.4.2 Thermal Conductivity 76
5.4.3 Thermal Conductivity for Zeolites with Adsorbed Molecules 79
5.4.4 Framework Density 80
5.5 Conclusions 81

6 Non-Equilibrium Transport Across a Zeolite Membrane 83
6.1 Introduction 84
6.1.1 A Zeolite Membrane in Equilibrium with a Gas 85
6.1.2 Transport Across a Heterogeneous System 87
6.2 Fluxes and Forces from the Second Law and Transport Coefficients 89
6.2.1 Fluxes and Forces from the Second Law 89

6.2.2 Transport Coefficients and Driving Forces 92
6.3 Case Studies of Transport Across the Zeolite Membrane 92
6.3.1 Solution Procedure 94
6.3.2 Results and Discussion 97
6.4 Conclusions 100

References **101**

Summary **123**

Samenvatting **127**

Curriculum Vitae **131**

Publications by the Author **133**

Acknowledgement **135**

Chapter 1

Introduction

The topic of this thesis is to provide equilibrium and non-equilibrium thermodynamic descriptions of heterogeneous systems, using the zeolite silicalite-1 (MFI-type) as an example. Well known molecular simulation techniques are used and novel techniques are developed for the purpose of finding transport coefficients and heats of adsorption for binary homogeneous mixtures and adsorbed molecules in nanoporous frameworks. A new method for precise and fast computation of equilibrium properties in terms of Kirkwood-Buff coefficients is developed. Equilibrium thermodynamic properties and transport properties are determined for various mixtures at different conditions. This can be used to model surface adsorption and membrane transport. Accurate models for describing transport of heat and mass across zeolite membranes are of paramount importance for optimizing separation performance of a membrane. In this Chapter, we first briefly review the status of research on zeolite surfaces in Section 1.1. We also define the concept of a surface as it will be used here (Section 1.2). The essence of non-equilibrium thermodynamics is recapitulated in Section 1.3. Molecular simulations is an excellent tool to obtain a molecular insight in transport and adsorption processes. The basics of simulation methods is reviewed in Section 1.4. The outline of this thesis is presented in Section 1.5.

1.1 Background

Zeolites are crystalline materials, with pores, channels, and cages at a molecular length scale. The building blocks of zeolites, silicon and oxygen, can be combined to form many frameworks with different adsorption and separation properties. The enormous amount of framework configurations [1] makes zeolites interesting, especially for separation [2–10] and catalysis [3, 11–13]. Recent work on small molecules adsorbed in zeolites and metal-organic frameworks (MOFs) is for example described in the book of Kärger, Ruthven, and Theodorou [14]. Kärger *et al.* [14] explain in detail the experimental methods used to measure diffusion of guest molecules in nanoporous frameworks. These authors also explain how computer simulation techniques can be used to study diffusion in theses nanoporous materials.

The huge amount of possible frameworks (2.7 million theoretical frameworks as identified by Deen *et al.* [1]), and the fact that only a few of these have been synthesized (approximately 240 frameworks [15]) makes it interesting to computationally study the adsorption and separation properties of zeolites. Zeolites are viable candidates for next-generation carbon capture and sequestration materials [6, 16–19]. Research on transport and separation properties of zeolites have been a hot research topic for some time now. Some of the recent developments can be found in Refs. [2, 10, 11, 20–32].

The external gas/zeolite interface can be a limiting factor for transport properties and the selectivity of zeolite structures [33–35]. A molecule must cross a free-energy barrier going from the gas and into the zeolite [36]. As it becomes possible to synthesize thinner and thinner membranes [37] (the zeolite layer in the membrane is around 3 μm in the work of Shu *et al.* [4]), the transport properties and selective properties of the external gas/zeolite interface will become more important. Choi *et al.* [21] synthesized layers of unit cell thick MFI-type zeolite nanosheets. Zeolite nanosheets could be considered as ultra thin membranes with enhanced transport properties, and low transport resistance. A zeolite nanosheet can be regarded as composed of two surfaces, and there is no bulk zeolite between these surfaces. The surfaces are then completely dominating the transport properties of the zeolite. Although zeolites have been systematically studied for decades, the properties of the external surface have not received much attention. In this thesis we have studied the external zeolite surface. In Section 1.2 we will describe the definition of the

surface used in this work.

The use of simulation tools can be a viable option for studying the transport on external surfaces. So far, only Inzoli *et al.* [35, 38, 39] have used non-equilibrium thermodynamics to describe the coupled transport of heat and mass at the external surface of a zeolite. The theory of non-equilibrium thermodynamics has been applied to describe gas-liquid interfaces [40–45] as well as single component transport across a silicalite-1 zeolite external surface [35, 42–45]. Computer simulations have provided an excellent tool to study transport, and develop theories on transport phenomena. However, few systems have been thoroughly investigated, and few transport coefficients have been determined for transport across the external surface. In this thesis, we present new methods related to computation of equilibrium and non-equilibrium states in zeolites. Special emphasis is put on the external surface of zeolites, and how the surface can influence the transport of molecules from a bulk-phase into the zeolite, and vice versa.

1.2 Gas/Solid Surfaces

In this thesis, we consider the surface as a thermodynamic system separate from the bulk phases, *i.e.* the zeolite phase, and the gas phase. We will use the term interface and surface interchangeably. One distinguishes normally between the internal and external surfaces of a zeolite. In literature, surface adsorption is usually used to describe adsorption on the inner part of the zeolite, that is adsorption in channels, cages, and intersections. The external surface exposes the crystal to the gas-phase. We shall study both, but will denote the inner part of the zeolite as bulk-zeolite, and the surface facing a gas-phase as the external surface.

To have a thermodynamic description of the external surface, we follow the definition proposed by Gibbs [46]. Gibbs described the dividing surface as: 'a geometrical plane, going through points in the interfacial region, similarly situated with respect to conditions of adjacent matter' [46]. From a macroscopic point of view, the surface is infinitesimally thin but at a molecular scale, there is a thickness of molecular order. Since intensive variables change with the position in the surface, the natural choice of variables for the external surface is excess variables [47]. The excess variables, like density and enthalpy, are determined by integrating the

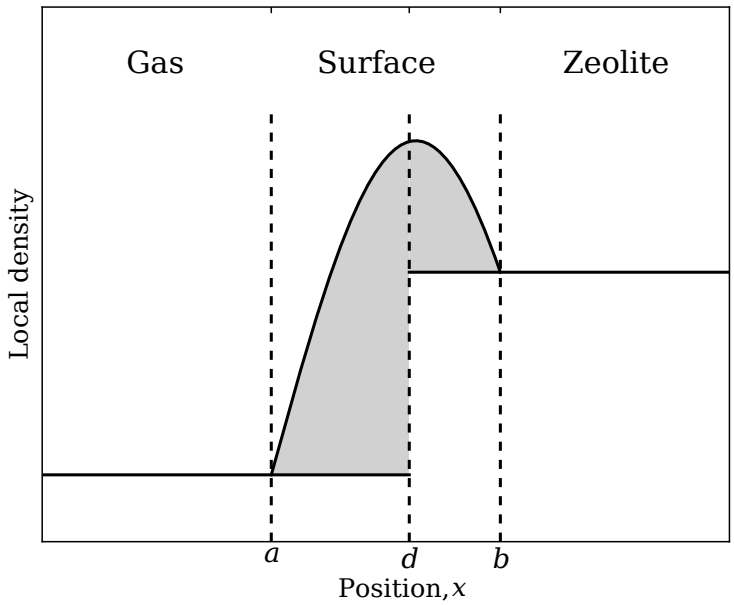

Figure 1.1: Typical density profile across an external surface of a zeolite. The surface excess density (grey area) is found by integrating the density profile from a to b, while subtracting the concentration in the adjoining bulk-phase. The dividing surface d is usually placed at the crystalline surface, while the position of the limits a and b can be selected arbitrarily as long as they are in the pure bulk-phase.

variable profile across the external surface, from the bulk-phase on one side of the surface to the bulk-phase on the other side of the surface. The position of the external surface, and the actual extent of the surface is then less important, and it is no longer necessary to take the actual thickness of the surface into account. This is illustrated in Fig. 1.1 for the excess density, but the method is generally applicable to other quantities.

Thermodynamic properties, *e.g.* density and partial molar enthalpy, can vary significantly across the surface on a molecular scale [47]. A typical density profile is shown schematically in Fig. 1.1. This shows how the density varies along one direction in the system. It is qualitatively close to the density profiles as seen for

gas-liquid interfaces, see *e.g.* Røsjorde *et al.* [40]. When the surface is exposed to gradients in temperature and chemical potential we assume that the surface or part of the surface is in local equilibrium [48]. Local equilibrium means that for a sufficiently small volume element the classical equilibrium thermodynamic equations apply [47]. Kjelstrup and Bedeaux [47] discuss local equilibrium in more detail, and Savin *et al.* [48] discuss the gauge invariance of the dividing surface, and the local equilibrium assumption for surfaces in binary systems. In this thesis local equilibrium is assumed to hold for all the non-equilibrium systems studied. In Section 1.3 we will describe how non-equilibrium thermodynamics can be used to describe transport in heterogeneous systems [47]. The Gibbs definition of the surface, and the assumption of local equilibrium will be central in this description.

The external zeolite surface has to a large extent eluded systematic study. The fact that is it a small part of the zeolite, just a few nano meters thick, makes it difficult to measure properties of the surface in experiments. For transport in thick membranes, the surface resistance will be a minor contribution to the transport resistance in the membrane itself, and can safely be neglected [14]. For zeolite nanosheet applications [21, 49] this is no longer true, and the surface can be a significant part of the resistance to heat and mass transport in the system [14]. The surface has a contribution to resistance towards heat and mass transport, *i.e.* independent of the membrane thickness.

1.3 Non-Equilibrium Thermodynamics for Heterogeneous Systems

Non-equilibrium thermodynamics is a systematic theory for describing transport (*e.g.* heat, mass, and/or charge) under non-equilibrium conditions. From the second law of thermodynamics, it follows that the change in entropy for an isolated system under non-equilibrium conditions must be larger than zero [47]. The local entropy production of a system can be described as:

$$\sigma = \sum_i J_i X_i \geq 0, \tag{1.1}$$

where σ is the entropy production, J_i is a flux, *i.e.* a flux of heat, mass, or charge, and X_i is the conjugate force, *e.g.* a gradient in inverse temperature, chemical potential,

or an electric field. The units of σ are therefore J K^{-1} s^{-1}. For the remainder of this work, we will restrict ourself to discussing fluxes of heat and mass, and forces being gradients in inverse temperature and chemical potential. Gradients in temperature and chemical potential are very common, and are a prerequisite for transport. One important aspect here, is that gradients in temperature can result in a flux of mass, the same way a gradient in chemical potential can result in a flux of heat [47, 50]. In the theory of non-equilibrium thermodynamics, each flux is a linear combination of all forces [47]:

$$J_i = \sum_j L_{ij} X_j, \tag{1.2}$$

where L_{ij} are the phenomenological coefficients. If we look at a system with a heat flux J_q, and a mass flux J_m (and two corresponding driving forces, X_q, and X_m) we end up with:

$$J_q = L_{11} X_q + L_{12} X_m, \tag{1.3}$$
$$J_m = L_{21} X_q + L_{22} X_m, \tag{1.4}$$

where X_q is the gradient in inverse temperature $X_q = \nabla \frac{1}{T}$, resulting in a heat-flux, and X_m is a gradient in chemical potential at constant temperature $X_m = \nabla \mu_{T,p}$, resulting in a mass-flux. The diagonal phenomenological coefficients (L_{11} and L_{22}) can be directly related to the diffusivity and thermal conductivity, familiar from the normal Fick's and Fourier's law [47, 50]. Gradients in chemical potential will relate the phenomenological coefficients to the Maxwell-Stefan coefficients [47]. Fick's and Maxwell-Stefan diffusivities describe the same phenomena: transport of mass due to a gradient in concentration or chemical potential [51, 52].

The off-diagonal coefficients (L_{12} and L_{21}) are the coupling terms, and describe the induced heat flux and mass flux by a gradient in chemical potential and temperature respectively. These effects are typically referred to as Soret effect (mass flux induced by a temperature gradient) and Dufour effect (heat flux induced by a chemical potential gradient) [47, 53–55]. Usually the coupling is small [50], but there are cases where it can be crucial [35, 54]. The coupling can be significant at interfaces [35, 47].

The off-diagonal coefficients have been shown to be symmetric:

$$L_{ij} = L_{ji}. \tag{1.5}$$

This is known as the Onsager Reciprocal relations [47, 50, 56, 57]. It was shown by Lars Onsager [56, 57] in his 1931 papers: 'Reciprocal Relations in Irreversible Processes' (I and II), at the same time establishing the field of non-equilibrium thermodynamics. The Onsager Reciprocal relations have been verified computationally by Xu *et al.* [58] using non-equilibrium molecular dynamics simulations. Building on the work of Onsager, de Groot and Mazur [50] presented a systematic way to apply the theory of non-equilibrium thermodynamics, thereby the transport of heat, mass, charge, and the coupling between these in *homogeneous* systems under non-equilibrium conditions.

A description of non-equilibrium thermodynamics for *heterogeneous* systems is necessary to describe more complex systems, and this is available in the recent book of Kjelstrup and Bedeaux: 'Non-equilibrium thermodynamics of Heterogeneous Systems' (2008) [47]. Kjelstrup and Bedeaux are building on the work of de Groot and Mazur, deriving the equations for transport in non-equilibrium systems, with emphasis on heterogeneous systems. The surface definition favoured by Kjelstrup and Bedeaux is the famous one described by Gibbs [46] (see Section 1.2). Describing transport across the surface, Kjelstrup and Bedeaux consider the surface as a thermodynamic system, and describe fluxes going into and out of the surface. This is shown schematically in Fig. 1.2. The non-equilibrium thermodynamics approach for heterogeneous systems has been studied using computer simulations for several different systems. Gradients in temperature and chemical potential have been applied to systems like: Lennard-Jones (LJ) particles [44, 58–60], *n*-octance [42], and *n*-butane in silicalite-1 zeolite [35, 61]. Even with the large temperature- and chemical potential gradients used in these works, the assumption of local equilibrium was found to hold for the surface, and phenomenological coefficients L_{ij} were determined. The diagonal coefficients can be compared to the thermal conductivity (Fourier's law), and diffusivity (Fick's law) in each case. The off-diagonal coefficients can be determined in several ways, and be compared directly using the Onsager Reciprocal relations.

Using the approach of Kjelstrup and Bedeaux [47], one can show that the excess entropy production for transport of heat and mass across a heterogeneous surface

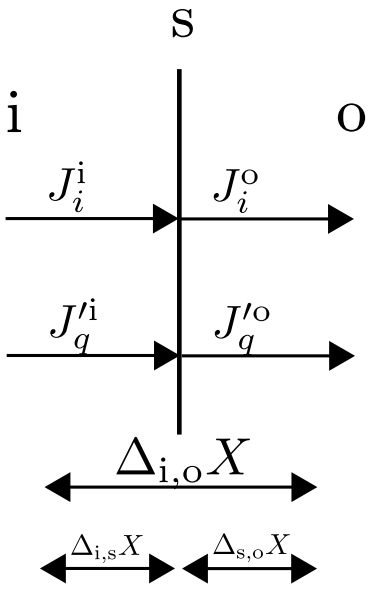

Figure 1.2: Notation used for the surface (s). i and o are denoting positions in the bulk phases next to the surface, so the notation $\Delta_{i,o}X$ is the difference $X_{\mathrm{o}} - X_{\mathrm{i}}$, where X_i is the inverse temperature or chemical potential. J_i is the mass flux of component i, and J_q' is the measurable heat flux. At steady-state the mass-flux is constant, $J_i^{i,s} = J_i^{s,o}$, due to conservation of mass, while the measurable heat flux is in general not.

can be described by:

$$\begin{aligned}\sigma^s = {} & J_q'^{\mathrm{i}}\Delta_{\mathrm{i,s}}\left(\frac{1}{T}\right) + J_q'^{\mathrm{o}}\Delta_{\mathrm{s,o}}\left(\frac{1}{T}\right) \\ & + J_m^{\mathrm{i}}\left(-\frac{1}{T^{\mathrm{s}}}\Delta_{\mathrm{i,s}}\mu_{m,T}\left(T^{\mathrm{s}}\right)\right) + J_m^{\mathrm{o}}\left(-\frac{1}{T^{\mathrm{s}}}\Delta_{\mathrm{o,s}}\mu_{m,T}\left(T^{\mathrm{s}}\right)\right),\end{aligned} \tag{1.6}$$

where the superscript s indicates that a variable is taken for the surface, i and o refer to the left and right side of the surface respectively (see Fig. 1.2), σ^s is the excess entropy production with units $\mathrm{J\,K^{-1}\,s^{-1}\,m^{-2}}$, J_q' is the measurable heat flux and J_i is the mass-flux of the ith component, T is the absolute temperature, and μ is the chemical potential. Equation (1.6) consists of the product of the conjugate flux-force pairs for the two parts of the surface. We also refer to Fig. 1.2 for a schematic representation of the notation used here. Note that for the surface we are looking at *differences*, and the notation $\Delta_{i,s}X = X_s - X_i$ is the same as used by Kjelstrup and Bedeaux [47].

One can choose between two different heat-fluxes: the measurable heat flux J_q'

and the total heat flux J_q. The measurable heat flux is the heat flux measured in experiments, not taking into account the latent heat carried by transported molecules. The total heat flux is determined directly in molecular simulations. Under steady-state conditions, the total heat flux is constant, while the measurable heat flux is not. The total heat flux can be related to the measurable heat flux through:

$$J_q = J'_q + \sum_{i=1}^{n} H_i J_i, \tag{1.7}$$

where H_i is the partial molar enthalpy of component i. The sum is over all components in the system. The difference in partial molar enthalpies between the different sides of the surface (*i.e.* the heat of adsorption [35]) indicates that there can be large thermal effects during adsorption on the external surface [35]. Whether measurable heat flux or total heat flux is preferred depends on the system studied, and the method used to determine the heat flux. Total heat flux is preferred in simulation and modelling approaches, while the measurable heat flux is preferred in experimental studies.

1.4 Molecular Simulation

In this thesis, classical molecular simulations are used to calculate macroscopic properties from the interaction between individual molecules. In classical simulations these interactions between atoms and molecules are described by a so-called force field, *i.e.* a functional form of their interaction energy as a function of their positions, and a corresponding set of parameters. This force field is often a pair-potential, defining the interaction energy and force between two particle centres. One of the most common functional form is the Lennard-Jones (LJ) pair-potential [62]:

$$U(r) = 4\varepsilon\left[\left(\frac{\sigma}{r}\right)^{12} - \left(\frac{\sigma}{r}\right)^{6}\right], \tag{1.8}$$

where U is the particle-particle interaction energy, σ is the distance where the interaction energy is zero, and ε is the depth of the potential well, *i.e.* the minimum energy between a pair of particles, r is the distance between the centres of the particles. The total potential energy is the sum of all the pair-interactions between all

particle pairs in the system. In addition, for molecules one must account for energy terms due to interactions within a molecule: bond stretching, bending, torsion, and intra molecular Lennard-Jones interactions. Polar systems require the use of long range electrostatic interactions. The force field parameters are usually fitted using vapour-liquid equilibrium data [63–67], but also other criteria can be used in the fitting procedure [68, 69]. Usually, periodic boundary conditions are used to mimic infinitely large systems [62, 70]. Periodic boundary conditions means that a particle leaving the simulation box on one side, will enter the box on the opposite side. The simulation box will appear to be replicated an infinite amount of times in each direction.

Molecular properties at the microscopic scale (the simulated system) can be related to macroscopic properties (in the thermodynamic limit) by averaging over trajectories. Equilibrium properties like heat of adsorption, heat capacity, and adsorption isotherms can be computed, as well as transport properties, like diffusion coefficients, and thermal conductivities [62, 71–74]. There are several different simulation methods to calculate macroscopic properties from microscopic interactions, but in this case we will consider two main types: Molecular Dynamics (MD) and Monte Carlo (MC). Of these, Molecular Dynamics is the conceptually easiest method.

In a MD simulation, the system is progressed in time by integrating Newton's second law of motion [62]:

$$\frac{\mathbf{F}_i}{m_i} = \frac{\mathrm{d}^2 \mathbf{x}_i}{\mathrm{d}\, t^2}, \tag{1.9}$$

where $\mathbf{F}_i$ is the force on particle i, m_i is the mass of particle i, $\mathbf{x}_i$ is the position for particle i, and t is the time. The force is calculated using the derivative of the interaction potential ($\mathrm{d}\, U / \mathrm{d}\, \mathbf{x}_i$), and the system is progressed using an integration scheme, usually Verlet, Velocity-Verlet, or Leap-frog [62]. By repeated integration, the system progresses through time, and average properties of the system can be calculated from the trajectory of all the atoms/molecules in the system. Within the numerical accuracy of the computer, the total and kinetic energy of the system should be conserved. However, the evolution of the system can be confined, typically using thermostats or barostats. If a thermostat is applied, the total energy of the system is *not* conserved. MD simulations can be used to calculate transport

properties, *e.g.* diffusion coefficients [75], since the dynamics of the particles in the system can be related to macroscopic transport properties. A MD simulation is usually *deterministic*, so a trajectory can be generated over and over based on only the initial positions and velocity. However, minor changes in the initial configuration can result in widely different final configuration. This is known as Lyapunov instability [62, 76]. The Lyapunov instability makes the microscopic trajectory deviate from the 'real' trajectory. The importance of this deviation remains an open question, but it has been shown that simulating representative trajectories instead of actual ones is usually sufficient [62, 76]. For a thorough introduction to molecular simulations, we refer to some excellent textbooks on the subject [62, 70, 77, 78].

The other common simulation method we consider is Monte Carlo (MC simulations. MC simulations are conceptually more difficult than MD simulations. Where MD simulations look at the natural time evolution of the system, a MC simulation is a numerical method to study a partition function Q [62, 79]. The partition function describes the properties of a system in equilibrium, and can be a function of temperature T, volume V, and number of particles N. $Q(NVT)$ is called the canonical partition function. Another commonly used partition function is the grand-canonical partition function, with constant chemical potential μ, volume V, and temperature$T$, $Q(\mu VT)$ [79]. Even for a very small system, the number of possible internal configurations very quickly goes to infinity (or just an extremely large number). Since only some of these possible configurations are statistically important, *i.e.*, have a non-zero contribution to the partition function, MC simulations generate weighted configurations which have a probability proportional to its statistical weight for a given partition function. This is called *importance sampling*, and was originally proposed by Metropolis *et al.* [80]. By generating many of these configurations, ensemble averages follow. The ensemble averages are related to the macroscopic properties of the system, constrained by the given partition function.

Even if computational power is increasing exponentially [81], it is still important to develop new methods, and improve on the already existing computational methods. One of the properties interesting in transport studies, are the Kirkwood-Buff (KB) coefficients. In their 1951 paper, Kirkwood and Buff [82] showed how density fluctuations in the μVT ensemble are related to pair-correlation functions in the grand-canonical ensemble. The KB coefficients can be used to calculate activity coefficients, partial molar volumes, and the isothermal compressibility [83].

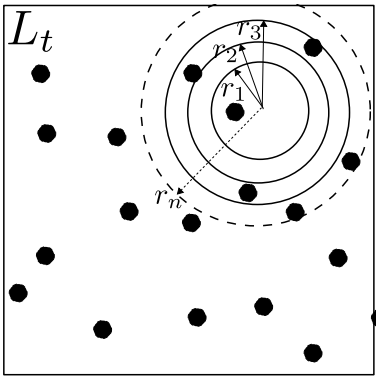

Figure 1.3: Sampling of small subvolumes in a large simulation box. The whole simulation box has sides L_t. Embedding successive spherical subvolumes in the larger box, one can extrapolate to the thermodynamic limit, *i.e.* an infinitely large system. The small subvolumes have radius r, where $r \leq \frac{1}{2}L_t$.

The grand-canonical ensemble can however be quite difficult to simulate for dense systems [62, 84–86], so a very common approximation is to use the pair-correlation function obtained from different ensembles. This is however not a good approximation [87]. In Chapter 2, we show a different way to compute the KB coefficients that is faster and more accurate, especially for dense phases or nanoporous materials. This new method uses a finite-size scaling approach by studying systems with different length scales, and extrapolating to the thermodynamic limit, see also Fig. 1.3 and the caption for a short explanation how grand-canonical ensembles can be determined from small systems.

1.5 Outline of This Thesis

The overall aim of this thesis is to contribute to the description and understanding of heterogeneous zeolite systems at equilibrium and non-equilibrium conditions. In more detail this means:

- to develop an efficient computational method to relate Maxwell-Stefan and Fick diffusivities, as well as to compute heats of adsorption in nanoporous materials.

- to develop ways to model mixture adsorption at an external zeolite surface.

- to investigate the transport of heat in filled and empty nanoporous materials using non-equilibrium molecular dynamics simulations.
- to simulate the transport of heat and mass into and across an external membrane surface, and to provide a description for this using non-equilibrium thermodynamics.

In Chapter 2, we investigate finite-size effects of small subsystems, *i.e.* a small part of a larger simulation box, and how KB integrals can be calculated for binary systems using a novel method. Kirkwood-Buff integrals can be used to relate Maxwell-Stefan and Fick diffusivities, determine partial molar volumes, or calculate the isothermal compressibility. KB integrals are calculated using a finite-size scaling method, by sampling small subvolumes, and accounting for non-periodic boundaries of the small subsystems, see also Fig. 1.3. This method is applied for both isotropic liquids, and for argon in silicalite-1 zeolite. We find the small system scaling method to be an efficient alternative method to determine KB integrals, avoiding the problem with convergence of pair-correlation functions, and avoiding performing grand-canonical simulations, as discussed in Section 1.4. The method allows calculation of properties associated with the grand-canonical ensemble directly from molecular dynamics simulations.

The adsorption of binary mixtures on the external surface of silicalite-1 zeolite is investigated in Chapter 3. Using the Ideal Adsorbed Solution Theory (IAST) for ethane and propane, the composition of ethane/propane mixtures adsorbed on surfaces can be determined. The surface is defined using the Gibbs definition, like described in Section 1.2. We find that IAST describes the adsorption for pressures below condensation for either of the two components. The IAST is able to describe adsorption on the external surface of silicalite-1 zeolite, indicating that the adsorption layer is in fact an ideal adsorbed solution.

Zeolite nanosheets are an alternative way to create zeolites with mesopore characteristics. In Chapter 4 we study the adsorption of argon on silicalite-1 zeolite, using experiments and simulations. The adsorption on the external zeolite surface is determined using the Gibbs definition. We find that the excess adsorption on the surface is negative, indicating a barrier for mass transport at lower pressures. The experiments and simulations have comparable adsorption isotherms for adsorption on zeolite nanosheets.

In Chapter 5, we investigated the transport of heat in zeolite frameworks. By using non-equilibrium molecular dynamics simulations to induce a temperature gradient in the system, we can directly calculate the thermal conductivity of the material. We found there to be very different thermal conductivity in different crystallographic directions in the crystal, and that non-equilibrium molecular dynamics simulations can be an efficient method to determine these properties. The thermal conductivity is found to be almost independent of the loading of guest molecules in the zeolite framework.

Finally, in Chapter 6, a non-equilibrium model for transport of heat and mass in a zeolite membrane was investigated using coefficients for the surface resistance, and coupling of heat and mass transfer. These coefficients were previously determined from non-equilibrium molecular dynamics simulations [35]. The model itself is computationally cheap, and makes it possible to quickly test several operating conditions for a zeolite membrane. The model is based on non-equilibrium thermodynamics for heterogeneous systems (see Sec. 1.3). We find the surface effects to be significant. The coupling of heat and mass transfer on the surface of the zeolite indicate that for thin membranes this can be a significant contribution to the transport of heat and mass across the membrane. The non-equilibrium model shows that heating the permeate side of the membrane can increase the transport across the zeolite membrane.

This work is the next necessary step in determining the resistances to heat and mass transfer at the external surface of silicalite-1 zeolite, and developing the tools necessary for describing the transport across external surfaces. The long term goal is to develop non-equilibrium thermodynamics to be the favoured method for studying external surfaces, and for modelling the transport of heat and mass in nanoporous materials. The choice of molecular simulations for determining transport coefficients is a flexible and efficient tool for this.

Chapter 2

Thermodynamic Properties from Small Scale Fluctuations

This Chapter is based on the paper: S. K. Schnell, X. Liu, J.-M. Simon, A. Bardow, D. Bedeaux, T. J. H. Vlugt, and S. Kjelstrup: 'Calculating Thermodynamic Properties from Fluctuations at Small Scales', J. Phys. Chem. B., 2011, vol. 115, pp 10911–10918.

Abstract

We show how density- and energy fluctuations of small non-periodic systems embedded in a reservoir can be used to determine macroscopic thermodynamic properties like the molar enthalpy and the thermodynamic correction factor. For mixtures, the same formalism leads to a very convenient method to obtain so-called Total Correlation Function Integrals, also often referred to as Kirkwood-Buff integrals. Using finite size scaling, the properties obtained for small systems can be extrapolated to the macroscopic system limit provided that the system is sufficiently far from the critical point. As derived in our previous work, Ref. [71], the finite size scaling is significant and depends on $1/L$, where L is the length of the small system in one dimension. By considering a reservoir with an ensemble of embedded small systems, the scaling arising from surface effects can be used to determine properties for macroscopic systems by extrapolation. We demonstrate this method for the

WCA- and LJ-fluids, as well a for a heterogeneous system, *i.e.* argon adsorbed in silicalite-1 zeolite.

2.1 Introduction

Until recently, thermodynamics of nano-scale systems has not received much attention. The problem when studying these systems is the small scale. Systems at the nanometer scale are difficult to handle experimentally, and so far the thermodynamics of such small systems has not been the focus of investigations in nanoscience. It is important to note that small systems are strongly influenced by surface effects, which cannot be neglected [47]. In principle, these surface effects could be exploited in practical applications or theory/simulations. With this in mind, it becomes important to find a consistent framework describing the thermodynamics of small systems. A theoretical formulation of thermodynamics of small systems is for example given by Hill [88]. The crucial difference between small systems and macroscopic systems is that the enthalpy and Gibbs energy are no longer extensive. Therefore, thermodynamic properties obtained for small systems can not be directly compared to thermodynamic properties of macroscopic systems.

In a recent paper [71], we investigated the finite size scaling of small non-periodic systems embedded in a large periodic reservoir that itself is simulated in the grand-canonical ensemble. These small non-periodic systems can exchange particles and energy with the reservoir, similar to a system in the grand-canonical ensemble. Based on the formalism of Hill [88], we found that thermodynamic properties attributed to the small system have a finite size scaling proportional to $1/L$, L being the length of the system in one dimension. The crucial difference with the more conventional finite-size scaling [89] is that an effective surface energy needs to be added to account for the different boundary conditions of small periodic- and non-periodic systems [71]. The predicted $1/L$ scaling was confirmed using Monte Carlo (MC) simulations in which small systems were embedded in a large simulation box, where the large simulation box itself was kept in the grand-canonical (μVT) ensemble. We determined the molar enthalpy h and the thermodynamic correction factor Γ for small homogeneous systems. The molar enthalpy h is of particular interest when studying adsorption properties [90]. The thermodynamic correction

factor Γ for a single-component system is defined by $1/\Gamma = k_B T \left(\partial \ln \overline{N}/\partial \mu\right)_{T,V}$ in which $\overline{N}$ is the average number of particles and μ is the chemical potential. For mixtures, Γ is related to deviations from ideal mixture behaviour and this quantity is commonly used to relate Fick and Maxwell-Stefan diffusivities [91, 92]. By integrating the thermodynamic correction factor Γ over the chemical potential, the adsorption isotherm (number of molecules as a function of the chemical potential) can be obtained [93]. This is applicable when studying the adsorption of small guest molecules in microporous materials such as zeolites or metal-organic frameworks (MOFs) [66].

The process of embedding a small system inside a large reservoir is shown in Fig. 2.1. The large system with sides L_t (in each dimension) is simulated with periodic boundary conditions. Several small systems embedded in the reservoir (denoted by L_{n-1}, L_n, and L_{n+1}) can exchange energy and particles with the large reservoir. When the large system L_t is in the grand-canonical ensemble, the small systems will be too. If the reservoir is in another ensemble (*e.g.* NVT or NPT), the small systems are only in the grand-canonical ensemble when $L_n \ll L_t$. By considering the scaling of small system properties with the size of the small system, we are able to extract macroscopic thermodynamic properties. In the present study, we show that this method is very efficient for obtaining Total Correlation Function Integrals, also referred to as Kirkwood-Buff (KB) integrals [82]. Partial molar volumes, the compressibility and partial derivatives of activity coefficients can be obtained from single Molecular Dynamics (MD) simulations by computing KB integrals. It is important to note that in the thermodynamic limit the choice of ensemble for the large reservoir is irrelevant [62]. Thus, our method provides a unique way of accessing the grand-canonical ensemble without having to rely on particle insertions and deletions, which can be extremely inefficient for dense systems [62, 86]. Sufficiently large systems with periodic boundary conditions simulated in the grand-canonical ensemble [62] were used to obtain reference values for thermodynamic properties in the thermodynamic limit.

The remainder of this chapter is organized as follows: in Section 2.2 we show how various thermodynamic properties can be computed using the proposed scaling. In Section 2.3, we describe the simulation method, as well as the systems that were studied in this work. Results for homogeneous and inhomogeneous systems

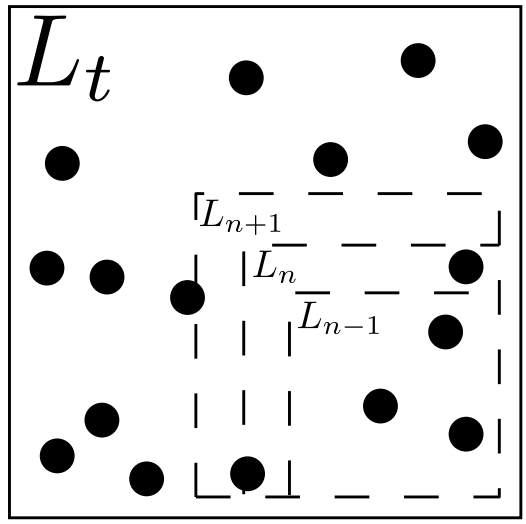

Figure 2.1: Sampling of small non-periodic systems in a (periodic) simulation box (reservoir). The reservoir itself has sides of L_t in each dimension. We embed a small system by randomly placing subvolumes of size L_{n-1}^d, where d is the dimensions of the system ($d = 3$ for all cases in this work). By systematically increasing the size of the subvolume (L_n, L_{n+1}), macroscopic thermodynamic properties can be obtained.

(*i.e.* argon adsorbed in silicalite-1) are shown in Section 2.4, and in Section 2.5 our findings are summarized.

2.2 Small System Scaling to Obtain Thermodynamic Properties

We consider a d-dimensional small system as a subvolume of a larger system (reservoir), see Fig. 2.1. The sizes of these systems in one dimension are denoted by L_n and L_t, respectively. The small system and the reservoir can exchange energy and particles. As the small system shares a surface with the reservoir, an effective surface energy $E^s(\mu, T)$ needs to be taken into account in a thermodynamic description of the small system. This effective surface energy originates from the difference between a small non-periodic system and a system with periodic boundary conditions [71]. Using the theory of Hill [88], we previously derived the following equations for the scaling of thermodynamic properties of embedded one-component

small systems [71]:

$$\begin{aligned}\frac{1}{\Gamma} &= 1 + \frac{2d\Lambda}{L}\left[\frac{\partial E^s}{\partial \mu}\left(1 + \frac{\partial E^s}{\partial \mu}\right) + \frac{\partial^2 E^s}{\beta \partial \mu^2}\right]\exp\left(\beta E^s\right) \\ &= \frac{1}{\Gamma_\infty} + \frac{C'}{L}, \qquad (2.1)\\ \overline{h} &= \frac{\overline{H}}{V} = \left(1 + \frac{d}{2}\right) k_B T \Lambda^{-d} \exp\left(\beta\mu\right) \\ &\quad + 2d\left(\frac{d+1}{2} k_B T - E^s + T\frac{\partial E^s}{\partial T} + \mu\frac{\partial E^s}{\partial \mu}\right) L^{-1}\Lambda^{1-d}\exp\left(\beta\left(E^s + \mu\right)\right) \\ &= h_\infty + \frac{B'}{L}, \qquad (2.2)\end{aligned}$$

where Γ is the thermodynamic correction factor, $\overline{h}$ is the enthalpy density, L is the length of the system in one dimension, and B' and C' are constants that do not depend on L. The subscript ∞ denotes macroscopic properties. In addition, we have $\beta = 1/k_B T$, where k_B is the Boltzmann constant, T is the absolute temperature, μ is the chemical potential, $\overline{H}$ is the average enthalpy, V is the volume, and Λ is the mean thermal de Broglie wavelength. Eq. (2.1) and (2.2) are independent of the dimensionality of the system when we are using L instead of the volume ($L = V^{1/d}$, where d is the dimensionality).

2.2.1 Pure Component Systems

The thermodynamic correction factor and the enthalpy follow from density and energy fluctuations in the grand-canonical ensemble. For single component systems, these can be described as [92, 94]:

$$\frac{1}{\Gamma} = k_B T\left(\frac{\partial \ln \overline{N}}{\partial \mu}\right)_{T,V} = \frac{\langle N^2\rangle - \langle N\rangle^2}{\langle N\rangle}, \qquad (2.3)$$

$$h = -\frac{\langle UN\rangle - \langle U\rangle\langle N\rangle}{\langle N^2\rangle - \langle N\rangle^2}, \qquad (2.4)$$

where the brackets $\langle\cdots\rangle$ denote an ensemble average in the grand-canonical ensemble, N is the number of particles, U is the potential energy, and h is the enthalpy

density. The molar energy is proportional to the enthalpy density. For homogeneous systems, the molar enthalpy is used, while for inhomogeneous systems (*e.g.* argon in silicalite-1) the molar isosteric heat of adsorption $q_{st}^{\star}$ can be obtained directly from h [94]. The isosteric heat of adsorption of argon is defined as the enthalpy change when argon is adsorbed from the gas phase into the host structure [90, 94].

2.2.2 Binary and Multicomponent Systems

Thermodynamic properties of mixtures can be obtained from Total Function Correlation Integrals, also referred to as Kirkwood-Buff (KB) integrals. This so-called fluctuation solution theory, derived a long time ago by Kirkwood and Buff [82], relates fluctuations in the grand-canonical ensemble to integrals of radial distribution functions over the volume:

$$G_{\alpha\delta} = V\frac{\langle N_\alpha N_\delta\rangle - \langle N_\alpha\rangle\langle N_\delta\rangle}{\langle N_\alpha\rangle\langle N_\delta\rangle} - \frac{\delta_{\alpha\delta}}{c_\alpha}, \tag{2.5}$$

$$= 4\pi\int_0^\infty \left[g_{\alpha\delta}^{\mu VT}(r) - 1\right] r^2\,\mathrm{d}\,r, \tag{2.6}$$

$$\approx 4\pi\int_0^R \left[g_{\alpha\delta}^{NVT}(r) - 1\right] r^2\,\mathrm{d}\,r, \tag{2.7}$$

in which the value of the integration limit R should be sufficiently large. It is important to note that Eq. (2.6) and (2.7) is only valid in the thermodynamic limit [87]. In these equations, averages in the grand-canonical ensemble are denoted by the brackets $\langle\cdots\rangle$, $g(r)$ is the radial distribution function, V is the volume, N_α is the number of particles of component α, $\delta_{\alpha\delta}$ is the Kronecker delta and $c_\alpha = \langle N_\alpha\rangle/V$ is the concentration of component α. The approximation $g_{\alpha\delta}^{NVT}(r) \approx g_{\alpha\delta}^{\mu VT}(r)$ is often safe as all ensembles are equivalent in the thermodynamic limit. There are several ways to correct for finite-size effects, one is presented by Krüger *et al.* [87], and used by Schnell *et al.* [95] and Liu *et al.* [96]. In these works, the finite size effect is assumed to be linear with $1/N$, and can be eliminated by simulating two systems with same density, but different size. The radial distribution function in the thermodynamic limit is then:

$$g_{\alpha\beta}^{\infty}(r) \approx g_{\alpha\beta}^{N}(r) + \frac{c(r)}{N}, \tag{2.8}$$

where $g(r)^{\infty}_{\alpha\beta}$ is the radial distribution function in the thermodynamic limit, $g^{N}_{\alpha\beta}(r)$ is the radial distribution function for a finite-size system with N particles, and $c(r)$ is a function not depending on the system size. An alternative approach has been described by Ganguly and van der Vegt [97]. These authors propose a correction to the radial distribution function up to half the box-length:

$$g^{\infty}_{\alpha\beta}(r) = g_{\alpha\beta}(r)\frac{\left(1-\frac{(4/3)\pi r^3}{V}\right)}{\left(1-\frac{(4/3)\pi r^3}{V}\right)-\frac{1}{V}4\pi\int_0^r\left(g_{\alpha\beta}-1\right)(r')^2\,\mathrm{d}\,r'-\frac{\delta_{\alpha\beta}}{N_\beta}}, \tag{2.9}$$

which normalizes the radial distribution function with respect to the surrounding medium. The fact that in a closed system there is a finite number of particles (type α and β), this method may be used to correct for finite size effects.

Close to the critical point, concentration fluctuations will become very long-ranged and therefore integration of $g(r)-1$ over volume will not be possible in practise. The use of Eq. (2.7) is particularly useful at temperatures well below the critical point, where simulations in the grand-canonical ensemble suffer from poor acceptance ratios for particle insertions/removals [62]. Thermodynamic properties of mixtures directly follow from $G_{\alpha\delta}$, for example the partial derivative of the activity coefficient γ_1 of component 1 in a binary system equals [82]:

$$\left(\frac{\partial \ln \gamma_1}{\partial x_1}\right)_{p,T} = \frac{\Gamma_{11}-1}{x_1} = -\frac{c_2\left(G_{11}+G_{22}-2G_{12}\right)}{1+c_2x_1\left(G_{11}+G_{22}-2G_{12}\right)}, \tag{2.10}$$

where x_1 is the mole fraction of component one and Γ_{11} is an element of the matrix of thermodynamic factors [91]. The partial derivative of the activity coefficient is necessary for converting between Fick's and Maxwell-Stefan diffusivities [51, 96, 98].

Expressions for partial molar volumes, the isothermal compressibility and partial derivatives of activity coefficients in terms of KB integrals for binary and ternary systems can be found in Ref. [83].

It is important to note that the convergence of the integral in Eq. (2.7) using $g(r)$ obtained from molecular simulations is often poor. In practice, this integration requires extremely accurate estimates for $g(r)$ as well as very large box sizes. The reason for this is that $g(r)$ only converges to 1 for $r \to \infty$ for an infinitely large system. For a system of finite size, $g(r)$ converges to a value different from 1

when $r \to \infty$. Various approximations and interpolations may be needed for the KB integrals to converge, see for example the work of Wedberg *et al.* [84, 85] and Christensen *et al.* [99, 100]. The latter authors also pointed out that although the individual terms $G_{\alpha\delta}$ are difficult to obtain by direct integration, partial derivatives of the activity coefficients using Eq. (2.10) for binary mixtures do not depend too much on the upper integration limit R by a lucky cancellation of errors. Such a cancellation is not present for ternary systems [83]. Recently, Nichols *et al.* [101] have proposed an improved method for the determination of $G_{\alpha\delta}$ for systems with periodic boundary conditions. Their method is based on reducing systematic errors introduced by the boundary conditions, requiring a finite-Fourier-series expansion of concentration fluctuations. Clearly, there is a considerable interest in developing more efficient methods to extract KB integrals from simulations. The method presented in this Chapter has been used with success to determine multicomponent Fick diffusivities directly from equilibrium MD simulations [51, 97].

2.3 Systems Studied

2.3.1 Homogeneous Systems

Two different interaction potentials are considered in this study: WCA and Lennard-Jones (LJ) interactions. Eq. (2.1) and Eq. (2.2) provide the scaling with respect to $1/L$ for both Γ and h in small non-periodic systems. The large reservoir with periodic boundaries is equilibrated in the grand-canonical or canonical ensemble. Separate grand-canonical simulations with periodic boundary conditions were used to obtain the values for Γ and h in the thermodynamic limit (denoted by Γ_∞ and h_∞ respectively). All simulation boxes used were cubic with sides L_t. The embedded small system had the same geometric shape as the simulation box. For the LJ-fluid, we used a spherical cut-off at 2.5σ, where the potential was truncated and shifted. The WCA-potential is a shifted LJ potential with the attractive tail removed [102]. The LJ parameters σ and ε were taken as unit length and energy respectively.

We also considered mixtures consisting of different WCA particles. For simplicity, we are using a mixture of labelled particles. The pairwise interaction between particles of equal type is given by the regular WCA potential, while the interaction energies between particles of different type are scaled by a factor 1/10. We have used

a mixture of 70% particles of type 1 and 30% of type 2.

Simulations were performed using either grand-canonical Monte Carlo or MD in the NVT ensemble at a reduced temperature of $T^* = 1.8$. In the latter, the instantaneous temperature is constrained by the algorithm described in Ref. [77]. We investigated the effect on system size of the reservoir (L_t) and varied the size of the small subsystem up to $L_t/2$.

2.3.2 Heterogeneous System

Monte Carlo simulations in the NVT ensemble were used to study the thermodynamics of argon adsorbed in the zeolite silicalite-1 (MFI-type zeolite) at 100 K. The force field parameters for the LJ interactions between guest-guest and guest-host pairs were taken from the work of García-Pérez *et al.* [103]. All LJ interactions were truncated and shifted at 12 Å. The silicalite-1 unit cell has dimensions 20.022 Å in the x-direction, 19.899 Å in the y-direction, and 13.383 Å in the z-direction [15]. We consider a zeolite consisting of $4 \times 4 \times 8$ unit cells, leading to a simulation box with dimensions of 80.088 Å$\times$ 79.596 Å$\times$ 107.064 Å (128 unit cells in total). The small system sampling is identical to the sampling for the homogeneous systems, with one exception: the size of the embedded small system was restricted to steps of ¼ of the crystallographic unit cell in each direction. Eight different small systems were embedded, so the largest size of a small system inserted had ¾=2 unit cells in each direction, leading a total volume of $2^3 = 8$ unit cells which is 1/16TH of the supercell. We varied the loading of argon from zero to the maximum loading of 32 argon molecules per unit cell, corresponding to fugacities ranging from 0.001 Pa to approximately 500 kPa. The thermodynamic factor and heat of adsorption computed from separate grand-canonical simulations are compared with the results from simulations in the canonical ensemble using the described fluctuation method.

2.4 Results and Discussion

2.4.1 Homogeneous Systems

The inverse thermodynamic correction factor Γ^{-1} for the homogeneous systems is plotted in Fig. 2.2. The lines are straight lines fitted to the data points in the

linear regime. Nook- and corner effects are significant for the very small systems ($1/L > 0.5$), *i.e.* systems that are of the order of the size of a single particle. For very large embedded systems, we observe deviations from the linear behaviour. This can be explained by the fact that the reservoir no longer can act as a grand-canonical reservoir to the embedded small system when $L \approx L_t$. For the high density system (Fig. 2.2(a)), we have obtained the value for Γ_∞^{-1} from simulations in a grand-canonical ensemble, with sides $L_t = 10$ and periodic boundary conditions. This system is too small to embed small systems, but it is sufficiently large to determine Γ^{-1} for macroscopic systems from grand-canonical simulations.

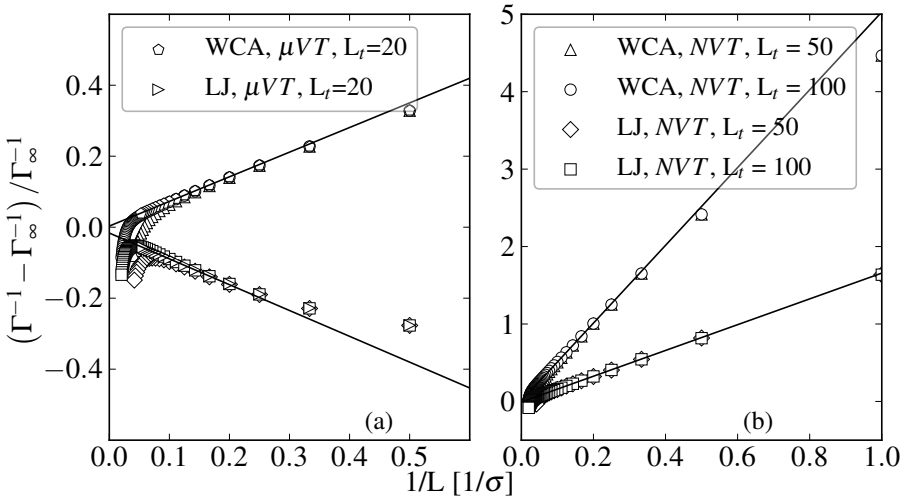

Figure 2.2: The inverse thermodynamic correction factor for the WCA and LJ fluids at reduced densities of (a) $\rho^* = 0.15$ and (b) $\rho^* = 0.60$. The temperature is $T^* = 1.8$ in reduced units. In (a) we also added the points obtained from sampling small systems in a reservoir equilibrated in the grand-canonical ensemble. The data obtained from the grand-canonical ensemble follow the straight lines well, while the data obtained from canonical reservoirs show deviations from linearity when $1/L \to 0$. This is a result of the reservoir being too small compared to L, as it no longer serves as a μT reservoir. We obtained the reference value Γ_∞^{-1} from the simulation in the grand-canonical ensemble using periodic boundary conditions. The legend has been split between the two parts of the figure to reduce overlap.

Equation (2.1) and Eq. (2.2) provide the general expressions for the scaling of thermodynamic properties with $1/L$. In our previous paper [71], these equations were verified numerically when the small system was embedded in a grand-canonical reservoir. The thermodynamic correction factor was calculated in the same manner for a system with WCA-particles in 2-dimensions. We have not included these results in this paper, as they do not lead to additional physical insight.

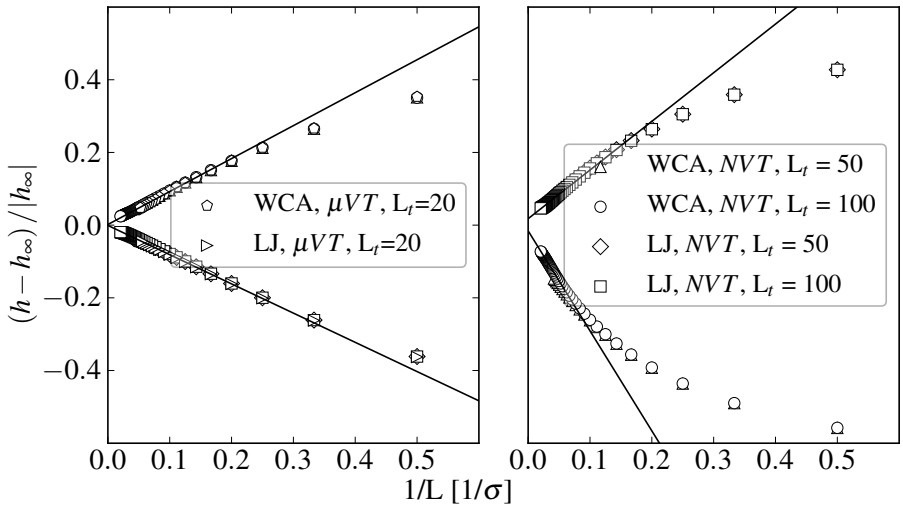

Figure 2.3: The molar enthalpy from a system with reduced density of (*a*) $\rho^* = 0.15$ and (*b*) $\rho^* = 0.60$. The temperature is $T^* = 1.8$ in reduced units. From the figures, we clearly see that the molar heat of adsorption is less sensitive to the size of the reservoir than the inverse thermodynamic correction factor. We obtain the value for h_∞ from simulations in the grand-canonical ensemble using periodic boundary conditions. The legend has been split between the two parts of the figure to reduce overlap.

In Fig. 2.3, we plotted the molar enthalpy for WCA- and LJ-particles at $\rho^* = 0.15$ and $\rho^* = 0.60$. The most striking difference between the scaling of the enthalpy and the thermodynamic correction factor is the behaviour of the enthalpy as the embedded system becomes large compared to the reservoir. In this case we do not see the same deviation from the linear behaviour when $1/L \to 0$. This indicates that computing the molar enthalpy does not require such a large reservoir as for the

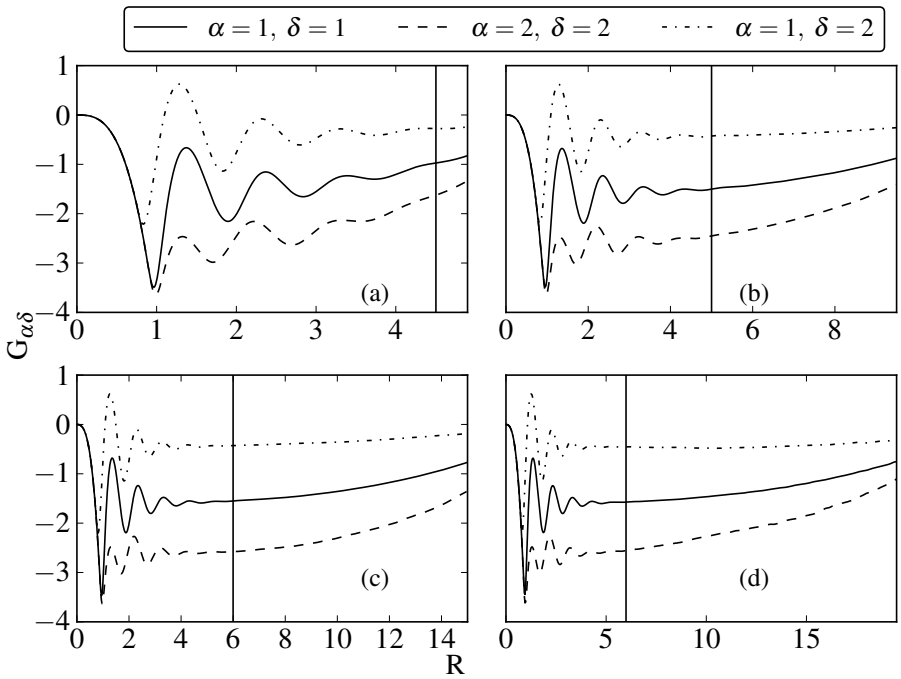

Figure 2.4: Kirkwood-Buff integrals for a 70/30 binary WCA system. The estimated values of $G_{\alpha\delta}$ are shown as functions of the integration boundaries (see Eq. (2.7)). (*a*) $L_t = 10$, (*b*) $L_t = 20$, (*c*) $L_t = 30$, and (*d*) $L_t = 40$. For (*a*) and (*b*) it is difficult to distinguish where the integral converges. For (*d*) we observe that the $[g(r)-1]r^2$ was not obtained sufficiently accurate for larger values of R. The vertical lines indicate where the values for $G_{\alpha\beta}$ listed in Tab. 2.1 were taken. All simulations were performed at a reduced density of $\rho^* = 0.75$ and a reduced temperature of $T^* = 1.8$.

thermodynamic correction factor. By extrapolating from the linear regime, we are able to determine the value of h_∞ for a macroscopic system with excellent accuracy, *i.e.* within 1 %.

In Fig. 2.4, we plotted the KB integral $G_{\alpha\delta}$ as a function of the upper bound R (see Eq. (2.7)) for a mixture of WCA particles. We investigated the effect of the system size. The vertical lines indicate the integration boundary R in each case,

see Tab. 2.1. The integration boundary is estimated from the plateau, which is, as expected, not always very clear as $g(r)$ for a finite-size system does not converge to 1 when $r \to \infty$ and therefore for large R the integral of Eq. (2.7) diverges. Especially for the two smallest systems ((*a*) and (*b*), with $L_t = 10$ and $L_t = 20$ respectively), the plateau is not easy to distinguish suggesting that this system is too small to obtain the KB integrals. The cut-off distances as well as the values of $G_{\alpha\delta}$ for various system sizes are listed in Tab. 2.1. For larger boxes (*c*), with $L_t = 30$ and (*d*), with $L_t = 40$, we find a sufficiently large plateau needed for making a reasonable estimation of the KB integrals.

Table 2.1: Values from Kirkwood-Buff integrals $G_{\alpha\delta}$ determined by integrating the radial distribution function (Eq. (2.7), Fig. 2.4), and from extrapolating the values found by embedding small systems (Eq. (2.5), Eq. (2.11), Fig. 2.5). The limit R for the integration of Eq. (2.7) is also given. Determining $G_{\alpha\delta}$ from the radial distribution function requires a box of at least sides $L_t = 30$ in this case. Embedding small systems and extrapolating leads to a very good estimation of $G_{\alpha\delta}$ already at $L_t = 10$, and the values are nearly identical for larger reservoirs.

$L_t/[\sigma]$	$\alpha\delta$	$R/[\sigma]$	Eq. (2.7)	Eq. (2.5), Eq. (2.11)
10	11	4.503	-0.977	-1.601
	22		-1.633	-2.686
	12		-0.275	-0.440
20	11	5.000	-1.508	-1.594
	22		-2.456	-2.601
	12		-0.429	-0.464
30	11	6.023	-1.552	-1.600
	22		-2.577	-2.602
	12		-0.428	-0.461
40	11	6.027	-1.574	-1.600
	22		-2.555	-2.621
	12		-0.455	-0.463

In Fig. 2.5, we plotted the values of the KB integrals when we sample the concentration fluctuations of the small systems embedded in the canonical ensemble simulation box (Eq. (2.5)). In this case we expect, analogous to Eq. (2.1) and (2.2)

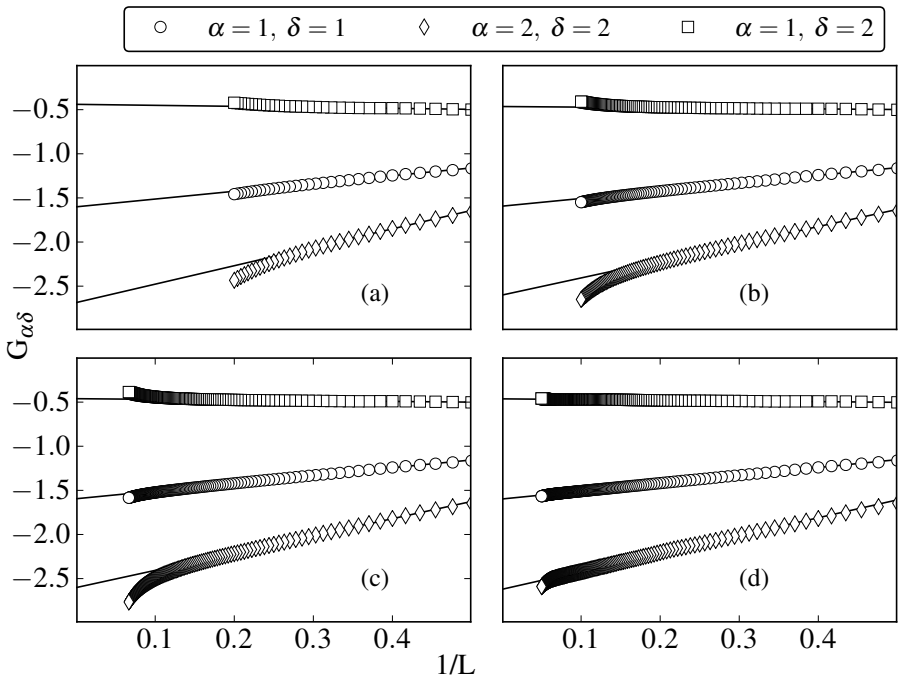

Figure 2.5: KB integrals for a 70/30 binary WCA system calculated using Eq. (2.5) and Eq. (2.11). Finite size scaling of $G_{\alpha\delta}$ as determined from sampling small systems embedded in a large reservoir of size L_t. (*a*) $L_t = 10$, (*b*) $L_t = 20$, (*c*) $L_t = 30$, and (*d*) $L_t = 40$. We fitted straight lines to the linear regime, and extrapolated till the thermodynamic limit ($1/L \to 0$). The final values of $G_{\alpha\delta}$ are shown in Tab. 2.1. The density of the system was in all cases $\rho^* = 0.75$ in reduced units, and $T^* = 1.8$.

that

$$G_{\alpha\delta} = G^{\infty}_{\alpha\delta} + A'/L, \tag{2.11}$$

in which A' is a constant that does not depend on L. The lines in Fig. 2.5 are fitted to the linear regime. These lines are extrapolated until the intersection with the vertical axis ($1/L \to 0$), and this value is taken to be the macroscopic value of $G_{\alpha\delta}$, *i.e.* $G^{\infty}_{\alpha\delta}$. This value can be compared directly to the value found by integrating the

radial distribution function, see Tab. 2.1. An excellent agreement is observed. In all cases, we are able to distinguish the linear regime quite easily, even for relatively small systems (see Fig. 2.5). A comparison between Fig. 2.4 and Fig. 2.5 clearly shows that obtaining KB integrals from density fluctuations in subvolumes is much more convenient than integration of the radial distribution function over volume. Thus, the new approach might make these computations more accessible for practical applications. The insensitivity to system size is further encouraging in this regard. The fluctuation solution theory based on the KB integrals has already demonstrated its great potential, *e.g.* as winner of the 3RD Industrial Fluid Properties Simulation Challenge in 2006 [99, 104].

2.4.2 Heterogeneous System

For the zeolite system, the embedded small system had sides dictated by the size of the crystallographic unit cell. The smallest system had sides $^1/_4 L_{\text{u.c.}}$. The increment in small system size were $^1/_4$ unit cell for each small system, and eight different small systems were used. Therefore, the largest small system embedded in the crystal is $2L_{\text{u.c.}}$, or $^1/_{16}$TH of the total simulation box.

In Fig. 2.6, we plotted the inverse thermodynamic correction factor as a function of the loading. The solid line shows the values obtained from simulations in the grand-canonical ensemble with periodic boundary conditions, serving as a reference for the thermodynamic limit. The symbols are values obtained from embedding small systems in a canonical simulation, while the dashed lines are from embedding a small system of the same size in a grand-canonical simulation box. The overall correspondence is very reasonable. It is immediately clear that the shape of the small system is very important for the result. All the small systems consisting of at least one unit cell in all directions correspond well with the result obtained from a system with periodic boundary conditions. For systems where this is not the case, the deviations are severe, and clearly deviate from the macroscopic result.

In Fig. 2.7, we plotted the local density of one unit cell of silicalite-1, projected in the xy, xz and yz-plane. The intensity shows the areas where it is most most likely to find a particle. The dashed lines indicate the ¼ step in each direction. It is obvious that small changes in the shape of the small system have a large effect on the average number of particles inside the small system, and therefore, the fluctuations

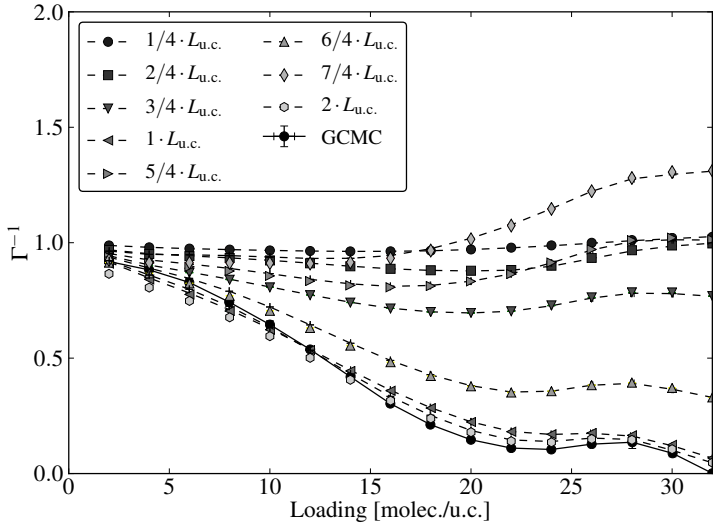

Figure 2.6: The thermodynamic correction factor of argon in silicalite-1, obtained by sampling with small systems in a large simulation box at 100 K. The solid line is thermodynamic correction factor obtained from simulations in the grand-canonical ensemble using periodic boundary conditions. The dashed lines are from embedding small systems in a simulation box in the grand-canonical ensemble, and the symbols are from embedding small systems in the canonical ensemble.

of energy and particles.

Fig. 2.8 shows the isosteric heat of adsorption for argon in silicalite-1. Again, the reference values are plotted as a solid line, while the dashed lines are from embedding different small systems in the grand-canonical simulation. The symbols are from embedding the small system in a canonical ensemble. For lower loadings, all the small systems lead to good estimations of the molar isosteric heat of adsorption. The best approximation is found from the system with $L = 2L_{\text{u.c.}}$ The molar isosteric heat of adsorption does not seem to have the same strong dependence on the shape of the control volume, as the thermodynamic correction factor. However, it is significantly better to have a subvolume with sides being at least one single unit cell.

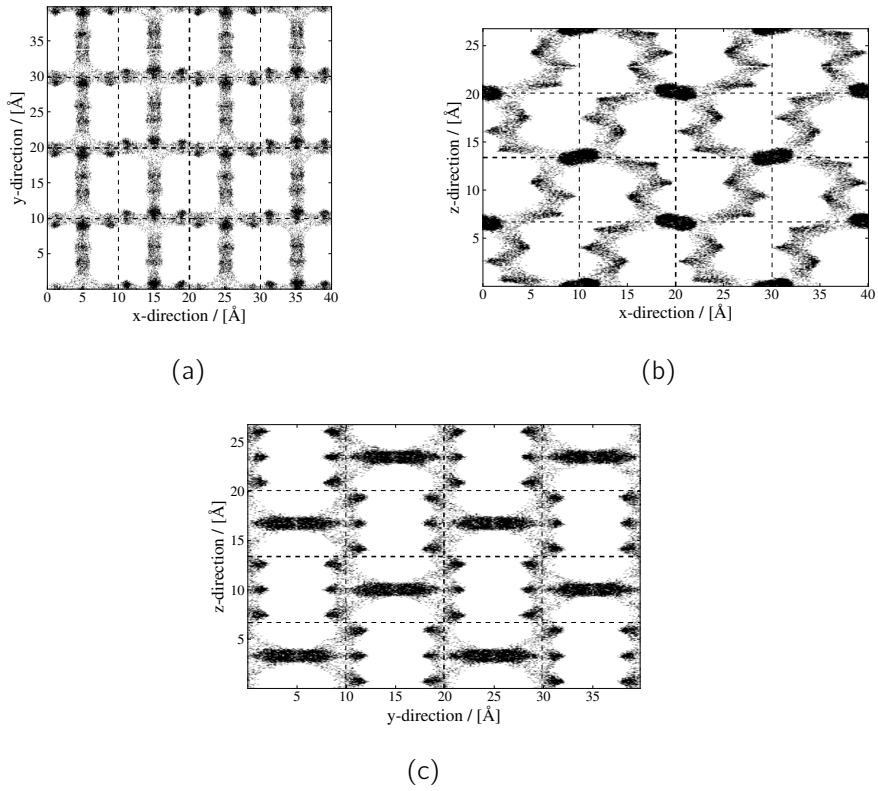

Figure 2.7: The positions of argon atoms inside silicalite-1 projected on the xy, xz, and yz planes. The density plots were constructed from the positions of argon in 535 snapshots, with 128 molecules per snapshot in a system with $2 \times 2 \times 2$ unit cells. One unit cell in all directions is plotted. The dashed lines indicates the $^1/_4$ unit cell in each direction. We clearly see how the system is well characterized in the x and y direction with steps of ¼unit cell, but the symmetry imposed by the zeolite structure requires larger steps.

The zeolite system does not show a pronounced finite-size scaling of $1/L$ as was found for the homogeneous systems. We feel that this is most likely related to the zeolite structure. With that in mind, sampling in the canonical ensemble gives very good agreement, as long as the structure of the zeolite is taken into account.

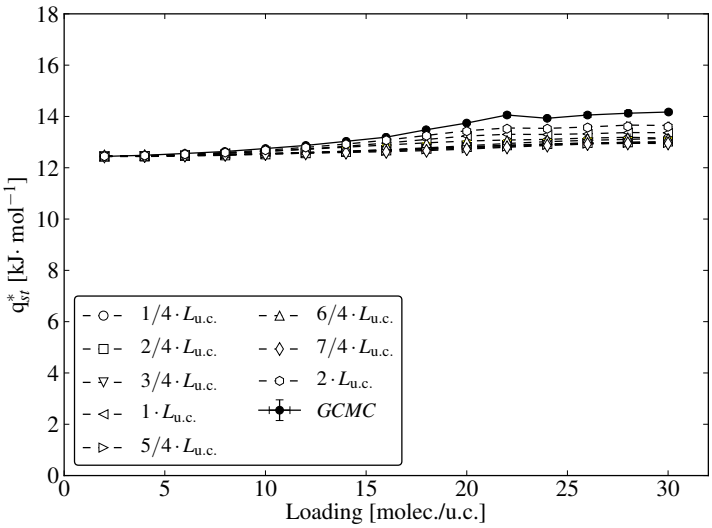

Figure 2.8: The isosteric heat of adsorption for argon in silicalite-1 at 100 K. The dashed lines are results from embedding small systems in a simulation box in the grand-canonical ensemble, and the symbols are from embedding small systems in the canonical ensemble. For this system, the shape of the control volume is not as important as for the thermodynamic correction factor. Also, we do not observe a clear finite size scaling. The heat of adsorption found from studying fluctuations lead to a very good representation of the molar isosteric heat of adsorption for this system.

2.5 Conclusions

We verified the method of sampling small systems embedded in a large reservoir. We conclude that the proposed method leads to very good results and can be considered as a valuable tool in obtaining thermodynamic data for systems where it is difficult to perform simulations directly in the grand-canonical ensemble, *e.g.* at low temperature. Obtaining the Kirkwood-Buff integrals has shown to be very efficient using this method, and one avoids the inherent problems associated with integrating the radial distribution function over volume. Moreover, the required system size is much smaller. This is especially useful for studying dense systems,

where simulations in the grand-canonical ensemble are too inefficient. The results for the zeolite system show that for heterogeneous systems the size of the control volume needs to be commensurate to the size of the unit cell of the zeolite. This is in agreement with the findings of Simon and Rubi [105] concerning local temperature fluctuations. Recently, the work of Ganguly and van der Vegt verifies the small systems approach on urea—water and methanol—water mixtures [97].

Very recently the small system sampling method presented in this chapter has been developed further, and the result of these investigations have been presented in several papers [51, 73, 75, 87, 95, 96]. These investigations have studied the nook- and corner contributions, and the shape of the control volume has been studied [73], Kirkwood-Buff coefficients for binary [75] and ternary mixtures [51] have been determined, an expression for finite-volume KB-integrals has been derived [87], and this has in addition been used to determine properties of single ions in solutions [95]. Much of this work has been gathered and is publised as a review [96]. This clearly shows that small system thermodynamics is an active field for research.

Chapter 3

External Surface Adsorption

This Chapter is based on the paper: E. García-Pérez, S. K. Schnell, J. M. Castillo, S. Calero, S. Kjelstrup, D. Dubbeldam, and T. J. H. Vlugt: 'External Surface Adsorption on Silicalite-1 Zeolite Studied by Molecular Simulation', J. Phys. Chem. C., 115, 2011.

Abstract

We have studied the adsorption of ethane, propane, and their mixtures on the external surface of silicalite-1 zeolite by molecular simulation using a classical force field. The Ideal Adsorbed Solution Theory (IAST) was successfully used to describe mixture adsorption, both on the external surface and inside the zeolite. Propane is preferentially adsorbed inside the zeolite for fugacities from 10^3 Pa to 10^8 Pa, while ethane is favored at higher fugacities. On the zeolite surface, propane is always preferentially adsorbed. We also determined the surface excess concentration for pure ethane and propane, as well as the surface excess of both components in an equimolar mixture. The surface excess concentration is negative or close to zero until the fugacity is approximately 10^5 Pa, when condensation of guest molecules on the external surface becomes important. The surface excess adsorption for ethane in a mixture is different than that for pure ethane, while for propane they are identical.

3.1 Introduction

The use of molecular simulations to describe the adsorption of guest molecules inside zeolites is nowadays an important tool in studying microporous systems [106–109]. Using relatively minor computational resources, detailed models for adsorption can be constructed, resulting in a better understanding of the transport, steric hindrance, location, and orientation of the adsorbed molecules. However, up until now, adsorption of molecules on the external surface of a zeolite has received far less attention. Studying surface adsorption can be quite a challenge experimentally, as the concentration of molecules on the surface can be very low and it is very difficult to distinguish surface adsorption from bulk adsorption in experiments. Therefore, computer simulation seems a natural choice for studying this. For a single zeolite crystal, the number of particles on the external surface will be small compared to those within the pores. Chandross *et al.* [110] used Molecular Dynamics (MD) and Monte Carlo (MC) simulations to study the dynamic exchange of molecules between a bulk zeolite phase, and an adjoining gas phase. The molecules used in this study were *n*-butane and *i*-butane. In their study of the surface, these authors focused on the surface residence time, and the importance of the surface as a barrier for transport into the zeolite. It was found that for thin membranes, the surface resistance can be significant. However, they only studied single component systems. Kortunov *et al.* [111] have performed interference microscopy studies of the surface of ZSM-5. The focus in this study was to investigate the importance of surface defects for transport of molecular species from a gas phase into the surface. These authors found that the surface structure is important for the kinetics of adsorption of *i*-butane in the zeolite crystal, and that surface defects can either increase or decrease the adsorption/desorption on the surface. There is now a considerable interest in using very thin zeolite membrane for separations [22]. This makes surface effects more important. It is also worth mentioning the work of Zimmermann *et al.* [33]. These authors define a critical crystal length as:

$$L^{\text{crit}} = \gamma \frac{j_{\text{intra}}}{j_{\text{surf}}/\lambda_{\text{surf}}}, \tag{3.1}$$

where j_{intra} and j_{surf} are the flux densities in the zeolite and at the surface, respectively, and λ_{surf} is the distance between the free energy well in the bulk gas phase

and the corresponding well in the zeolite phase. The value of γ provides a threshold for when the surface contribution is considered insignificant. The critical crystal length is defined as the width of a membrane, for which the surface resistance will negligible compared to resistance in the membrane itself. Using methane and ethane (and $\gamma = 200$, equivalent to 1 % of the total resistance), the critical crystal length was found to be typically 10^2 to 10^4 nm. Inzoli *et al.* [38] investigated the surface adsorption isotherm of *n*-butane on silicalite-1. In this work, the focus was exclusively on pure component adsorption. They also calculated the surface adsorption isotherms, along with the surface excess adsorption, which in certain cases was negative.

For studying transport into and through zeolites, making models of such transport, and modifying the zeolite to act as a better membrane, knowledge on what happens on and in the different parts of the zeolite is very important. The whole path, from molecules residing in the gas phase, adsorbing on the surface, entering the zeolite, and finally desorbing from the zeolite needs to be considered when constructing models for membrane transport. The surface acts as a barrier to transport [35] and a negative surface excess may be one of the contributors to this resistance. It is therefore necessary to have models accurately describing adsorption and composition of binary or multicomponent adsorption at the surface. In this work, we have used Monte Carlo simulations in the grand-canonical ensemble to obtain equilibrium adsorption data for surface adsorption. This should lead to a better molecular understanding of surface adsorption and barriers for mass transport at the surface. The simulations are performed with ethane, propane, and their equimolar mixture. The Ideal Adsorbed Solution Theory (IAST) of Myers and Prausnitz [112] is applied to the pure component adsorption isotherms, in order to predict the surface adsorption of a mixture of these two components. The Ideal Adsorbed Solution Theory is a fairly simple model, in which two (or more) pure component isotherms, can be used to predict the adsorbed mixture composition for any gas mixture composition. In addition, we find the surface excess concentration of ethane, propane, and their equimolar mixture on the surface.

The remainder of this chapter is organized as follows: In Section 3.2, we describe the simulation method, the force field, and provide details on the description of the surface. We explain how the simulations are performed, and how the absolute concentration and surface excess concentration are determined. In Section 3.3,

we present our results: adsorption isotherms, mixture isotherms, surface excess adsorption, and we show that the IAST describes the mixture adsorption on the surface. In the final section, we summarize our findings.

3.2 Methodology

The computed adsorption isotherms were obtained using grand-canonical Monte Carlo (GCMC) simulations, in which the chemical potential of each component, the temperature, and the volume are fixed [62]. The imposed chemical potential of a component is directly related to its fugacity [113]. The simulations were performed in cycles, and in each cycle a Monte Carlo move was chosen at random with a fixed probability: translation (20 %), regrowth (20 %), rotation (20 %), and insertion/deletion of molecules (40 %). In the case of mixtures, identity changes were also performed with the same probability as the insertion/deletion of molecules [114]. Monte Carlo simulations of surface adsorption are computationally much more expensive than simulations for a corresponding bulk phase with periodic boundary conditions. Due to very large memory requirements, it is not practical to use grid interpolation techniques for computing guest-host interactions. More details on the simulation methods can be found elsewhere [62, 64, 66].

The ethane and propane molecules were modelled using the united atom approach, in which the CH_n-beads (pseudoatoms) are considered as single, chargeless interaction sites. The interactions of the adsorbed molecules with the zeolite are dominated by the dispersive forces between the pseudoatoms and the oxygen atoms of the zeolite [106, 115, 116]. These dispersive interactions are modelled by truncated and shifted Lennard-Jones potentials [65, 66] with a cutoff distance of 12 Å. All Lennard-Jones parameters were taken from the work of Dubbeldam *et al.* [66]. Lorentz-Berthelot mixing rules were used to calculate Lennard-Jones interactions between unlike atoms.

The positions of the zeolite atoms of silicalite-1 zeolite were taken from van Koningsveld *et al.* [117]. In this characterization of silicalite-1, the unit cell is orthorhombic (space group Pnma) with cell parameters: a =20.022 Å, b =19.899 Å, and c =13.383 Å. Simulations were performed for three different systems with periodic boundary conditions in all directions: (*a*) a system comprising $2 \times 2 \times 2$ unit

cells of silicalite-1 with periodic boundary conditions, (*b*) an empty box (without zeolite) with dimensions L_x =40.044 Å, L_y = 179.091 Å, and L_z =40.149 Å (taken from the dimensions of a silicalite-1 structure: $L_x = 2a$, $L_y = 9b$, and $L_z = 3c$), (*c*) a box containing a zeolite membrane, with dimensions L_x =40.044 Å, L_y =417.879 Å, and L_z =40.149 Å (taken from the dimensions of a silicalite-1 unit cell: $L_x = 2a$, $L_y = 21b$, and $L_z = 3c$). This system contains 18 unit cells of silicalite-1 placed at the center of the simulation box, with the straight channels of the zeolite oriented in the y-direction. Therefore, in this simulation box there are two gas regions, a zeolite membrane, and two surfaces separating the zeolite and the gas regions. The two gas regions account for approximately 85 % of the total box volume. Different surface structures appear depending on where the crystal was cut. In our case, the crystal is cut between two sinusoidal channels, perpendicular to the straight channel. The external surfaces of the zeolite were then flat with the pores emerging at the surfaces. The positions of the zeolite atoms are kept fixed, as it has been demonstrated that the influence of framework flexibility in the adsorption of small molecules in zeolites is negligible [118].

In experiments, silicon atoms at the surface are terminated with silanol groups. In our simulations, we did not saturate the silicon atoms at the surface for two reasons: (*1*) our model for the adsorbed molecules does not consider atomic partial charges, so that there are no electrostatic interactions between the adsorbed molecules and the zeolite; (*2*) the dispersive interactions between the adsorbed molecules and the hydrogen atoms in the silanol group are negligible.

All the simulations were performed at a temperature of 308 K. We computed density profiles along the y-direction of the simulation box, see Fig. 3.1. The loading on the different parts of the surface is found from integrating the density profile over the different parts of the surface. That is:

$$q_{\mathrm{A,gas}} = \int_a^d c_{\mathrm{A}}(y)\mathrm{d}y, \tag{3.2}$$

and

$$q_{\mathrm{A,host}} = \int_d^b c_{\mathrm{A}}(y)\mathrm{d}y, \tag{3.3}$$

where c_{A} is the local concentration of component A. We denote the dividing surface d, and take this to be the crystallographic surface (see Fig. 3.1). Position a and

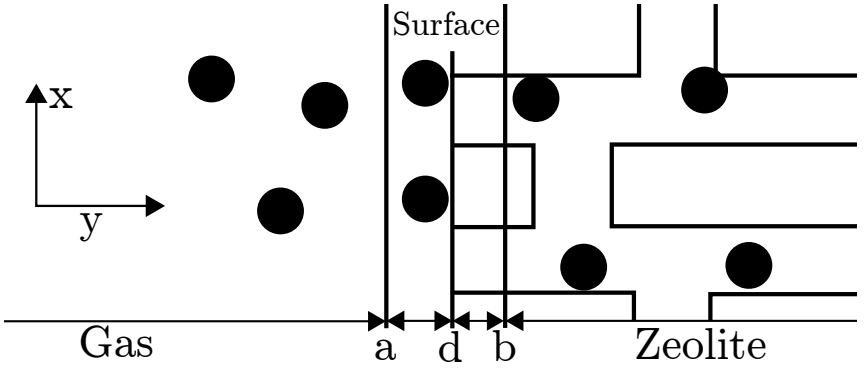

Figure 3.1: Schematic representation of the external zeolite surface, and positions of gas side and host side of the external surface. The crystallographic surface, d, is delimiting between the gas part and the host part. The surface is determined by studying the concentration profile in the y-direction. The typical extent of the surface is 10 Å for the gas side, and 7 Å into the host side, leading to a total surface of typically 17 Å. However, when condensation takes place, the gas side can easily extend up to 30 Å into the gas phase.

b are determined by comparing the local density profile with the corresponding bulk phase at the same simulation conditions. When the difference between these become larger than 1 %, we assume that we are in the surface region. In this way, the surface is separated into two parts: the gas part, going from the crystallographic surface and into the gas phase; and the host part, going from the crystallographic surface and into the zeolite structure. We can then study each of these parts individually, and by adding them, the external surface as a whole.

Considering the surface as a Gibbs-surface, we compute the surface excess concentration by integrating the local density [47, 119, 120]:

$$\Gamma_{\mathrm{A}}(y) = \int_a^b \left[c_{\mathrm{A}}(y) - c_{\mathrm{A}}^g \theta(d-y) - c_{\mathrm{A}}^z \theta(y-d) \right] \mathrm{d}y, \tag{3.4}$$

where Γ_{A} is the surface excess concentration of component A, y is the position along the y-axis in the box (perpendicular to the surface), and θ is the usual Heaviside step function. The superscript g and z refer to the concentration in the bulk gas phase and bulk zeolite phase respectively. The integration is performed from a to b, where position a is in the bulk gas phase, and b is in the bulk zeolite phase. In

this case, the position of a and b are of no importance, as we are considering excess properties. We take d to be the dividing surface, the crystallographic surface in this case.

3.3 Results and Discussion

Figure 3.2 shows the adsorption isotherms of ethane and propane as pure components and as an equimolar mixture in the bulk zeolite as a function of the fugacity of each component. The isotherms for the equimolar mixture obtained using the Ideal Adsorption Solution Theory (IAST) of Myers and Prausnitz [112] are shown with solid lines. Regarding the pure components, the adsorption for ethane is lower than for propane for fugacities lower than 10^5 Pa. At larger fugacities we observe the opposite behaviour, where the adsorption of ethane is notably larger than that

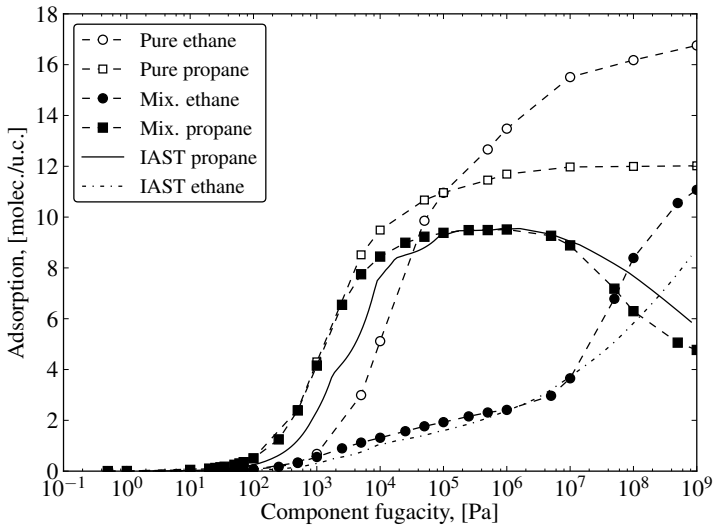

Figure 3.2: The adsorption isotherms of ethane and propane as pure components and in an equimolar mixture in silicalite-1 zeolite at 308 K. Error bars are smaller than the symbol size.

of propane. At low fugacity, the larger molecule adsorbs better due to the larger adsorption energy. At higher fugacity the loading of the smaller ethane molecule is larger because it is much easier to fill in the pores in the silicalite-1 as the loading increases. These effects are well known for bulk zeolites and have been observed previously by molecular simulations [121–123]. These effects also explain the behaviour of the mixture isotherm. At low fugacities we find the same behaviour as for the pure components, but there is a reversal of adsorption at 10^8 Pa. This reversal in the adsorption is due to the fact that, at saturation conditions, the ethane adsorbs more as a consequence of a size entropic effect [121]. The total mixture loading predicted using IAST compares very well with the GCMC simulations for the equimolar mixture of ethane and propane at these conditions.

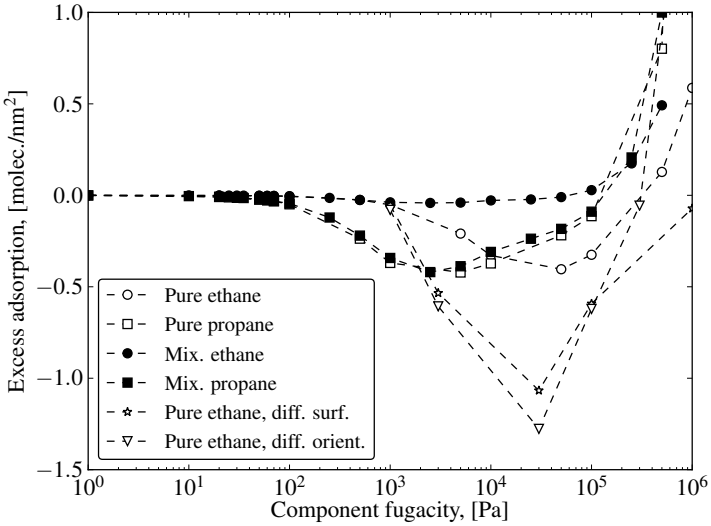

Figure 3.3: Ethane and propane surface excess adsorption for pure components and for an equimolar mixture in the system with a zeolite membrane. Also shown are results for a different cut of the surface, *i.e.* perpendicular to the y-axis of the zeolite and crossing the sinusoidal channels, as well as different surface perpendicular to the x-axis of the zeolite. Results are obtained using Eq. (3.4).

In Fig. 3.3 we compare the surface excess adsorption for pure components and for the equimolar mixture as a function of the component fugacity. The number of molecules adsorbed on the surface is expressed as number of molecules per unit of surface area. When the excess adsorption is positive, the adsorption of molecules on the surface is favoured. Pure ethane results in an excess adsorption nearly close to zero until we reach a fugacity of 10^3 Pa. The excess adsorption of pure propane is large and negative at low fugacities, and becomes positive between 10^5 and 10^6 Pa. There are considerable differences for ethane between the pure component and the equimolar mixture between 5×10^3 Pa and 5×10^5 Pa. Between this range of fugacities the excess adsorption of the mixture is zero, and negative for the pure component. On the other hand, the surface excess adsorption of propane does not show large differences between the pure component and the mixture. In conclusion, pure component ethane tends to adsorb more on the surface for the whole range of fugacities. However pure component propane provides the largest excess adsorption. Propane has the highest excess adsorption at high fugacities. In Fig. 3.3, we also provided the excess adsorption of ethane for a different cut of the surface, as well as for a different orientation. Clearly, the excess adsorption for these different surfaces is different.

Adsorption on the gas part of the external surface for ethane and propane as pure components, and their equimolar mixture are shown in Fig. 3.4. We observe that the adsorption of both ethane and propane is low until the fugacity approaches 10^3 Pa. This is related to condensation. The IAST analysis gives a very good representation of this case at low loadings. However, the IAST breaks down when condensation at the surface becomes important. Fig. 3.4(*c*) shows the left part of the plot on a logarithmic scale for both axis to better distinguish the details. The IAST perfectly predicts mixture adsorption on the surface. In Fig. 3.4(*d*) something similar is shown for the host part of the external surface. The agreement is excellent when we compare the mixtures isotherms from simulations to these from IAST analysis. In this system we have very similar conditions as we have inside the pores zeolite.

Finally, in Fig. 3.5 we study the adsorption on the external surface in total, this being the gas side and the host side considered together. When we compare the mixtures isotherms from simulations to these from the IAST analysis, the IAST analysis provides similar results as for the host side of the surface. For most of this system,

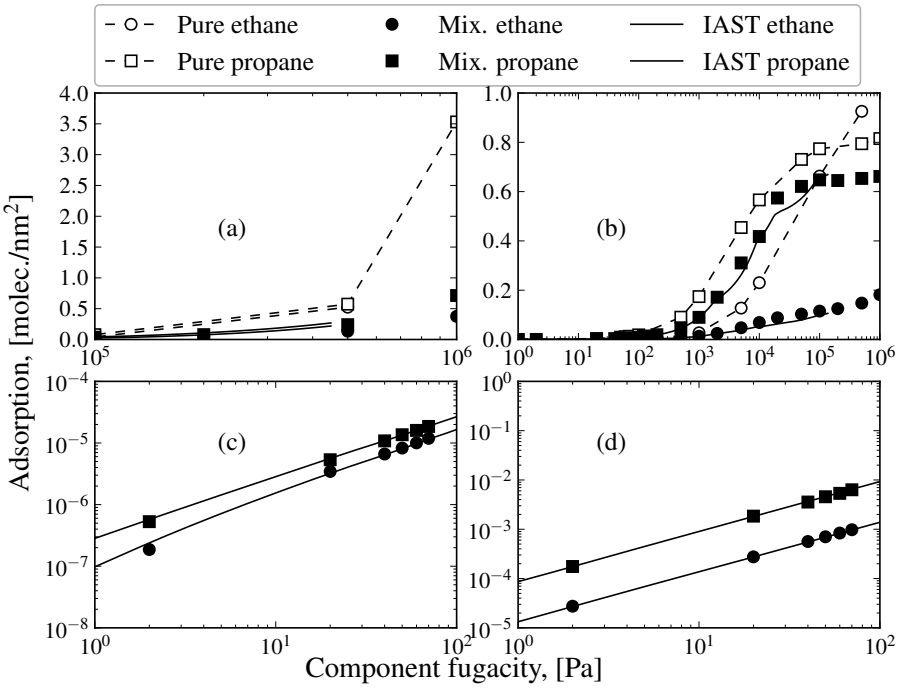

Figure 3.4: Adsorption on the gas-side of the external surface (*a*) and the host-side (*b*). Isotherms for the equimolar mixture compared to IAST analysis. Results from the IAST are shown as solid lines. The error bars from the simulation data are smaller than the symbol size. (*c*) and (*d*) shows the data from the low pressure part of Fig. (*a*) and (*b*) respectively. This is plotted in a log-log plot, to emphasize that IAST does describe the data very well at this low concentration regime. The steep increase in adsorption on the right side of the figure indicates that condensation occurs. The IAST give fairly good predictions up to 10^5 Pa.

the contribution from the gas-side of the surface is minor, until condensation occurs. Again, IAST predicts the adsorbed mixture composition within the expected range.

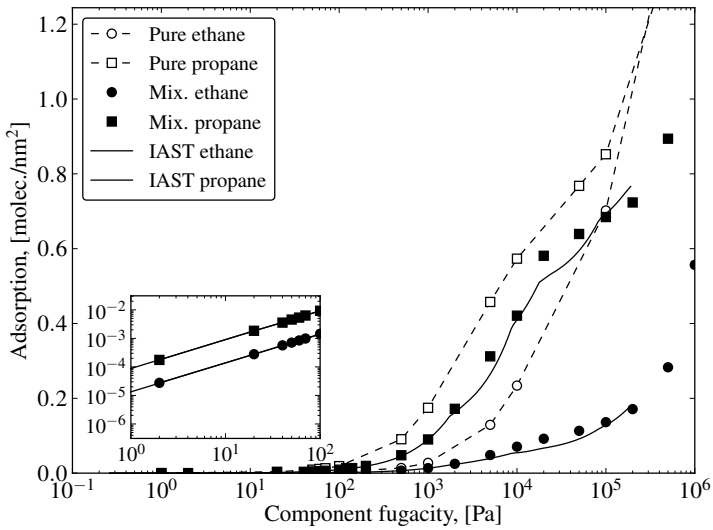

Figure 3.5: Total surface adsorption as a function of the component fugacity. This is a combination of the data plotted in Fig. 3.4 The adsorption on the host side is totally dominating up until condensation occurs on the gas side of the surface. The IAST predictions correspond well with data from simulations.

3.4 Conclusions

In this chapter, we investigated the single component and binary mixture adsorption of ethane and propane on the surface of silicalite-1 zeolite. The external surface is defined as a Gibbs surface, and changes in density lead to a gas-side and host-side surface. The crystallographic surface is taken as the dividing surface. The IAST is able to predict the mixture adsorption for the different parts of the external surface. We also find that the predictions for the zeolite framework correspond well with previous results. The IAST offers a simple and efficient way to get quantitative information on the mixture at zeolite surfaces. The fact that the IAST method works, indicates that we have ideal adsorption on the surface. In future work, we would like to look at competitive adsorption of branched and linear alkanes, as well as

adsorption of polar molecules on the surface of silicalite-1. With polar molecules, it is necessary to describe the structure of the surface with a different models, as electrostatic interactions will become significant. Our results clearly show that the excess adsorption of molecules on zeolite surfaces depends on the cut as well as the orientation of the zeolite crystal.

Chapter 4

Adsorption of Argon on MFI-Nanosheets

This Chapter is based on the paper: S. K. Schnell, L. Wu, A. J. J. Koekkoek, S. Kjelstrup, E. J. M. Hensen, and T. J. H. Vlugt: 'Adsorption of Argon on MFI-nanosheets: Experiments and Simulations', In preparation.

Abstract

Argon adsorption on zeolite nanosheets has been studied using molecular simulations and experiments. Zeolite nanosheets are thin sheets of zeolite, with a thickness on the nanometre length scale. Zeolite nanosheets have a large surface area compared to the mass of the zeolite crystal. No part of the zeolite nanosheet can be characterized as bulk zeolite. The pores, channels and cages of the zeolite are still present, so adsorption can take place inside the nanosheet, as well as on the external surface of the zeolite nanosheet. Capillary condensation can take place between parallel zeolite nanosheets, and this can occur at pressures below saturation pressure of the adsorbent. The large space on the external surfaces, as well as void space between surfaces of different nanosheets, can significantly increase the porosity of the system. This results in a different adsorption isotherm compared to the regular bulk zeolite structure, where adsorption on the external surfaces has only a mi-

nor contribution to the overall adsorption. In this paper, we develop a simulation model for studying adsorption of argon on the external surface of zeolite nanosheets and between layered zeolite nanosheets. Using molecular simulation, we study the effect of capillary condensation with different distances between the nanosheets. Results from molecular simulations are compared to adsorption isotherms from experiments. The comparison between bulk zeolite and zeolite nanosheets helps to distinguish adsorption on external surfaces from adsorption in the zeolite framework. We find that experimental data can be described using a simple nanosheet model in molecular simulations. In addition, the density profile around the external surface of the zeolite is studied. The density profile across the external surface is calculated, and used to determine the Gibbs surface excess concentration of the gas/zeolite interface.

4.1 Introduction

Zeolites are crystalline microporous aluminosilicates, extensively used in industry as solid acid catalyst [124–126]. Transport and adsorption properties of zeolites are important for improving their performance in catalysis and separation applications [127–130]. Transport of adsorbed molecules in zeolites can be severely hampered by the slow rate of diffusion in micropores and between cages [20, 131–134]. Transport in nanoporous materials has been studied by many authors [20–27]. The recent book by Kärger *et al.* [14] provides an excellent overview of theory, experimental methods, and simulation methods used to study transport of adsorbed molecules in microporous materials.

The observed selectivity of zeolites makes them very interesting for separation and catalysis applications [3, 135–137]. The high selectivity is caused by the structure of the zeolite, where channels with diameter on a molecular scale can completely exclude molecules from diffusing inside the zeolite framework [138]. This can strongly reduce the diffusivity of molecules that do in fact fit inside the zeolite. For many applications this can be a limiting factor. One approach to cope with slow diffusion is to synthesize zeolites with larger pores, introducing substantial mesoporosity (thereby reducing the total diffusion length inside the framework) [139–144]. Nanostructuring of zeolites into sheet-like crystals is explored as an alternative to

synthesizing mesoporous structures. The well known zeolite ZSM-5 (MFI-type) is the focus of the work by Choi *et al.* [21], Koekkoek *et al.* [11], and Na *et al.* [49, 145]. The surface area to mass ratio is maximized for thin zeolite sheets. At the same time, diffusion length for molecules inside the crystal is reduced [37].

Zeolite nanosheets typically have a thickness of about one unitcell [21]. The thickness of a zeolite/gas interface is usually 0.5 to 1 unitcells [35, 146]. Therefore, most of the zeolite nanosheet mass will be in contact with the solid/gas interfaces, the so-called external surface. No part can be considered as a bulk zeolite, *i.e.* a zeolite where the surface does not influence the local properties, like density, to any extent. Therefore, zeolite nanosheets must be described based on the surface properties, and not the bulk properties of the zeolite. The properties of the external surface are best described by excess variables [47]. Using the Gibbs definition of the surface [46], the surface properties, *e.g.* densities, can be described in a consistent way.

Application of thin zeolites are impeded by the problem of synthesizing a uniform layer, a thin sheet with oriented zeolite crystal [11, 21, 49, 145, 147]. The work of Choi *et al.* [21] has shown that it is possible to construct zeolite nanosheets of MFI-type zeolite with a thickness of only one unitcell. The nanosheet is oriented such that the straight channels are oriented perpendicular to the nanosheet surface. For adsorption or molecular sieving purposes this orientation of silicalite-1 is an advantage as diffusion of adsorbed molecules in the straight channels is much faster than in the sinusoidal channels [92, 134, 148, 149]. As shown by Choi *et al.* [21], Na *et al.* [49], and Koekkoek *et al.* [11], zeolite nanosheets may strongly improve catalytic properties of zeolites. This is caused both by the availability of catalytic sites, either being exposed on the external surface, or more easily accessible catalytic sites through shorter diffusion in channels. This may also reduce the problem of coking on the external surfaces and in channels [11]. In zeolite crystals, coking of the surface can both block catalytic sites on the surface, and restrict access to the interior of the zeolite. Zeolite nanosheets will to a lesser extent be affected by this [11].

A description of equilibrium and transport properties for the external zeolite surface was presented by Inzoli *et al.* [35, 38]. Equilibrium properties, *e.g.* adsorption isotherms, surface excess adsorption isotherms, and surface tension were determined for *n*-butane at the external surface of silicalite-1 (MFI-type) zeolite. In addition, using non-equilibrium molecular dynamics simulations, the resistance to

heat and mass transfer and the coupling coefficients for heat and mass transfer at the external surface were computed. These transport coefficients showed that the coupling of heat and mass transport at the external zeolite surface can be significant. Schnell *et al.* [150] used these coefficients to model transport of *n*-butane in a zeolite membrane. It was found that increasing the sweep-gas temperature increases the flux of molecules through a zeolite membrane, and the explicit modelling of the surface lead to temperature jumps at the surface. Accurate models and increased understanding of transport properties, selectivity, and surface heat-effects will help increasing the understanding of fundamental transport properties, and help optimize zeolite based systems for separation purposes.

Another equilibrium study of the external zeolite surface is the work of García-Pérez *et al.* [146] (see also Chapter 3 of this thesis), focusing on binary surface adsorption, and the applicability of Ideal Adsorbed Solution Theory (IAST) [112] for adsorption on silicalite-1 surfaces. These authors calculated adsorption isotherms of ethane and propane at the external zeolite surface, and determined the surface excess adsorption. The work of Inzoli *et al.* [35, 38] and García-Pérez *et al.* [146] use a definition of the external surface proposed by Gibbs [46], in which the surface is a plane where the *equilibrium* intensive properties (*e.g.* density) are different from the neighbouring bulk-phases [46, 47]. The Gibbs surface definition is an efficient way to define the external surface in a consistent thermodynamic analysis [47]. This is especially useful in molecular simulations, where the local density can be computed also across the external surface. Zimmermann *et al.* [33, 34, 36] studied transport across external zeolite surfaces, and described the resistance to mass transport across this gas/zeolite interface. These authors did not use the Gibbs surface definition, but used instead the critical crystal length [151] to define the extent of the external surface. The critical crystal length is the distance between the free-energy minima on the gas-side of the crystallographic surface, and the local free-energy minima on the zeolite side of the crystallographic surface. This way of defining the surface is much more system specific, as the minima changes from system to system. The Gibbs definition of the surface is gauge invariant for transport properties at the external surface, an preferable in non-equilibrium systems [48]. Zimmermann *et al.* [152] also investigated the transport across thin nanosheets of AFI-type and LTA-type zeolite, using non-equilibrium molecular dynamics to simulate transport across the zeolite nanosheet. This study provided direct access to

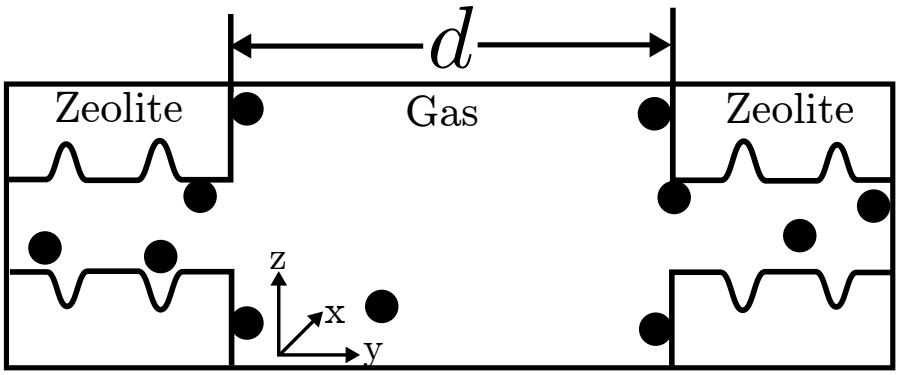

Figure 4.1: Schematic illustration of the systems studied in our simulations. The distance d is the surface to surface distance, and denotes the size of the gas-phase. The argon molecules are show as black circles. In the nanosheet simulations, the size of the gas-phase is large, d =40 Å, so argon could be in the gas-phase without having any interaction with the zeolite, or molecules adsorbed on the surface of the zeolite. The system has periodic boundary conditions in all directions, so the zeolite slab will appear to be an infinitely large sheet of zeolite. In the layered structure, the size of the gas-phase is d =5 Å, and incremented up to 40 Å. We find that this is a sufficiently large system to represent the nanosheet-structure. Argon in the gas-phase can interact with one or both surfaces of the zeolite. This can lead to capillary condensation at pressures below saturation pressure.

transport properties of zeolite nanosheets, but does not require an explicit definition of the external surface.

In this work we have studied adsorption of argon on silicalite-1 (MFI-type) nanosheets with the aim to increase our understanding of the adsorption process. For an initial study, and for convenient comparison with experimental data, argon in chosen as adsorbent. Experiments and molecular simulations with classical force fields have been used to obtain adsorption isotherms. From molecular simulations, the density profile of argon around the external zeolite surface was determined. The density profile has been used to calculate the surface excess adsorption on the external surface. In experiments, capillary condensation occurs at low pressure, and can be difficult to distinguish from adsorption in pores. We study how the effect of layered zeolite nanosheets influence the capillary condensation between

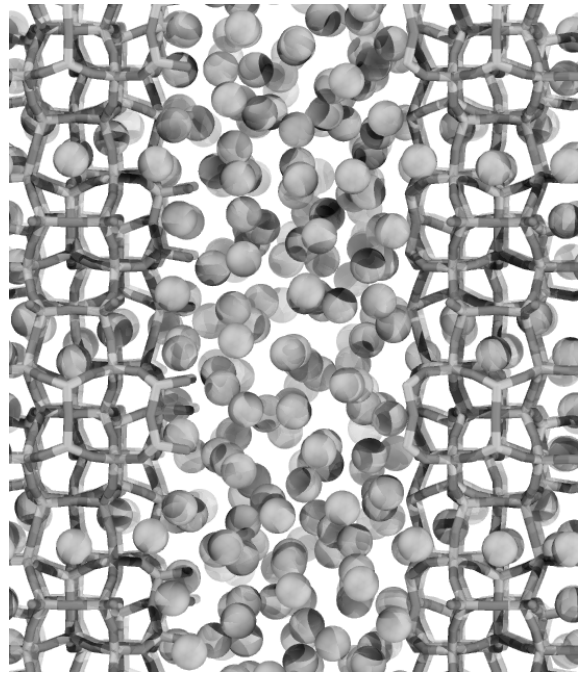

Figure 4.2: Typical simulation snapshot of argon adsorption between zeolite nanosheets at 30 kPa and 87 K. The zeolite framework is shown as rods (dark grey is oxygen, and light grey is silicon). Argon is shown as spheres. The surface-to-surface distance is d =5 Å. This snapshot is comparable to the schematic representation shown in Fig. 4.1.

the layers, and how this can be observed in the adsorption isotherms. This layered structure is schematically illustrated in Fig. 4.1 (see also Fig. 4.2). In the caption it is described how the inter-sheet distance is calculated. The adsorption between zeolite nanosheets with different inter-sheet distances has been studied using molecular simulations. Condensation at the external surface is studied at pressures below saturation pressure. Capillary condensation between surfaces with different inter-sheet distances have been studied at pressures below the saturation pressure for argon. The surface excess adsorption of argon on silicalite-1 nanosheets can be calculated for various layered structures of zeolite nanosheets. Surface excess adsorption isotherms for the zeolite nanosheet are found to be in good agreement with previously published results for the external zeolite surface.

This chapter is organized as follows: in Section 4.2, we describe the difference between excess adsorption and surface excess adsorption, focusing on the Gibbs definition of the external surface. The molecular simulations are described in Sec-

tion 4.3, while in Section 4.4 the results from both experiments and simulations are presented and discussed. In Section 4.5, our findings are summarized.

4.2 Excess Adsorption and Surface Excess Adsorption

We distinguish between surface excess adsorption and excess adsorption. These are different thermodynamic quantities, even though the names are confusingly similar. *Excess adsorption* refers to the amount of adsorbed molecules in a sample, where the volume of the sample is subtracted from the volume of the container used to hold the sample [153]. The absolute adsorption can be directly determined from molecular simulations. The absolute adsorption is the total amount of gas adsorbed in the system, *i.e.* the average number of particles in one simulation. Excess and absolute adsorption have the same units. In this work, to quantify adsorption we use volume adsorbate at standard temperature and pressure per gram adsorbent, cm^3 STP /g zeolite. The excess adsorption n^{excess} can be related to the absolute adsorption as [154]:

$$n^{\text{excess}} = n^{\text{absolute}} - V^{\text{g}}\rho^{\text{g}}, \tag{4.1}$$

where V^g is the pore volume of the zeolite, calculated from simulations using helium as guest-molecules at 298 K [154], and ρ^g is the density of argon as gas at the given temperature and pressure. To compare adsorption isotherms from experiments with adsorption isotherms from simulations it is necessary to convert absolute adsorption isotherms into excess adsorption isotherms. For pressures above the saturation pressure of the adsorbate, the excess adsorption isotherm has a significantly smaller loading than the corresponding loading from the absolute adsorption isotherm. This is caused by the $V^g\rho^g$ term, as this can become large if the pore volume is large. The excess adsorption isotherm can even become negative if the pressure is above saturation pressure [154]. In this work argon is used as guest-molecule at a temperature of 87 K. Since excess adsorption will become negative above the saturation pressure, we restrict ourself to pressures below 68 kPa [155].

The *surface excess adsorption* is calculated from the density profile of the adsorbate across the external surface. The density profile is calculated in molecular

simulations as the density in a volume element along an axis parallel to the external surface. Using the Gibbs definition of a surface [46, 47], the surface excess adsorption can be determined by

$$\Gamma = \int_a^b \left[c(x) - c^g(a)\theta(d-x) - c^z(b)\theta(x-d) \right] \mathrm{d}x, \tag{4.2}$$

where Γ is the surface excess adsorption (in units of *mol per area*), θ is the Heaviside step function ($\theta(x) = 0$ for $x < 0$, and $\theta(x) = 1$ for $x > 0$), and $c(x)$ is the concentration profile (in units of *adsorbent per volume*), and x is the position perpendicular to the gas-zeolite interface. The dividing surface is denoted by d. The limits for the integration, a and b, are positions in the bulk phases. The exact positions are not important, as long as they are in the bulk phases. The dividing surface is denoted d, and can be chosen arbitrarily [46–48]. $c^g(a)$ and $c^z(b)$ are the bulk-phase concentrations, *i.e.* the concentration in the bulk-phases next to the surface (in position a and b).

4.3 Simulations

Grand-canonical Monte Carlo (GCMC) simulations were performed using classical forcefields. Interactions are described with Lennard-Jones (LJ) potentials between guest-host, and guest-guest molecules. The force field parameters were taken from the work of García-Pérez *et al.* [103]. Interactions between argon and the zeolite framework are determined from argon and oxygen atoms in the framework [66]. The LJ pair potential was truncated and shifted at a distance of 12 Å. The zeolite framework was modelled as a rigid structure, as framework flexibility is not important for equilibrium adsorption of small molecules [118]. Following García-Pérez [103], electrostatic interactions were not included. In this work, the pressure in the gas phase ranged between 0.01 Pa to almost 70 kPa, and the temperature was kept at 87 K. For more details on GCMC simulation, we refer the reader to Refs. [62, 66, 106].

Coordinates of oxygen and silicon in the zeolite framework were taken from crystallographic data by van Koningsveld *et al.* [117]. Bulk and nanosheet zeolite systems were simulated. The systems were defined as follows:

1. Bulk zeolite: A zeolite crystal (2 × 2 × 2 unitcells, or 39.798 Å, 40.044 Å, and 26.766 Å respectively) that spans the system in all three directions. The system is therefore continuous, and there are no surface or gas-phase present. This system will be used as a reference for the zeolite bulk-phase adsorption, and for calculating surface excess adsorption isotherms. It is necessary to compare the adsorption on zeolite nanosheets with the adsorption in the pure zeolite phase.

2. Zeolite nanosheet: The zeolite is placed in the centre of a simulation box (2 × 1 × 3 unitcells). The crystal spans the simulation box in the crystallographic a and c directions (corresponding to the Cartesian x and z direction in the simulation box; the dimensions of the zeolite unitcell in these directions are 19.899 Å, 20.022 Å, and 13.383 Å respectively [117]). The gas-phase is parallel to the zeolite b-direction (simulation box y direction), and is created by increasing the size of the simulation box (in the y direction), while keeping the centre of mass for the zeolite crystal at the centre of the simulation box. Periodic boundary conditions are used in all directions. Therefore, the inter-sheet distance d is the length of the simulation box, minus the thickness of the zeolite slab in the y-direction. This zeolite slab model is shown schematically in Fig. 4.1. The distance d between the surfaces is varied to study the effect of layering, and how capillary condensation between zeolite nanosheets contributes to excess adsorption isotherms. To have a bulk-type gas phase, a molecule in the gas-phase should have no interactions with the surface or molecules on the surface. In this work, the surface-to-surface distance of 40 Å is found to be large enough to accomplish this. This will be denoted by 'nanosheet', as it can be viewed as a single sheet of MFI-type zeolite, one unitcell thick. As interactions ranging longer than 12 Å will be cut-off, there will be a significant gas-phase where the molecules cannot interact with either surface, or molecules adsorbed on the surface.

Since the periodic structure of the zeolite framework is discontinued at the gas/zeolite interface, it is important to consider exactly where the external surface is introduced in the framework. Inzoli *et al.* [35, 38] consider this in their work, and describe two ways of introducing a surface in the xy plane of silicalite-1 zeolite:

1. A cut between two sinusoidal channels in the zeolite. This introduces a 'flat' structure on the surface, and the straight channels protrude on this surface.

2. A cut in the sinusoidal channels in the zeolite, creating a 'rough' structure on the surface. The straight channels protrude into the remainder of the sinusoidal channels.

Inzoli *et al.* [35, 38] observed minor differences in the adsorption isotherms of *n*-butane on the external surface between these surface structures. The second alternative, a 'rough' structure has been used for the simulations in this work.

In reality, zeolite surfaces are terminated with silanol groups that have a dipole moment. In our simulations, these groups are not included. The work of Inzoli *et al.* [35, 38], Zimmermann *et al.* [33, 34, 36], and García-Pérez *et al.* [146] also exclude these external surface groups. Argon does not have electrostatic interactions in the model, this will probably have a minor influence on the adsorption isotherms for non-polar particles, like argon.

4.4 Results and Discussion

4.4.1 Adsorption Isotherms

Adsorption isotherms for argon in a bulk zeolite, experimental results for a zeolite nanosheet [156], and simulation results from a nanosheet are shown in Fig. 4.3. For pressures below 10 kPa, the nanosheet model results in an isotherm with systematically lower adsorption than the experimental isotherm. Some of the differences can be attributed to capillary condensation between nanosheets in the experiments. In the experimental setup, overlap between sheets, and nooks between sheets perpendicular to each other may create favourable adsorption sites. In the simulations, there are no overlap between sheets, defects, impurities in the zeolite framework, or defects at the surface of the nanosheets that may increase adsorption at low pressures. The adsorption isotherm for a bulk zeolite shows that more argon is adsorbed than in experiments for pressures above 10 Pa and below 2 kPa. At higher pressures, the bulk zeolite is saturated with gas. In this range (between 10 Pa and 2 kPa), argon prefers the inside of the zeolite, and there is sufficiently space inside the zeolite to allow the gas to adsorb. With a zeolite nanosheet of one unitcell thick, no part of

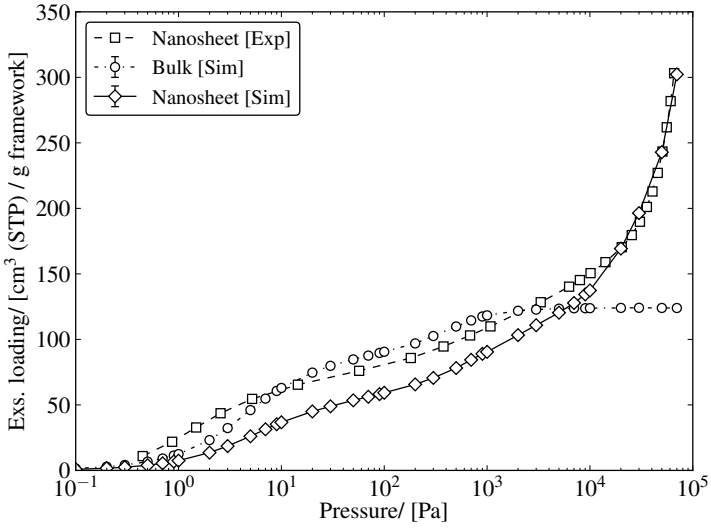

Figure 4.3: Excess adsorption isotherm of argon inside and on the external surface of silicalite-1 nanosheets, and for a bulk zeolite. In the legend, we distinguish between simulation results (Sim), and experiments (Exp). The bulk zeolite has no surfaces, so this system has a clear maximum for adsorption that is reached around 1 kPa. At this point, the zeolite is fully loaded with argon, and increasing the pressure will not increase the amount of argon adsorbed in the zeolite.

the zeolite can be characterized as a bulk zeolite, but argon will still prefer to adsorb inside the zeolite, as much as possible.

The adsorption isotherm for the bulk zeolite reaches a maximum loading around a pressure of 1 kPa, corresponding to a loading of 124 cm^3 STP/g zeolite. This corresponds well with the simulation results of García-Pérez *et al.* [103] (at 77 K), and experimental results of Saito and Foley[157] (at 87 K). For the experimental adsorption isotherm for zeolite nanosheets, as well as the simulation for a nanosheet, however, we observe that the loading (in units of cm^3 STP/g zeolite) can increase significantly compared to the bulk adsorption. For pressures above 10 kPa and higher, adsorption in surface layers at the external surface takes place and increases the adsorption in the system. The increase observed in the experimental adsorption

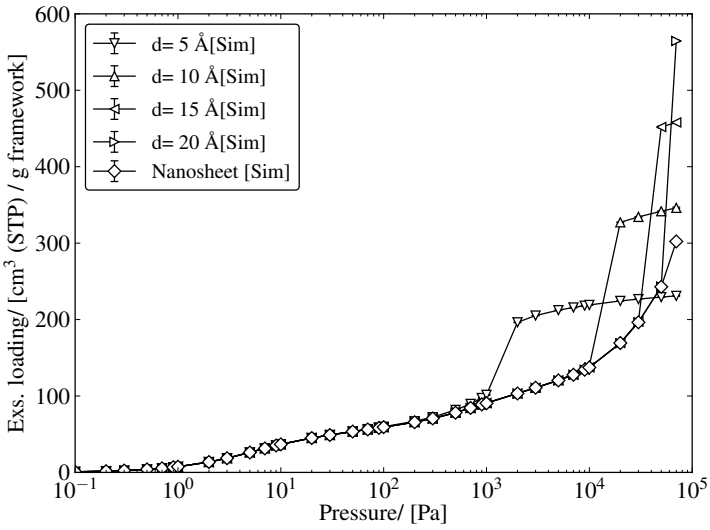

Figure 4.4: Computed excess adsorption isotherms of argon determined for various layered structures of zeolite nanosheets, see also Fig. 4.1 for the definition of the inter-sheet distance d. Significant steps in the adsorption isotherms can be observed, which can be directly related to the capillary condensation between the layers of zeolite. For smaller distances d, the surface-to-surface distance have a length scale comparable to typical mesopores. This results in a significant increased adsorption, as the gas will condense easily between the surfaces at pressures below saturation pressure.

can be attributed to capillary condensation between zeolite nanosheets, and condensation on the external surface. The adsorption isotherm for the zeolite nanosheet from simulation is, however, not affected by capillary condensation. At higher pressure, argon condenses at the external surface of the nanosheet. For pressures above 10 kPa, experimental and simulation adsorption isotherms are almost identical. In the experiments, silanol groups can contribute to the surface adsorption. This would probably be observed at lower pressures, before condensation becomes important at the external surface, but also during condensation the presence of silanol groups could be important. To investigate their role in adsorption would require further investigations beyond the present study, however.

In Fig. 4.4, the adsorption isotherms for argon in different layered arrangements are shown. As described in Section 4.3, the inter-sheet distance is denoted by d, and the legend in Fig. 4.4 indicates what this inter-sheet distance is. The nanosheet has inter-sheet distance d =40 Å, and no capillary condensation occurs for pressures below saturation pressure. For all these cases, the adsorption is seemingly not affected by increasing the pressure until 1 kPa. Up to this pressure, adsorption takes place inside the channels in the zeolite. In this work, the zeolite in the nanosheets are always the same, and adsorption should not be affected until capillary condensation becomes important. At pressure of 1 kPa, the layered structure with inter-sheet distance d =5 Å, being the shortest inter-sheet distance, shows a rapid increase in the loading as argon condenses between the surfaces. At around 10 kPa, the same is observed for d =10 Å, and similar steps are observed for the different layered structures at increasing pressures. For the system with d =5 Å, the loading reaches a plateau value, as the space between the surfaces are completely filled. Increasing the pressure further only shows a small increase in the adsorption, as the liquid phase is almost incompressible. The isotherms in Fig. 4.4 confirm that the experimental results can be described by the nanosheet model used in the simulations. For an inter-sheet distance of d =20 Å the rapid increase associated with capillary condensation is very close to the saturation pressure of argon at 87 K, increasing this distance to 40 Å should safely shift the capillary condensation pressure for this spacing very close to the saturation pressure.

4.4.2 Argon Density Profiles

In Fig. 4.5, we have plotted the density profile of argon around the external surface for two layered structures and for the nanosheet. Two pressures are shown, 1 kPa and 30 kPa. The crystallographic surface is shown as a vertical, dashed line. The gas-phase is to the left of the crystallographic surface, while the zeolite-phase is to the right. From the density profile in Fig. 4.5 it can be observed that at low pressures the difference between the three systems is minor. Argon molecules prefer to reside inside the zeolite. At higher pressures there is a clear difference among the adsorption profiles of the surfaces. The nanosheet has a quite small adsorption on the surface, and the density profile indicates that the concentration on the outer part of the surface is close to the gas-phase concentration. The density profile indicates

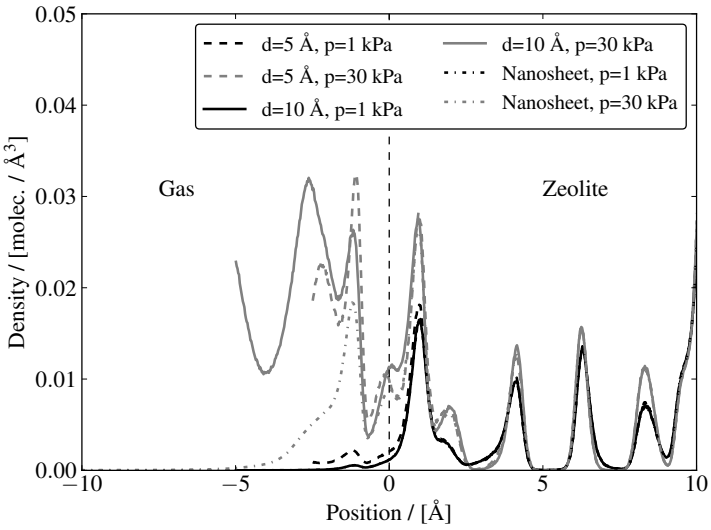

Figure 4.5: Density profiles as a function of the position across the zeolite surface for sheet distance d =5 Å, d =10 Å, and for the zeolite nanosheet. The vertical dashed line shows the position of the crystallographic surface. The zeolite structure is to the right of the dashed line, while the gas-phase is to the left. The figure shows the adsorption around the surface for two layered structures, as well as for the nanosheet structure at pressures 1 kPa and 30 kPa. The layered structures (d = 5 and d = 10) show how the capillary condensation takes place at pressures above 1 kPa. For the nanosheet, there is condensation on the surface, but even at pressures of 30 kPa, we can only observe a mono-layer adsorption on the external surface, at a sheet distance of 10 Å, the gas-phase is seemingly unaffected by the surface.

that there is one adsorbed layer on the external surface. The layered structures have both clear capillary condensation in the gas phase for a pressure of 30 kPa, well below the saturation pressure of 68 kPa for gaseous argon [155].

4.4.3 Surface Excess Adsorption

In Fig. 4.6, the surface excess adsorption isotherms for the nanosheet as well as the layered structures are shown. As expected, the surface excess adsorption isotherms show a loading of zero or even negative loading for pressures well below the satu-

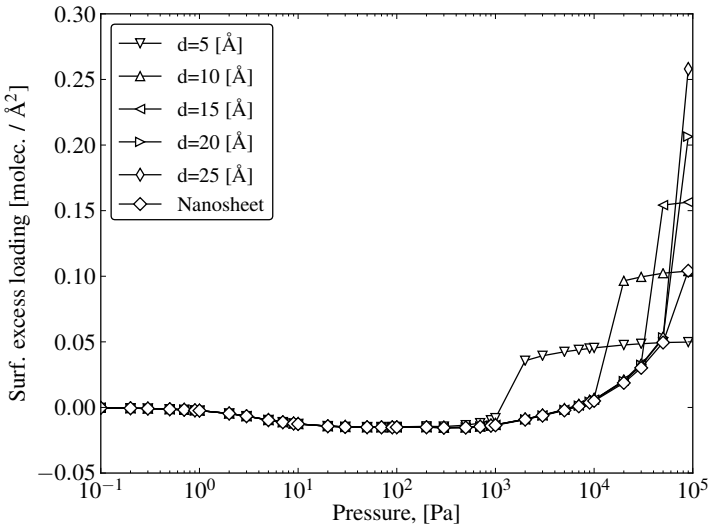

Figure 4.6: Surface excess adsorption of argon, determined for different layered nanosheet structures, calculated using Eq. (4.2). For lower pressures, the surface excess adsorption is zero or negative. At higher pressures, the surface excess adsorption isotherm becomes positive, and shows the same step behaviour that we observe in the adsorption isotherm. At this pressure, the mesopore created between two zeolite surfaces allows argon to condense at pressures below the condensation pressure.

ration pressure. This low surface excess means that the surface has a smaller concentration of particles than the corresponding bulk phases, especially the zeolite phase, see also Fig. 4.5. For higher pressures, we see how capillary condensation between the surfaces strongly increases the surface excess adsorption. The surface has more space for adsorbing particles than the zeolite framework, particles can be packed tighter not being restricted by the zeolite structure. These surface excess adsorption isotherms are similar to the surface excess adsorption isotherms found by Inzoli *et al.* [38] for *n*-butane at the external surface of silicalite-1 and by García-Pérez *et al.* [146] for ethane and propane at the external surface of silicalite-1. For the nanosheet, the surface excess adsorption becomes positive at pressures above 10 kPa. This is caused by significant adsorption on the surface at this pressure.

4.5 Conclusions

In this work, we have studied the adsorption of argon on zeolite nanosheets and layered zeolite nanosheet structures. Adsorption isotherms from experiments and from simulations of zeolite nanosheets and bulk zeolite were compared, and found to be in good agreement. Defects and impurities are possible causes for increased loading in the experimental part. The simulated zeolite nanosheet isotherm is comparable to the experimental isotherm for higher pressures. We see for layered structures that the adsorption isotherms may not reflect the real structure of the material, but rather internal arrangement of sheets. We show that short distances between sheets cause capillary condensation, and strongly increase adsorption. The calculated surface excess adsorption isotherms support this, and show how the capillary condensation increases the surface excess adsorption. The differences between the isotherm obtained from simulations and from experiments indicate that a specific force field describing the interaction at the external zeolite surface may be required. Surface groups, like silanol, may explain discrepancies, increase condensation on the external surface, as well as increase capillary condensation.

Chapter 5

Thermal Conductivity in Zeolites

This chapter is based on the article: S. K. Schnell and T. J. H. Vlugt: 'Thermal Conductivity in Zeolites Studied by Non-Equilibrium Molecular Dynamics Simulations', Int. J. Thermophysics, 2013, vol 34, pp 1197–1213.

Abstract

The thermal conductivity of zeolites is an important material property. For example, this is the case for catalysis, where chemical reactions release heat either inside zeolites or at zeolite surfaces. At zeolite surfaces, heat is released during the adsorption of guest molecules. Unfortunately, it can be difficult to determine the thermal conductivity of zeolites from experiments or from equilibrium molecular dynamics simulations. Non-equilibrium molecular dynamics (NEMD) simulation is an interesting approach to determine thermal conductivities. Inducing a thermal gradient by moving kinetic energy between different parts of the simulation box, and then studying the resulting thermal gradient, will lead to direct access to the thermal conductivity of the zeolite. In this work, we have used NEMD simulations to determine the thermal conductivity of several pure silica zeolites. The zeolites are modeled using the Demontis force field, making it possible to screen many zeolite frameworks, and study finite size effects. In addition, we have studied the influence of adsorbed guest molecules on the thermal conductivity. The thermal

conductivity of zeolites is usually in order of 0.6 W/m K to almost 4 W/m K, with large differences between different crystallographic directions. We find that the loading of guest molecules adsorbed inside the zeolite has a minor influence on the thermal conductivity, and that in general the thermal conductivity increases with increasing framework density of the zeolite.

5.1 Introduction

Zeolites are microporous crystalline materials. Zeolite frameworks are usually silicon and oxygen based. Silicon and oxygen are present in the ratio 1:2 and organized in tetrahedral building blocks. Using these simple building blocks, a wide variety of zeolite structures can be constructed [15]. These many different structures, with pores, channels, and active sites for catalysis, make zeolites interesting materials for separation and catalytic applications [135, 158, 159]. Zeolite based membranes, where the zeolite has a specific pore-size, can be used as molecular sieves. These membranes can separate mixtures of small molecules such as CO_2, CH_4, H_2S, N_2, and water with high selectivity [12, 138, 160].

One new application of zeolites is as electric insulators in the form of zeolite thin-films. An electric insulator has a low dielectric constant, but at the same time it should be able to transport heat away from the electric components. In addition, it should be chemically stable at operating temperatures. High silica zeolites may have all of these properties [161, 162]. Zeolite thin-films are ordered structures, just a few unit cells thick. These can be created with the desired crystallographic orientation [37]. For a brief introduction on zeolite thin-film applications, we refer the reader to Lew *et al.* [147].

Zeolites themselves are ordered crystals, with micropores, cages, and channels [15]. Much effort has been put into describing and modelling the adsorption and transport of guest molecules inside such systems, see *e.g.* van den Bergh *et al.* [134, 149, 163], Vlugt *et al.* [118, 164, 165], Krishna *et al.* [132, 166–168] and Kapteijn *et al.* [169]. Compared to the quite extensive work on determining adsorption isotherms and diffusivities of guest molecules adsorbed in zeolites, not much work has been put into determining the thermal conductivity of these materials. We will provide a brief description of experimental, theoretical, as well as simulation meth-

ods used to determine thermal conductivities of zeolites. We will emphasize some of the advantages and disadvantages for each method. In addition, we will present the results from some experimental studies, as well as some modelling studies.

5.1.1 Thermal Conductivities from Experiments

The experimental approach typically uses the 3ω-method [170]. This method is applicable for zeolites in their crystal form, as well as for zeolite powders. Powders are compressed into pellets, for which the thermal conductivity is determined. The 3ω-method applies a metallic wire on the zeolite. This wire is used both to heat and to measure the materials response to heating. The response is used to determine the thermal conductivity of the material. Coquil *et al.* [171] have applied this method to measure the thermal conductivity of MEL- and MFI-type thin films, and Fang *et al.* [172] have studied the temperature dependence of the thermal conductivity for the same film types.

Murashov and White [173] measured the thermal conductivity of zeolite 4A (LTA) using a method proposed earlier by the same authors [174]. The method is based on measuring the response to a modulated heat flow directed into a sample. This method is useful for measuring powders with low thermal conductivities. Applying this technique to a dehydrated LTA-type zeolite powder, these authors found a thermal conductivity of around 0.12 W/m K at 300 K. The thermal conductivity of a powder can be significantly lower than for a similar bulk crystal, as there are large resistances to heat transfer between the grains of the powder.

Another zeolite of high industrial importance is faujasite (FAU-type). The version used in experimental work is usually referred to as NaX or zeolite 13X. This structure has been studied extensively by different groups. Jakubinek *et al.* [175] studied the effective thermal conductivity of this framework, for bulk as well as for powders. These authors found a thermal conductivity of 0.15 W/m K for zeolite particles of around 2 µm, and 0.073 W/m K for particles around 800 nm. Liu *et al.* [176] found a thermal conductivity of 0.15 W/m K. These studies also used a powder form of the zeolite, but with unknown particle size. These findings clearly shows the difference in thermal conductivity for the material itself, and the thermal conductivity that can be measured for a powder. A powder will always have a lower conductivity than the bulk zeolite framework.

5.1.2 Modelling

The modelling approach to describe thermal conductivity in zeolites is largely based on the Boltzmann Transport Equation (BTE). The first application of this theory to crystal systems was performed by Callaway [177] and Holland [178]. The analysis is based on phonons, a transport description where energy is transported as a wave in a lattice. Even though this model has advantages, and can provide very good predictions of the thermal transport, there are certain difficulties using it. One needs the Debye temperature of the material in question, as well as the relaxation time of the phonons. Both can be difficult to determine for more complex systems, especially for zeolites, where the structure can be significantly different from ordered structure of metals or dielectrics. For an introduction to this approach, we refer the reader to McGaughey and Kaviany [179]. Even with the difficulties of the BTE, it is an interesting method for studying the transport in materials, and can provide valuable insight into thermal transport in materials. In particular, phonon scattering processes are not well understood for complex materials [180]. For further information about these methods, we refer the reader to the work of Hudiono *et al.* [181], Greenstein *et al.* [180, 182], and Chen and Koplevich [183].

An alternative method to determine thermal conductivities is using Molecular Dynamics (MD) simulations with classical force fields. The thermal conductivity, λ, is usually determined from molecular simulations using the Green-Kubo relation [62, 179]:

$$\lambda = \frac{1}{V k_B T^2} \int_0^\infty \left\langle \frac{\mathbf{S}(t) \cdot \mathbf{S}(0)}{3} \right\rangle \mathrm{d}\, t \tag{5.1}$$

where $\mathbf{S}$ is the heat current vector, T is the absolute temperature, t is time, and k_B is the Boltzmann constant. Most commonly, the thermal conductivity is reported as an average over the three spatial directions:

$$\lambda = \frac{\lambda_x + \lambda_y + \lambda_z}{3}, \tag{5.2}$$

where the direction is indicated by the subscript. For isotropic materials, the thermal conductivities $\lambda_x, \lambda_y, \lambda_z$ in each direction will be the same, while for anisotropic materials the heat current vector will be different in different directions, resulting

in different thermal conductivities in different directions. Green-Kubo relations have the advantage that they can be applied to almost any system. The disadvantage is that the correlation function of Eq. (5.1) decays slowly. To obtain sufficiently accurate results, it will be necessary to run long MD simulations.

McGaughey and Kaviany [184] used Green-Kubo relations, along with classical simulation methods to determine the thermal conductivity in a Lennard-Jones FCC-crystal. Later these authors extended their work to Quartz, SOD-type, FAU-type, and LTA-type zeolite [185]. At 300 K, they described the transport of heat in zeolites by two different mechanisms; (*1*) short length scale conductivity, ≈1.0 W/m K, and (*2*) long length-scale behavior, which is temperature dependent, and of the order of ≈0.4 W/mK (LTA-type) to ≈ 9.0 W/mK in the crystallographic *c*-direction in quartz. Both mechanisms are dependent on the structural properties of the material, the coordination number for silicon, and atomic bond lengths and angles, respectively. For sodalite (SOD-type) zeolite, they found a thermal conductivity of 3.09 W/m K, FAU-type zeolite has 2.00 W/m K, and LTA-type zeolite has 1.61 W/m K. They also studied the temperature dependence of the thermal conductivity in zeolites, and found that the conductivity increases significantly with decreasing temperature.

5.1.3 NEMD Approach

In this work, we use non-equilibrium molecular dynamics (NEMD) to determine the thermal conductivity of zeolites. In this approach, we use MD simulations such that the system is driven out of equilibrium. The advantage of using NEMD simulations, compared to sampling correlation functions, is that they converge much faster. In this case, we create an artificial heat-flux, and study the resulting temperature gradient [186]. The conductivity is then given from Fourier's law:

$$\lambda = \lim_{\mathrm{d}\,T/\,\mathrm{d}\,x \to 0} \frac{-\langle J_q \rangle}{\langle \mathrm{d}\,T/\,\mathrm{d}\,x \rangle} \tag{5.3}$$

where $\mathrm{d}\,T/\,\mathrm{d}\,x$ is the temperature gradient, $\langle \cdots \rangle$ denotes an ensemble average, and J_q is the heat-flux along the gradient. In this way, we are studying a 1-dimensional transport problem, where we can determine the temperature difference caused by the artificial heat-flux.

NEMD simulations have been used previously to determine the thermal conductivities of solids [187], liquids, liquid-liquid mixtures [53, 188–191], and complex systems like biological membranes [192]. Inzoli *et al.* [193] used a similar approach for a MFI-type zeolite with adsorbed *n*-butane guest molecules, using very small system sizes. The focus of that paper was to investigate transport properties in the bulk zeolite. Thermal conductivities for the framework were determined from extrapolating the thermal conductivity to zero loading. No clear change in thermal conductivity was found as a function of loading. In this work, we have used this approach to study the heat transport in different crystallographic directions of pure zeolite crystals, as well as the conductivity of MFI-type zeolite with argon and *n*-hexane adsorbed, and FER-type zeolite loaded with argon. NEMD simulation is an effective method to study thermal conductivity. Therefore, it is possible to study many frameworks, finite-size effects, as well as how the anisotropy of the zeolite framework leads significantly different thermal conductivities in different crystallographic directions.

5.1.4 Outline

This chapter is organized as follows: in Section 5.2 we present the simulation procedure applied in this work. In Section 5.3 we provide details on the simulations and the used force field. In Section 5.4 we present the results we find for different zeolite frameworks. Finite-size effects are investigated, we tabulate the thermal conductivities for several zeolite frameworks in different crystallographic directions, and we study the dependence of loading on the thermal conductivity in the zeolite frameworks. In Section 5.5 our findings are summarized.

5.2 NEMD Simulation Method

There are several methods that can be used to set up simulations with a heat flux in a MD simulation. In this work we have chosen the method originally described by Müller-Plathe [186] as the basis for our simulations. The simulation box was divided into one hot and one cold zone, see Fig. 5.1. At certain intervals, the hottest particle in the cold zone and the coldest particle in the hot zone of the same type will exchange velocity. This ensures that the total energy and linear momentum of

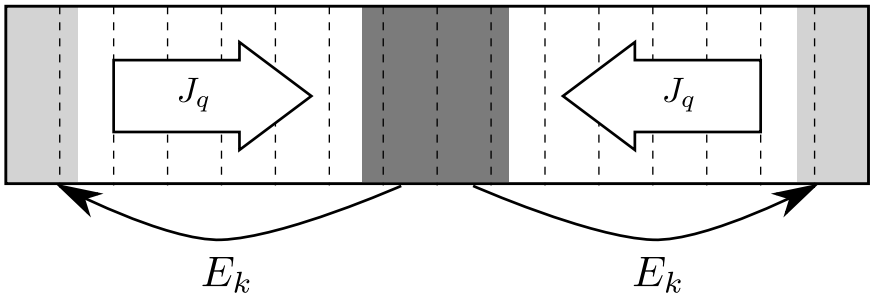

Figure 5.1: Schematic representation of the simulation setup used in this work. The high-temperature regions (light grey) are on the outer edges of the simulation box, and the low-temperature region (dark grey) is in the middle. Periodic boundary conditions connect the two high-temperature regions, so for practical purposes, this is the same region. The heat-flux is induced by moving kinetic energy, E_k, from the low-temperature region (dark grey) to the high-temperature region (light grey) using virtual collisions (as described in the main text). This will result in a heat-flux, J_q, from the high-temperature region to the low-temperature region. At steady state, the transported kinetic energy will be equal to the heat flux. The temperature profile can be directly calculated from the number of particles, and kinetic energy in each layer. Different layers are indicated with dashed lines.

the whole system is conserved. We can apply normal periodic boundary conditions and normal integration schemes. The system can be equilibrated using regular thermostats.

The original method as presented by Müller-Plathe [186] has two shortcomings that should be handled in order to use the method efficiently for zeolite frameworks with adsorbed guest molecules: (*1*) the swap of velocities is only defined between non-bonded particles, and (*2*) the velocity swaps are taking place between particles of the same type, more specifically, the same mass. In addition, we want to allow for exchanges to take place without having to search for the particles with highest and lowest kinetic energy. In this way, the perturbation in performing a velocity-swap will be reduced, and it is possible to use a higher frequency for these swaps.

To overcome these limitations, we used the method proposed by Lussetti *et al.* [191] to perform velocity swaps between more complex molecules. Individual atoms in a molecule can be used to exchange heat between the hot and cold zones, provided that the intra-molecular bonds are flexible. For molecules, or segments

of molecules where bonds are constrained, the velocity exchange can be performed on the center of mass velocities of the whole groups. To allow the velocity swap to take place between two particles with different mass, we use the method described by Nieto-Draghi *et al.* [55, 194]: two selected particles (one in the hot zone, and one in the cold zone) are involved in a virtual elastic collision. The velocities of the two particles (masses m_1 and m_2, and initial velocities $\mathbf{v}_1$ and $\mathbf{v}_2$) after the virtual collision are:

$$\begin{aligned}\mathbf{v}_2' &= \frac{2m_1\mathbf{v}_1 + (m_2 - m_1)\mathbf{v}_2}{m_1 + m_2},\\ \mathbf{v}_1' &= \frac{2m_2\mathbf{v}_2 + (m_1 - m_2)\mathbf{v}_1}{m_1 + m_2}.\end{aligned} \tag{5.4}$$

We see from Eq. (5.4) that if $m_1 = m_2$, we obtain the original velocity exchange method as described by Müller-Plathe. It is important to note that in the original method described by Müller-Plathe, the criterion for a virtual collision to take place is that we find the two extremes: the hottest particle in the cold zone, and the coldest particle in the hot zone. Exchanging velocities between these two particles will always lead to an 'artificial' flux going from the cold to the hot part of the simulation box. The response of the system is a heat-flux going from the hot to the cold zone. At steady-state, these two are equal. In our simulations, particles are selected at random in the hot and cold zone. Therefore, the difference in kinetic energy is on average smaller than for the approach of Müller-Plathe (where the largest possible energy difference is always selected). We impose the criterion that the artificial flux must always go from the cold to the hot side if a virtual collision is to take place. If two particles are selected and this criterion is not met, the exchange is rejected and two new particles are selected at random until a suitable pair is found. In this way, we can have a higher frequency for the virtual collisions, and the instantaneous change in energy will be smaller than deliberately searching for the extremities.

The heat-flux is calculated from:

$$\langle J_q \rangle = \frac{1}{2A\tau} \sum_{\text{exchanges}} \frac{m_1(\mathbf{v}_1'^2 - \mathbf{v}_1^2)}{2}, \tag{5.5}$$

where τ is the time over which we sample the system, and A is the cross-section

area of the simulation box (perpendicular to the flux-direction). This area has to be counted twice, since the system is symmetric around the center of the box. The temperature profile in the system can be calculated from the average kinetic energy of the particles. The system is divided into a number of slabs, see *e.g.* Fig. 5.1. The temperature in one such slab is then:

$$T_i = \frac{1}{3\langle N\rangle k_B}\langle \sum_{j}^{\text{particles}} m_j \mathbf{v}_j^2\rangle \tag{5.6}$$

where N is the total number of particles present in a slab averaged over the whole simulation, and we sum over all particles present in the whole slab.

5.3 Simulation Technique

The NEMD simulations were performed in the microcanonical ensemble (constant N, V and E). The system was kept at a temperature of 350 K during the initialization procedure, and equilibrated properly in the NVE ensemble, obtaining a steady-state before the sampling took place. The initial positions of the zeolite atoms were obtained from the IZA database [15]. A constant heat-flux was obtained early in the equilibration. The timestep for integrating the equations of motion was 0.001 ps, and the averages were sampled every 10TH timestep. The virtual collisions were attempted every 200 or 500 timesteps. This resulted in a clear constant temperature gradient between the hot and cold zones. Given that the average heat flux is constant, the linear temperature profile shows that the thermal conductivity is constant over the range of temperatures in the system. In this way, Fourier's law can be applied to the system in itself. The linear response of the system was tested by doubling the frequency of virtual collisions. This resulted in a doubling of the observed temperature gradient. Unless otherwise stated, the hot and cold layer were in total 10 % of the length of simulation box in the direction of transport.

The zeolite was modelled using the Demontis force field for zeolites [195]. We applied the slightly modified force field described by Vlugt and Schenk [118]. The

interactions between Si and O in the system is described as harmonic springs:

$$V_{\text{Si-O}}(r) = k_{\text{Si-O}}(r - r_{\text{o,Si-O}})^2, \tag{5.7}$$

$$V_{\text{O-O}}(r) = k_{\text{O-O}}(r - r_{\text{o,O-O}})^2, \tag{5.8}$$

where $r_{\text{o,Si-O}}$ and $r_{\text{o,O-O}}$ are the equilibrium bond lengths, $k_{\text{Si-O}}$ and $k_{\text{O-O}}$ are the spring constants. We take $k = k_{\text{O-O}} = k_{\text{Si-O}}/5 = 50\,000\,\text{K}\,\text{Å}^{-2}$. It is necessary to assess the importance of the values of the spring constants.

For simulations with argon and *n*-hexane, we used the force field parameters from Dubbeldam *et al.* [65] for a united-atom representation of *n*-hexane. Intramolecular interactions of *n*-hexane consisted of bond-stretching, bond-bending and torsion. Lennard-Jones interactions were calculated between beads of the guest molecules and the oxygen atoms of the framework. Guest-guest interactions were also described by Lennard-Jones interactions. For more details on the force field, we refer the reader to the paper of Dubbeldam *et al.* [65]. The argon-argon and argon-zeolite interactions were similarly taken from García-Pérez *et al.* [103].

5.4 Results and Discussion

In Fig. 5.2, we have plotted the thermal conductivity as a function of the spring constant. These results are for the MFI-type framework, and we have only looked at the transport in *y*-direction. We clearly see the increasing thermal conductivity with increasing spring constants. The rapid increase goes on until k/k_B becomes approximately 50 000 $\text{K}\,\text{Å}^{-2}$, from there, the conductivity does not increase as steeply. We find that for MFI-type framework, k/k_B of 50 000 $\text{K}\,\text{Å}^{-2}$ leads to a reasonable value of around 1 W/m K. Experimental data indicates that MFI-type zeolite has a thermal conductivity between 0.8 W/m K as a lower estimate, to 1.5 W/m K as a higher estimate [171, 182, 193].

5.4.1 Finite-size Effects, and Effect of the Size of the Hot and Cold Zones

There are significant finite-size effects present when the zeolite crystals are studied using NEMD simulations. Because of the symmetry in the setup of the simulation box, increasing the simulation box with two unit cells only leads to one unit cell extra

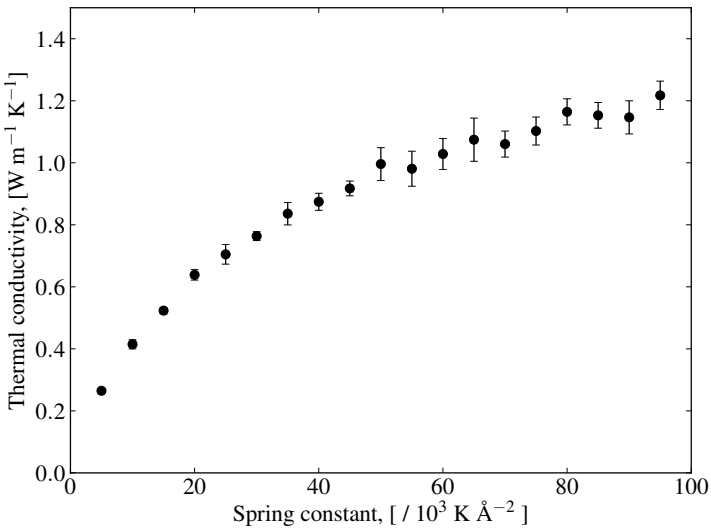

Figure 5.2: Thermal conductivity of all silica MFI-type zeolite in the y-direction. The thermal conductivity is plotted as a function of the spring-constant, k/k_B. The system size in this case was 8 unit cells. Even though this is not sufficiently large to overcome all finite-size effects, it still indicates that the spring-constant has a large effect on the thermal conductivity of the framework. Experimental results for MFI-type zeolite vary between 0.8 W m^{-1} K (Greenstein *et al.* [182]) to over 1.4 W m^{-1} K (Inzoli *et al.* [193]). A spring constant of 50 000 K Å^{-2} was used in the remainder of this work.

in the transport zone. In Fig. 5.3 we have plotted the finite-size effect of MFI-type, as a function of the simulation box length in the direction of transport. In addition, we have tested the effect of using larger parts of the system for virtual collisions. In general, for this we used 10 % of the system in all cases in this work. From Fig. 5.3 we see that changing this to 20 % has no effect on the calculated thermal conductivity. Even with a flexible zeolite model, the particles in the framework only move a little around their equilibrium position. Therefore, there are always sufficient particles to exchange energy with. In fact, we have not yet observed that an exchange has not been performed because none of all possible pairs of molecules could successfully perform a virtual collision. At the same time, we tested the finite-size effect by

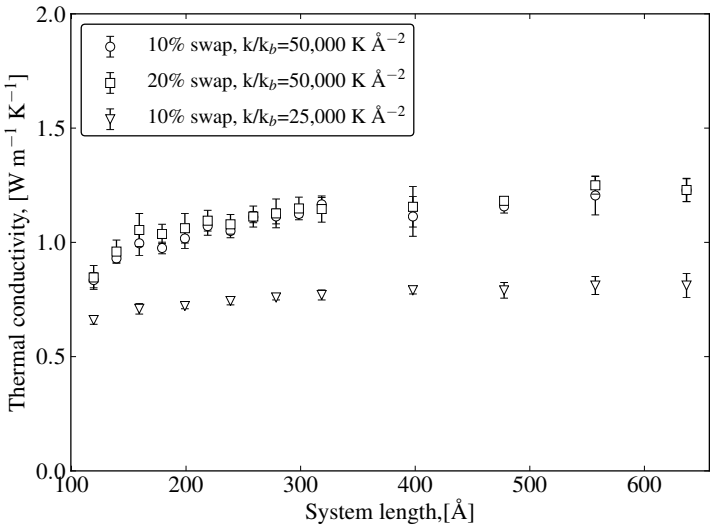

Figure 5.3: Thermal conductivity in MFI-type zeolite as a function of box-length in the y-direction. The thermal gradient is constructed in the y-direction. The simulation box was 2 and 3 unit cells in the x- and z-direction, respectively. Three different system configurations have been tested: one where 10 % of the box-length is used for virtual collisions, one where 20 % of the box-length is used for virtual collisions, and one where the spring constant of the force field is reduced from 50 000 KÅ^{-2} to 25 000 KÅ^{-2}, while 10 % of the box is used for virtual collisions. We see how the size of these zones has no significance on the thermal conductivity, while using a smaller spring constant, we see that the finite-size effect is smaller than for the systems with larger spring constants.

changing the spring constant, k. We see how a lower value of k leads to a faster convergence to a constant value. In all these systems, we have plotted the thermal conductivity as a function of the number of zeolite unit cells in the direction of transport.

In Fig. 5.4 we have plotted the finite size scaling of VSV- and MFI-type framework in x-, y-, and z-direction. The finite size effect is clear in all cases. Increasing the size of the simulation box leads to an increase in the thermal conductivity. The

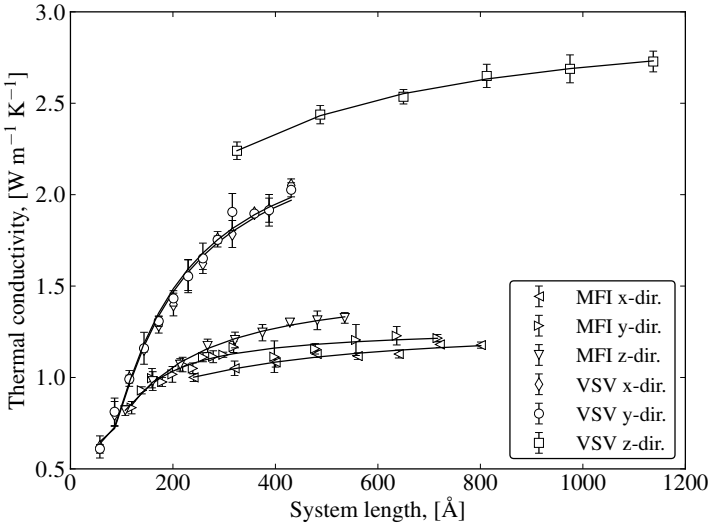

Figure 5.4: The finite size scaling of the thermal conductivity λ for MFI- and VSV-type zeolites. We clearly see the significant finite-size scaling effects in some of the zeolite systems. The results for VSV-type zeolite, having almost equal length in x-, and y-directions (7.179 Å), with a comparatively long z-direction (40.620 Å), clearly show how λ is related to the size and shape of the unit cell. MFI-type zeolites have smaller differences (20.022 Å,19.899 Å, and 13.383 Å in x-, y-, and z direction respectively). In all simulations, the directions perpendicular to the temperature gradient was at least 24 Å each. The black lines are the result of fitting the results to Eq. (5.9).

black lines show the data fitted with the function:

$$\lambda = \lambda_\infty + \frac{\beta}{L} + \frac{\gamma}{L^2} \tag{5.9}$$

where λ_∞ is the thermal conductivity in the thermodynamic limit, and β and γ are fitted parameters. Eq. (5.9) can describe the computed λ quite well. Fitting with this equation leads to a good representation of the obtained simulation data.

What is evident from Fig. 5.4 is that the finite size scaling depends on the actual size of the unit cell. The results for VSV-type frameworks, which have a long unit cell length in z-direction, clearly show that the finite-size effect is reduced quickly.

A certain length of the system is necessary to obtain a good estimate of the thermal conductivity, but using the simple interpolation given with Eq. (5.9), we can obtain an accurate estimate of the value in the long range limit.

Finite-size scaling effects should be taken into account for thin-film applications of zeolites. Our results show that there can be significant finite-size effects for systems smaller than 200 Å. This is for example the case in the work of Choi *et al.* [21], where the synthesized zeolite thin-film is approximately 20 Å thick.

5.4.2 Thermal Conductivity

In Table 5.1 we present the computed thermal conductivity for a selection of pure silica zeolite frameworks in the crystallographic x, y, and z-directions. The frameworks used were simulated for several different lengths. If the unit cell direction is long, then fewer unit cells are necessary in the direction of transport. The data were all fitted to Eq. (5.9), and the value for the thermodynamic limit, λ_∞ is reported in Tab. 5.1. The estimated error in the thermal conductivity is less than 10 % in all cases (estimated from 5 independent simulations of the same system). For isotropic zeolites, the structure of the crystal is the same in all directions, the thermal conductivity was found to be equal in all directions.

For SOD-type frameworks, we find a thermal conductivity of 1.2 W/m K. This is significantly lower than the conductivity of 3.09 W/m K determined by McGaughey and Kaviany [185] from equilibrium MD simulations. Also for FAU-type framework, as well as LTA-type zeolite we find a significantly lower thermal conductivity, with 1.09 W/m K and 1.20 W/m K compared to 2.00 W/m K and 1.61 W/m K respectively from McGaughey and Kaviany [185]. The thermal conductivity of LTA-type zeolites have also been determined experimentally by Greenstein *et al.* [180]. Their results are however for crystalline LTA-type framework, with non-framework anions. These authors found the thermal conductivity to vary between 0.8 W/m K with K^+ cations, to 1.2 W/m K with Na^+ cations. This is quite good agreement with 1.09 W/m K determined using NEMD simulations.

For MFI-type zeolite frameworks, there are several different studies available in literature. Greenstein *et al.* [182] find thermal conductivities between 0.8 and 1.0 W/mK for calcined polycrystalline films, while it is between 1 and 1.5 W/m K for uncalcined MFI. Coquil *et al.* [171] found MFI thin film thermal conductivities

Table 5.1: Thermal conductivity for different zeolite framework types. All frameworks are modelled as pure silica frameworks. The isotropic frameworks are given for the x, y, and z direction as one single value. There can be quite large differences in thermal conductivity between the different crystallographic directions for some anisotropic frameworks. In FER-type zeolite, we observe a difference of more than 2 W/m K between the x- and z-direction.

Framework	λ_x [W/m K]	λ_y [W/m K]	λ_z [W/m K]
AFR	0.75	0.73	0.82
BEA	0.80	0.80	1.01
BOG	1.16	0.93	1.00
CHA	0.91	1.16	1.04
EAB	0.76	0.71	0.78
EUO	2.20	1.39	1.82
FER	1.18	2.50	3.62
GME	0.90	0.90	0.95
LEV	0.95	0.89	0.93
MEI	0.67	0.61	1.04
MER	1.01	1.05	0.87
MFI	1.29	1.28	1.54
MFS	2.57	1.53	1.31
MTT	3.38	1.77	1.89
OFF	0.78	0.73	0.94
TON	1.81	1.84	2.98
VSV	2.50	2.51	3.01
ANA		2.55	
FAU		1.09	
KFI		0.98	
LTA		1.20	
SOD		1.17	

between 0.93 to 1.12 W/m K. These results are in agreement with the result obtained here. In the x- and y- directions, we find that the crystal has a thermal conductivity of approximately 1.29 W/m K and 1.28 W/m K. In z-direction, we find it to be

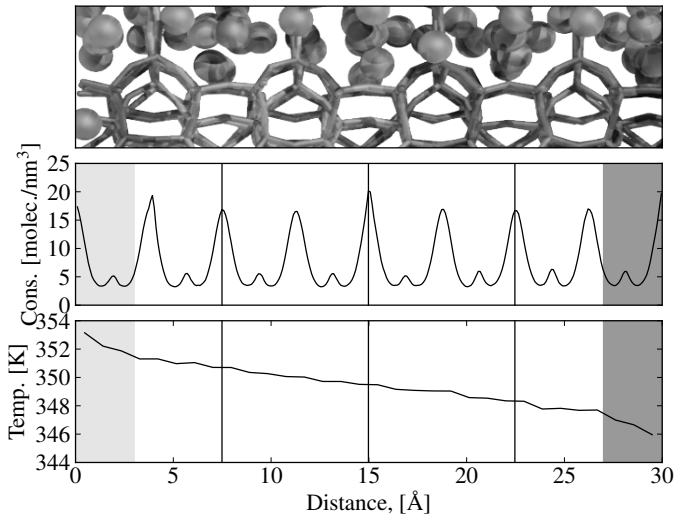

Figure 5.5: The temperature profile, and structure of FER-type zeolite. The temperature gradient is applied in the z-direction of the zeolite. The figure shows the temperature profile, density profile and zeolite with argon molecules adsorbed. There are approximately 15 argon molecules per unit cell. The black vertical lines outline the positions of the boundaries of the unit cells. The x- and y-direction of the simulation box are 38.312 Å and 28.254 Å respectively. The hot and cold zone are indicated with the grey squares on the lower part of the figures.

0.82 W/m K. We have found no experimental data on the thermal conductivity in specific directions in the MFI-framework.

We find the highest thermal conductivity for FER-type frameworks in z-direction, with λ_z = 3.63 W/m K. The x-direction of the same crystal only has a thermal conductivity of 1.18 W/m K. From Table 5.1 we see there can be significant differences in the thermal conductivity in different crystallographic directions.

In Fig. 5.5 we show the temperature profile in FER-type zeolite, where the distance is given in the z-direction. The top part of the figure shows a snapshot from the simulation. The zeolite unit cell are marked with the vertical black lines in the bottom part of the figure, also showing the temperature profile for this system. Fig-

ure 5.5 shows a step-pattern in the temperature profile. This step-pattern can be seen for some other zeolite structures, in some crystallographic directions as well, but the FER-type zeolite has the most distinct pattern. This is caused by the small number of silicon-oxygen bonds between different parts of the zeolite as heat can only be transferred through bonds in this model. Different unit cells are connected with few silicon-oxygen bonds, that seems to hamper the transport of heat. The middle part of the figure shows the density profile in the zeolite. In this case, the step-like pattern in the temperature-profile is slightly reduced, but not removed.

5.4.3 Thermal Conductivity for Zeolites with Adsorbed Molecules

In Fig. 5.6 we have plotted the thermal conductivity of the zeolite framework as a function of the loading of guest molecules (argon or *n*-hexane). We considered the relative loading, taking the maximum loading of argon to be 31.15 molecules/u.c., and the maximum loading of *n*-hexane to be 8 molecules/u.c. From the figure, we see that the adsorption of molecules hardly changes the thermal conductivity of the zeolite. This is in agreement with the results presented by Inzoli *et al.* [193]. In their work, they found that the adsorbed molecules have minor impact on the thermal transport in zeolite frameworks. However, the simulations of Inzoli *et al.* [193] were performed for much smaller systems and will therefore suffer from significant finite-size effects.

For the FER-type framework, there is slight increase in the thermal conductivity at higher loadings, but this effect is quite small. Also, this framework has the step-patterns in the thermal conductivity, that act as internal resistances towards heat transfer. The small effect of the loading of guest molecules on these steps indicates that the loading has a small effect on the thermal conductivity.

In the work of Griesinger *et al.* [196], the thermal conductivity of different zeolites with different loading of gases was studied experimentally, focusing on hydrogen, helium, argon, nitrogen, and air. These authors found a significant increase in the thermal conductivity for increasing loading, in some cases by orders of magnitude. These studies were performed using a transient wire method. It is possible that in zeolite system, based on powders, the adsorbed gas helps transport heat between zeolite grains. These boundaries between particles will act as significant resistances to heat transfer.

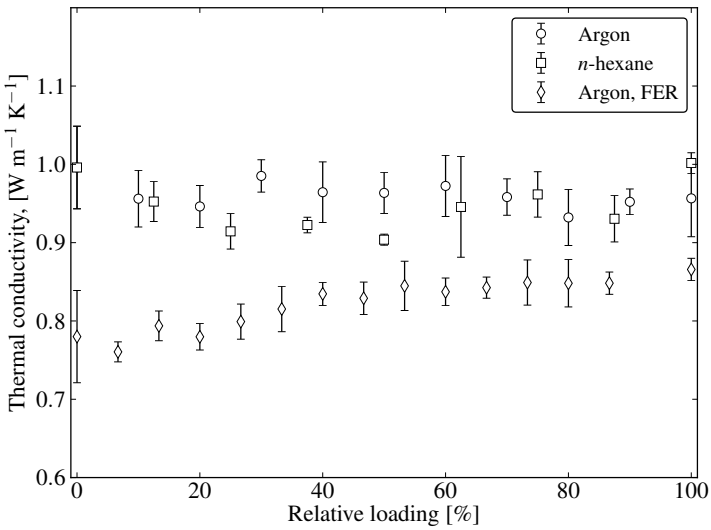

Figure 5.6: The thermal conductivity of MFI-type zeolite as a function of the relative loading of adsorbed molecules. For argon in MFI-type, the maximum loading is set to 31.25 molecules per unit cell. For *n*-hexane in MFI-type framework, the maximum loading is set to 8 molecules per unit cell. The thermal gradient is applied in the *y*-direction. For FER-type zeolite the maximum loading of argon is set to 15 molecules per unit cell. The thermal gradient is applied in the *z*-direction for the FER-type framework. For FER-type zeolite, we observe a very small increase in the thermal conductivity with increasing relative loading, while for MFI-type zeolite, there is no significant change in the thermal conductivity with increasing loading.

5.4.4 Framework Density

In Fig. 5.7 we have plotted the thermal conductivity as a function of the framework density. The density is given as atoms (Si and O) per nm^3. The thermal conductivity is given as the average value for the crystal, according to Eq. (5.2). From this figure we clearly see how most of the structures lump together with thermal conductivities around 1 W/m K. The zeolites with highest conductivity are also among the zeolites with highest density. However, at approximately the same density there are several structures with significantly lower thermal conductivity. LTA-type and FAU-type

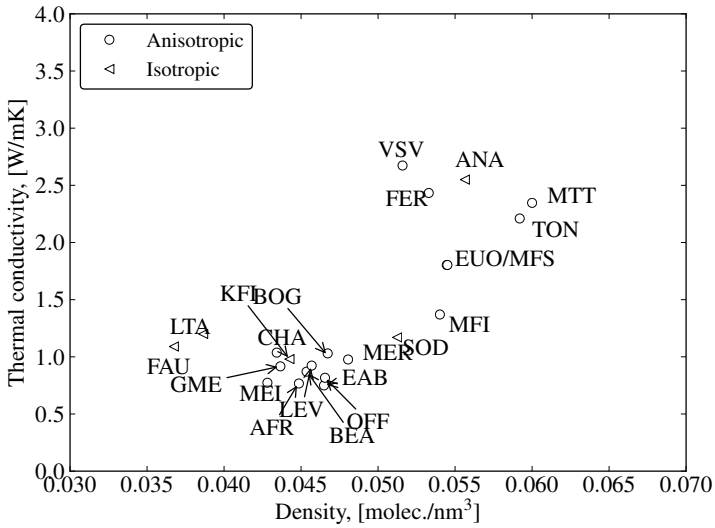

Figure 5.7: Thermal conductivity of zeolites as a function of the framework density. For anisotropic frameworks we have calculated the framework thermal conductivity, see Eq. (5.2). We can observe an increase in the thermal conductivity for higher density frameworks.

zeolite have the lowest density of the zeolites we have tested in this work, but still the thermal conductivity is about the same as for the main group. There are no clear distinction between the isotropic and anisotropic structures.

5.5 Conclusions

We have studied the thermal conductivity of several all-silica zeolite framework types using non-equilibrium MD simulations. We find that using even the simple Demontis force field for zeolites gives a good description of the thermal conductivity. In addition, force field is computationally cheap, making it easy to screen several zeolite framework types and studying finite-size effects. We found that the thermal conductivity has significant finite-size effects. The finite-size scaling depends on the length L of the system, and can be described using a second order expansion in

$1/L$. The thermal conductivity strongly depends on the crystallographic direction of the zeolite. This is best seen in FER-type zeolite, where the thermal conductivity is three times larger in the z-direction than in the x-direction. At the same time, the addition of guest molecules in the framework is found to have little effect on the overall thermal conductivity. Among the zeolites with highest thermal conductivity, several of these have a high framework density. There is however no clear relationship between the structure, and the resulting thermal conductivity.

Chapter 6

Non-Equilibrium Transport of Heat and Mass Across a Zeolite Membrane

This chapter is based on the book-chapter 'Non-Equilibrium Thermodynamics for the Description of Transport of Heat and Mass Across a Zeolite Membrane', by S. K. Schnell, T. J. H. Vlugt and S. Kjelstrup, From the Book: 'Handbook of Membrane Reactors: Fundamental Materials Science, Design and Optimisation (Volume 1)' edited by Angelo Basile. ISBN-13: 978-0-85709-414-8.

Abstract

Non-equilibrium thermodynamics offers a better and more precise way to describe transport of heat and mass over membranes then the simple Fick's and Fourier type models. In this work we derive the equations for single component transport (of *n*-butane) across a zeolite membrane. We use Non-equilibrium molecular dynamics (NEMD) data to show how phenomena are related. Significant differences are documented between this method, and methods invoking Fick's and Fourier's law.

6.1 Introduction

A precise description of membrane transport phenomena requires detailed attention to the surface of the membrane, as well as to the membrane itself [47]. Before or after transport through the membrane, the component to be transported can be more or less strongly adsorbed to the membrane interface. The transported component may also be involved in a chemical reaction at the interface. Such phenomena are usually closely related to the exchange of heat, meaning that there are sinks or sources for heat present at the membrane external surface. This surface is of molecular thickness, and it is therefore to be expected that the mass flux is affected by the heat flux through the membrane, and also that these fluxes vary with position in the membrane. Nevertheless, in chemical engineering the transport of heat and mass is usually described using Fourier's law and Fick's laws, which do not include such effects. We consider a series of layers, from a homogeneous gas-phase on the 'feed' side, to a homogeneous gas-phase on the 'permeate' side. The boundary layers are of macroscopic thickness. We will here distinguish such macroscopic boundary layers from a molecularly thin interface, and consider five regions of transport, namely the homogeneous phases of the macroscopic boundary layers, the interface layers between each homogeneous phase and the membrane phase, called the surface, and the membrane phase itself.

In the modelling of membrane separations, knowledge of chemical potentials and temperatures is required for the adjacent homogeneous phases and the membrane. The surface is often assumed to be at equilibrium, making these properties continuous at the surface. With large mass fluxes and/or large heat productions at the surface, these assumptions may no longer be correct and more traditional descriptions using Fick's and Fourier's laws will fail to capture the correct behaviour. In this case, one must use the theory of irreversible thermodynamics to correctly describe heat and mass transfer [47, 50].

The purpose of this chapter is to present such a description, to identify the effects and consequences of coupling heat and mass transport, and to study the commonly used assumption of equilibrium at the interface at steady state conditions. The simple transport of a single component through a membrane is used as an example. A typical alkane, *n*-butane, is chosen as the component to be transported, and silicalite-1 [15] is used as membrane material. Membrane reactors using

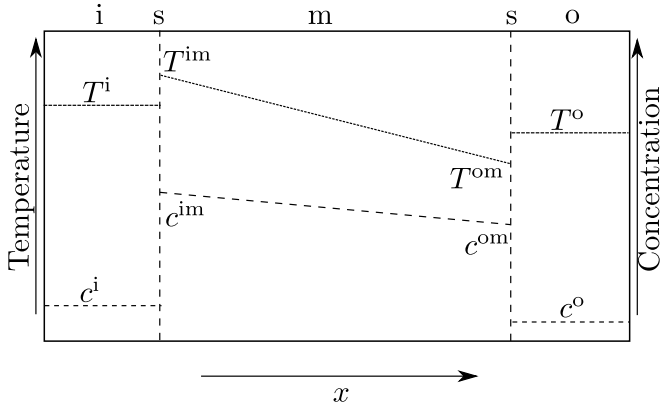

Figure 6.1: Schematic representation of the system studied here. At the surface, jumps in temperature and concentration, of guest molecules occur. For simplicity, it is assumed that temperature and concentration gradients inside the membrane are constant. The membrane is denoted by *m*; *i* and *o* denote the pure gas-phase (also considered as the 'feed' and 'permeate' side respectively). The surfaces are denoted by *s*. The superscripts *im* and *om* denote the temperature and concentration in the membrane on the *i*- and *o*-side.

zeolites are well studied; see for example a recent review [158]. Most importantly, all transport coefficients for heat and mass transfer are already available for this system; see the work of Inzoli *et al* [35, 197]. In this work, molecular dynamics simulations were used to obtain the transport coefficients. Equilibrium data needs to be supplied, in order to be able to define the driving forces for transport. To the best of our knowledge, this is the first time data obtained from molecular dynamics simulations have been used exclusively to accurately model the transport through a heterogeneous system under non-equilibrium conditions at the surface.

6.1.1 A Zeolite Membrane in Equilibrium with a Gas

A zeolite membrane separating two gas-phases is in the thermodynamic sense a heterogeneous system composed of five subsystems. This is illustrated in Fig. 6.1. Two of these, the two gas-phases, are homogeneous, three-dimensional systems. The membrane can also be regarded as a homogeneous phase on a scale in units

of length of two zeolite unit cells [72] with gas absorbed in the various channels. The two external surfaces, or the transition zones of molecular thickness between gas and zeolite membrane, are the fourth and fifth thermodynamic systems. The surfaces are two-dimensional systems, defined according to Gibbs, with excess properties as state variables [47]. We will use the word surface or interface to indicate this type of thermodynamic system.

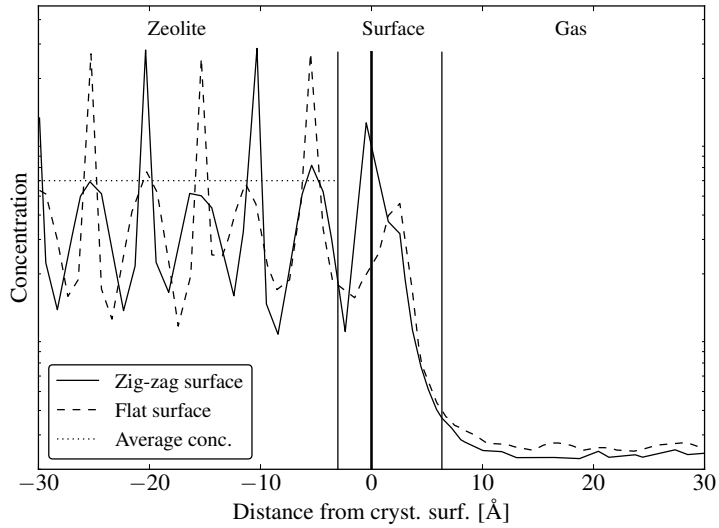

Figure 6.2: *n*-Butane local density near a gas-zeolite interface. The density profiles are given in arbitrary units, to illustrate the density fluctuations inside such a zeolite. Density profiles are shown for (*a*) a flat surface cut between the sinusoidal channels, and perpendicular to the straight channels and (*b*) a textured surface, where the cut is in the sinusoidal channels, and also here, perpendicular to the straight channels. For macroscopic applications, the average concentration over several unit cells is a more convenient measure for the concentration in the zeolite.

Figure 6.2 shows the density profiles of *n*-butane in the zeolite and close to the surface at equilibrium. The local density of guest molecules in the zeolite strongly varies with position in the zeolite. In the work of Inzoli *et al.* [35, 193], the external surface has two different surface structures; one where the surface is cut between

the sinusoidal channels, and the other one across the sinusoidal channels. This shifts the density profile as seen in Fig. 6.2, and these represent two quite different surface structures. Inzoli *et al.* [35] showed that for this system the details of the surface structure have a minor influence on the surface resistance to transport.

Equilibrium adsorption isotherms for gases and gas mixtures are in general well known for bulk zeolite systems, experimentally as well as computationally [66, 106, 198]. We have used established procedures to obtain equilibrium adsorption isotherms data [62], which are needed to describe transport problems in our case. Thermodynamic adsorption data is obtained using Configurational-bias Monte-Carlo simulations in the grand-canonical ensemble [62]. Interactions between atoms and molecules are described using a classical force field [66]. Figure 6.3 shows adsorption isotherms for *n*-butane adsorption in silicalite-1 at a temperature from 320 K to 400 K, which is the range of temperatures represented by coefficients given by Inzoli *et al.* [35, 197]. In Fig. 6.3 we have plotted the loading of *n*-butane in the zeolite (in molecules /nm^3) as a function of the fugacity. In this work we take the fugacity coefficient to be one. The isotherms are well described with a Langmuir model [199] with a maximum loading of approximately 1.7 molecules /nm^3. The silicalite-1 is oriented so the straight channels face out in the gas-phase. This is one of the most interesting orientations for this crystal, and effort has been put in place for producing membranes with only this crystallographic orientation; see for example the work of Lee and Jeong [37].

6.1.2 Transport Across a Heterogeneous System

When a fluid with one or more components is transported across a selective membrane, concentration gradients arise in the layer immediately outside the membrane. Likewise, due to negative or positive enthalpies of adsorption in the membrane, temperature gradients will arise, depending on the ratio of the relative conductivity of the membrane to its surroundings [35]. In a pure gas, there is obviously no composition gradient, only a temperature gradient. With pores of molecular size, the zeolite becomes a component in the thermodynamic sense. A concentration gradient inside a zeolite can thus be maintained in the presence of a temperature gradient. We will investigate the stationary state transport of one component through the membrane.

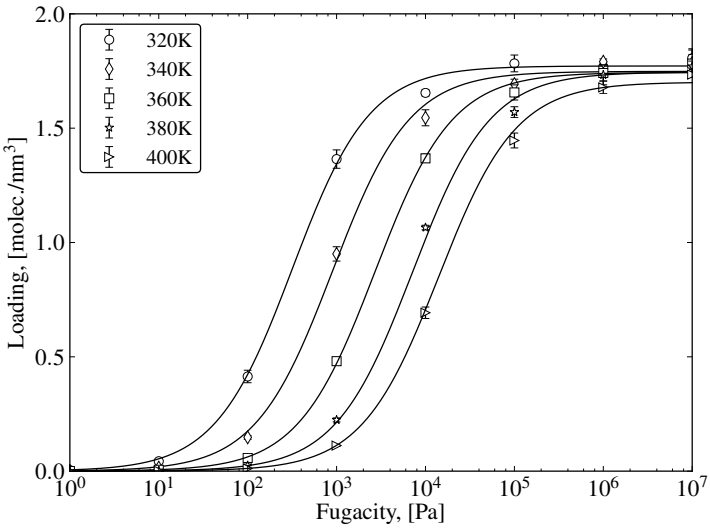

Figure 6.3: Adsorption isotherms of *n*-butane in a bulk zeolite crystal with periodic boundary conditions, without an interface. Therefore, no gas—zeolite interface was present here. The temperature range is selected to be in the range of the operating conditions of such a membrane system. In all cases, the isotherms are well described using a Langmuir single site isotherm [199].

Typical profiles of the intensive variables, such as chemical potential, μ, and temperature, T, are illustrated in Fig. 6.1. At the interface during transport, a possibility arises to maintain a difference in chemical potential between the two phases adjacent to the interface; this means that the interface is not in equilibrium under such conditions, *cf.* a similar discussion of liquid-vapour interfaces of Ge *et al.* [200]. Likewise, a temperature difference can be maintained across the interface. We will study the details of this situation, that is, what are the causes of such jumps, what do they physically mean, and how can we take advantage of them? We will also examine the assumption of continuity of intensive variables at the interface: what does it mean in practice to have the correct non-equilibrium description of the surface? This work can be seen as a step in the direction of analysing multicomponent

systems using realistic transport coefficients.

6.2 Fluxes and Forces from the Second Law and Transport Coefficients

6.2.1 Fluxes and Forces from the Second Law

The theory of non-equilibrium thermodynamics is used to analyse the questions above. The sections below provide the essential steps in such a description. The detailed background and explanation of the theory, as set up for heterogeneous systems, can be found elsewhere [47]. The same symbols are used as in this reference.

The Equations for Transport of Heat and Mass

In the theory of non-equilibrium thermodynamics, the fluxes and forces pertinent to the system are derived from the entropy production per volume or area element. The entropy production is formulated using the assumption that there is local equilibrium in the system. This assumption is surprisingly valid even for systems with very large gradients [201]. The expression for the entropy production follows by introducing mass and energy-balances into the Gibbs equation. In the present case, the mass and energy-balances are simple, as the mass and total energy fluxes, J and J_q, respectively, are constant and directed along the x-axis only:

$$J^i = J^m = J^o = J, \tag{6.1}$$

$$J_q'^i + J^i H^i = J_q'^m + J^m H^m = J_q'^o + J^o H^o = J_q. \tag{6.2}$$

Superscripts m, i and o denote that the location is the membrane, the i-side (feed) or o-side (permeate) surfaces; see Fig. 6.1. The flux of n-butane is denoted by J; the sensible heat flux is J_q' [47] and H is the molar enthalpy of n-butane. The total energy flux is J_q. We distinguish between the sensible heat flux and the total heat flux. The sensible heat flux is the one that can be measured directly, and is described by Fourier's law in a pure component. The total heat flux is the sensible heat flux, and in addition the enthalpy carried by mass transport. The definitions of the various types of heat fluxes are described and explained in detail in Kjelstrup and

Bedeaux [47]. The entropy production and the corresponding force-flux relations for the zeolite membrane and its two surfaces are discussed in the next section.

The Zeolite Membrane

As discussed in Section 6.1.1, we can regard the zeolite membrane as a homogeneous phase. Strong evidence has been obtained that it is meaningful to consider thermodynamic variables in volume elements as small as a single unit cell, also when the system is exposed to large gradients [47, 72]. The entropy production σ is:

$$\sigma = J'^{m}_{m} \frac{\mathrm{d}}{\mathrm{d}x}\frac{1}{T} + J\left(-\frac{1}{T}\frac{\mathrm{d}}{\mathrm{d}x}\mu_T\right). \tag{6.3}$$

We define the fluxes into the membrane as positive, and use the membrane as the frame of reference for all fluxes. The driving forces for transport of heat and mass are the gradients in inverse temperature T, and minus the gradient in chemical potential, μ_T, taken at constant temperature. The fluxes conjugate to these forces are those of *n*-butane and sensible heat. The force-flux relations that follow from this are (see also Chapter 1.3):

$$\frac{\mathrm{d}}{\mathrm{d}x}\frac{1}{T} = r^{m}_{qq} J'^{m}_{q} + r^{m}_{qm} J, \tag{6.4}$$

$$-\frac{1}{T}\frac{\mathrm{d}}{\mathrm{d}x}\mu_T = r^{m}_{mq} J'^{m}_{q} + r^{m}_{mm} J. \tag{6.5}$$

In Eq. (6.4) and (6.5) the resistivities are denoted by the symbol r, and the superscript denotes that these relate to the membrane, while the subscript identifies the type of resistivity. The diagonal resistivities, r_{qq} and r_{mm} can be related to the conductivity and diffusivity respectively, while the off-diagonal resistivities describe the coupling between heat and mass transfer. Also, the mass flux is denoted by J, and the sensible heat flux is denoted by J'^{m}_{q}. We have chosen to use the sensible heat flux in all of this work, especially since this is the one that is determined in experiments. The resistivities are related to the more commonly used thermal conductivity, λ, and Fick's diffusivity, D. The resistivity r_{qq} is related to the thermal conductivity by:

$$\lambda = \frac{1}{T^2 r_{qq}}, \tag{6.6}$$

while r_{mm} is related to Fick's diffusivity by:

$$D = \frac{1}{Tr_{mm}} \frac{\partial \mu_{b,T}}{\partial c_b}. \tag{6.7}$$

From the results in Chapter 5 it seems reasonable that the thermal conductivity is mostly unaffected by the adsorbed molecules in the system, and not very dependent on the temperature (Ref. 5.5).

The Zeolite External Surfaces

The entropy production of the surface, σ^s, is an excess property, given for stationary state transport of one component and heat as [47]:

$$\sigma^s = J_q'^i \Delta_{i,m} \frac{1}{T} + \left(-\frac{1}{T^m} \Delta_{i,m} \mu_T \left(T^m \right) \right). \tag{6.8}$$

The driving forces are now expressed as differences instead of gradients. For instance, $\Delta_{i,m}$ indicates the difference between the phases m and i. The dimension of σ^s is J K^{-1} m^2. The force-flux relations for the surface are therefore:

$$\Delta_{i,m} \frac{1}{T} = r_{qq}^{s,i} J_q'^i + r_{qm}^{s,i} J, \tag{6.9}$$

$$-\frac{1}{T^m} \Delta_{i,m} \mu_T \left(T^m \right) = r_{mq}^{s,i} J_q'^i + r_{mm}^{s,i} J. \tag{6.10}$$

Again, the superscript indicates that the resistivities are related to the surface, s. We use the superscript i to indicate that these values are related to the i-side of the membrane; see Fig. 6.1. The subscript m again means the membrane.

For the o-side of the interface we obtain similarly,

$$\Delta_{m,o} \frac{1}{T} = r_{qq}^{s,o} J_q'^o + r_{qm}^{s,o} J, \tag{6.11}$$

$$-\frac{1}{T^m} \Delta_{m,o} \mu_T \left(T^m \right) = r_{mq}^{s,o} J_q'^o + r_{mm}^{s,o} J. \tag{6.12}$$

Similarly for these equations, the superscript indicates which surface the value relates to. The values of $J_q'^i$ and $J_q'^o$ are not necessarily identical. The values of

the resistivities for the surface are evaluated from the fluxes in the corresponding gas-phase.

In order to find the temperature and concentration profiles across the membrane, we solve Eqs. (6.2), (6.4), (6.5) and (6.9)–(6.12) simultaneously.

6.2.2 Transport Coefficients and Driving Forces

Because of the Onsager symmetry relation, $r_{ij} = r_{ji}$, only three coefficients are needed in the Eqs. (6.4), (6.5), and six in the set (6.9) to (6.12). The nine coefficients needed were already determined by Inzoli *et al.* [35, 193], and the values of the transport coefficients are shown in Fig. 6.4 (transport inside the membrane) and Fig. 6.5 (transport at the membrane surface). Altogether, the six equations and nine coefficients are sufficient to compute the profiles of the temperature and chemical potential across the heterogeneous system fully, for any set of inlet conditions on the i-side, or feed side.

The chemical potential driving force is everywhere taken at a specified temperature. This driving force in the membrane is

$$-\frac{1}{T}\frac{\mathrm{d}}{\mathrm{d}x}\mu_T = -R\frac{\mathrm{d}}{\mathrm{d}x}\ln a, \tag{6.13}$$

where $a = p/p^*(T)$ is the activity, defined by p, the vapour pressure of the component that would be in equilibrium with the gas in the membrane (assuming ideal gas behaviour), and p^*, the vapour pressure for saturation of the gas at temperature T. The driving force across the surface is likewise

$$-\frac{1}{T^m}\Delta_{m,o}\mu_T\left(T^m\right) = -R\ln\frac{p}{p^*\left(T^m\right)}. \tag{6.14}$$

These equations will be used to calculate jumps in concentration at the surface.

6.3 Case Studies of Heat and Mass Transport Across the Zeolite Membrane

To examine the interaction of heat and mass transport across the zeolite membrane, we have chosen to present the profiles of concentration and temperature for the

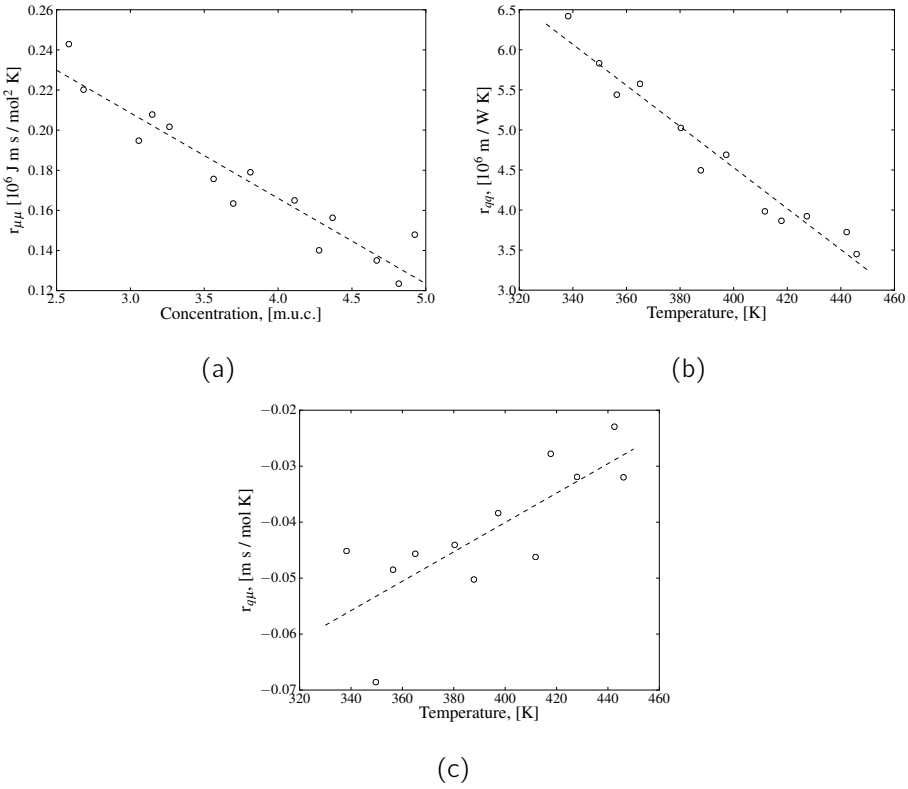

Figure 6.4: The resistance to (*a*) mass transfer, (*b*) heat transfer, and (*c*) the coupling between mass and heat transfer for *n*-butane in silicalite-1 zeolite. The resistance to mass transfer, $r_{\mu\mu}$, is given as a function of the concentration, while the resistance to heat transfer, r_{qq}, is given as a function of temperature. Note that the coupling coefficient, $r_{q\mu}$, is very small.

following conditions. Results are reported in tables or figures as indicated:

- The heat and mass fluxes at constant and equal temperatures in the gas-phases; see Table 6.1 and Fig. 6.6.
- The heat and mass fluxes at isobaric transport of *n*-butane; see Table 6.2 and

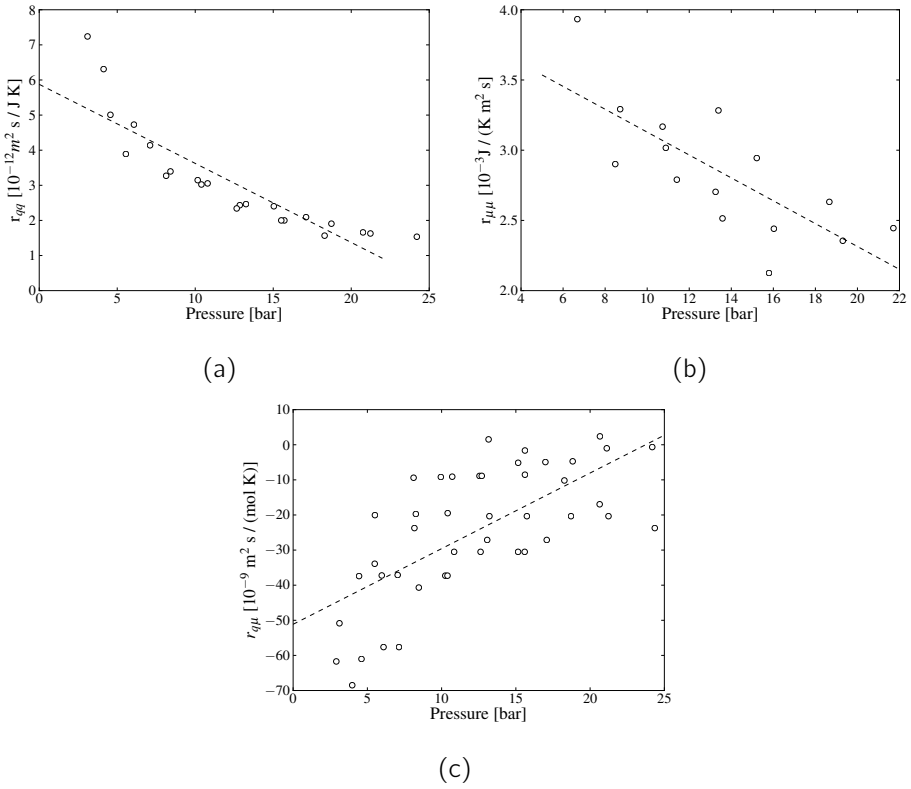

Figure 6.5: The resistance to (*a*) mass transfer, (*b*) heat transfer, and (*c*) the coupling between mass and heat transfer for *n*-butane at the external surface of silicalite-1 zeolite. All values are depending on the pressure in the facing gas-phase, and the temperature dependency is found to be negligible.

Fig. 6.7.

6.3.1 Solution Procedure

There are different ways to treat this type of membrane system. Eqs. (6.4) to (6.12) are formulated such that we can calculate fluxes and temperature profiles on the

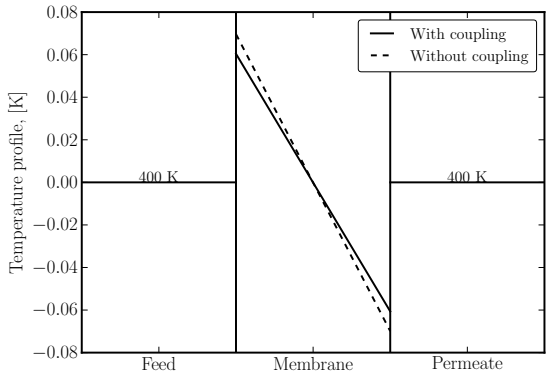

(a)

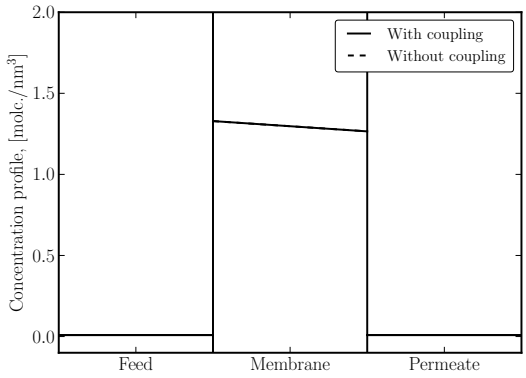

(b)

Figure 6.6: Concentration and temperature profiles in the zeolite membrane. On both sides of the membrane the temperature is 400 K; Fig. 6.6a shows the temperature profile, while Fig. 6.6b shows the concentration profile across the membrane. The fugacity difference between the two gas-phases is 10 kPa. The modelling is performed both with coupling and of heat and mass transfer, and without coupling. For the temperature across the membrane, we observe that including the coupling of heat and mass transfer in the modelling leads to differences in the temperature profile, while the concentration profile is not affected.

Table 6.1: Heat and mass fluxes for various fugacity differences over the membrane. The fugacity on the 'feed' side (denoted by i in the text and in Fig. 6.1) is 50 kPa, and the 'permeate' side (denoted by o) is $f_i - \Delta f$. The temperature is kept at 400 K on both sides, and the thickness of the membrane is 50 μm. The measurable heat flux is given for the i-side of the membrane.

Δf (kPa)	J (mol m^{-2} s)	$J_q'^i$ (kJ m^{-2} s)
2	0.055 08	−2.40
4	0.112 50	−4.89
6	0.172 48	−7.50
8	0.235 24	−10.23
10	0.301 07	−13.10

Table 6.2: Heat and mass fluxes for various fugacity differences over the membrane. In this table we present the mass flux, as well as the measurable heat flux for the 'feed' side (denoted by i) of the membrane. Here, ΔT is $T^o - T^i$, and T^i =400 K. We denote the 'permeate' side by o. In all cases, the fugacity of n-butane is set to be f^i =100 kPa on both sides of membrane, and the membrane is kept at 50 μm thickness. In all cases, we have used coupling of heat and mass transport over both the membrane and the surfaces.

ΔT (K)	J (mol m^{-2} s)	$J_q'^i$ (kJ m^{-2} s)
0.2	−0.001 79	−5.18
0.4	−0.003 58	−10.35
0.6	−0.005 37	−15.51
0.8	−0.007 15	−20.67
1.0	−0.008 94	−25.83

membrane surface. For other formulations, we refer to the work of Kjelstrup and Bedeaux [47]. In this case, we have the resistivities as a function of pressure for the gas-zeolite interface, and the resistivities for transport in the membrane as a function of the local temperature and concentration. The cases of equal temperature difference over the membrane and isobar transport can be solved directly by solving Eqs (6.4), (6.5) and (6.9)–(6.12). In addition the total energy balance of Eq. (6.2) is used. This leads to a system with eight equations, and eight unknowns. The

equations can be solved numerically. In this case, we wish to find the fluxes, J, $J_q'^m$, $J_q'^i$, and $J_q'^o$. In addition, we obtain the temperature, and concentration profiles across the membrane.

The resistivities on the surfaces are determined from the pressure in the adjoining gas-phase. The surface resistivities were relatively independent of the temperature over the range of temperatures from 350 K to 450 K. In Fig. 6.5 we have plotted the values of resistivities obtained from Inzoli *et al.* [35].

The resistivities for the membrane are found from the concentration and temperature on the i-side of the membrane. All values for resistivities inside the membrane are taken from Inzoli *et al.* [193], see Fig. 6.4. These values are obtained for a system with b-oriented silicalite-1, where the straight channels in the silicalite-1 emerge on the gas-zeolite interface. All values in the work of Inzoli are obtained for such a system. Also, that model does not take defects, for example, pinholes or small fractures, into account. For practical applications, the zeolite membrane has to be fixed to some frame or suspended in a polymer matrix. These are effects that will clearly affect the transport, but are not taken into account here.

6.3.2 Results and Discussion

In this section we present results obtained by solving the reported equations. There is a huge number of possible configurations of such a membrane setup; in this case, we have focused on a few basic setups. The choice of temperature is well within the range of temperatures used by Inzoli *et al.* [35, 193].

Equal Temperature in Gas-phases

The temperature difference from gas-phase to gas-phase is first set to zero, setting the temperature equal to 400 K on both sides. This still produces a jump in temperature from the surface to the membrane. We set the membrane thickness to be 50 μm, and the difference in pressure is taken to be from 2 kPa to 10 kPa, in increments of 2 kPa.

In Fig. 6.6 we present the temperature and concentration profile for this case. The temperature profile has a jump across the surfaces on both sides of the membrane. There is also a jump in the chemical potential (not shown). The concentra-

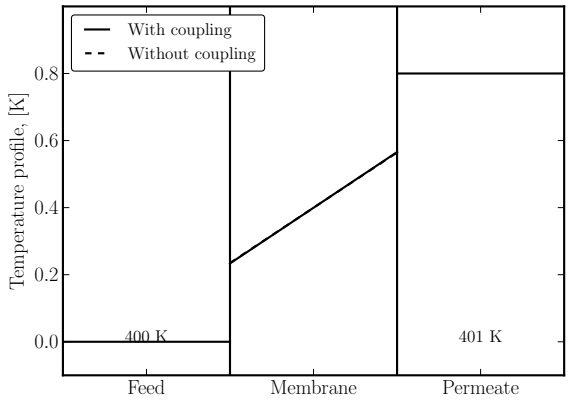

(a)

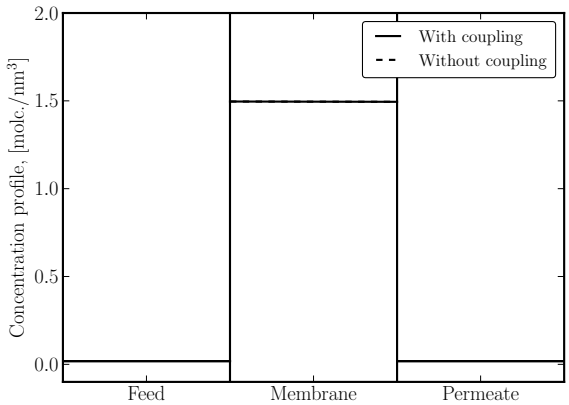

(b)

Figure 6.7: Concentration and temperature profiles at 400 K; Fig. 6.7a shows the temperature difference, while Fig. 6.7b shows the concentration profile across the membrane. The temperature difference between the two gas-phases is kept at 0.8 K. We considered the situation in which coupling between heat and mass transfer was included or excluded in the model. The effect of the coupling is negligible for this case.

tion in the different parts of the system is shown in Fig. 6.6b. The concentration in the gas-phases is low, and the concentration in the zeolite membrane is relatively high.

In Tab. 6.1, we present the transport of heat and mass through the membrane when there is no temperature difference, but there is a difference in pressure of *n*-butane. We clearly see how increasing the gradient in pressure changes the transport of *n*-butane through the membrane. The membrane thickness was 50 μm.

Thermally Induced Transport

In this case, we study the transport over the membrane, by setting the pressure on both sides of the membrane to a constant value, 50 kPa. The temperature is kept at 400 K on the *i*-side of the membrane in all the cases, while the temperature of the *o*-side is given by $T_i + \Delta T$. Concentration and temperature profiles for this case are presented in Fig. 6.7, and the resulting fluxes for different gradients in temperature are given in Tab. 6.2.

The temperature gradient strongly influences the transport of heat in the system. However, we see that also the contribution to mass transport can be significant, especially at higher temperature differences. In this case, we see that heating the *o*-side will decrease the total mass transport in the membrane. Still, the most important contribution to mass transport is found in the pressure difference.

Enhancing Membrane Transport

In Tab. 6.1 we have presented the heat and mass transport over the membrane with a constant pressure difference, and differences in temperature. It is obvious that increasing transport can be obtained by increasing the temperature on the *o*-side of the membrane. The transport of heat with no temperature difference is caused by the coupling of heat transport with the mass transport. This is a quite significant contribution for such a small pressure difference.

Transport in the Membrane

The transport inside the membrane can very well be described using the classical equations, that is, Fick's and Fourier's laws. Coupling of heat and mass is zero in

pure systems, and small in two-component bulk phases such as silicalite-1 with *n*-butane. The coupling is found to have a small effect on the thermal gradient, as can be seen in Fig. 6.6a, while the concentration gradient seems to be more or less unaffected by the coupling. This can easily be seen from the isotherms; see Fig. 6.3, where all of the isotherms show saturation at the pressures and temperatures used in these calculations.

6.4 Conclusions

It has recently become clear that Fourier's and Fick's laws, plus the energy balance [202], are not sufficient when it comes to describing interface transport for zeolite membranes, nor even for transfer of single components [47]. These equations alone are not sufficient to obey the requirement for Onsager symmetry in the interaction of the heat and mass flux. This is confirmed by this work. This requirement can be fulfilled only by invoking the theory of non-equilibrium thermodynamics. Going to this level of description necessarily means that the description becomes more complicated. The gain may be a better basis for further use, for optimization of yield and energy efficiency of membrane reactors.

In this chapter, we have presented results obtained for transport under non-equilibrium conditions, and shown how this method models transport across a zeolite membrane in agreement with the second law of thermodynamics. We clearly see changes in temperature at the surface of the zeolite, and this effect needs further study. In this case we have only presented transport of single components across the zeolite. In future work, the selectivity and separation purposes should be studied further.

References

[1] Deem, M.W.; Pophale, R.; Cheeseman, P.A.; and Earl, D.J. Computational Discovery of New Zeolite-Like Materials. *J. Phys. Chem. C*, 113, 2009: 21353–21360.

[2] Dubbeldam, D.; Krishna, R.; Calero, S.; and Yazaydin, A.O. Computer-Assisted Screening of Ordered Crystalline Nanoporous Adsorbents for Separation of Alkane Isomers. *Angew. Chem. Int. Ed.*, 51, 2012: 11867–11871.

[3] van Erp, T.; Caremans, T.P.; Dubbeldam, D.; Martin-Calvo, A.; Calero, S.; and Martens, J.A. Enantioselective Adsorption in Achiral Zeolites. *Angew. Chem. (Int. Ed.)*, 49, 2010: 3010–3013.

[4] Shu, X.; Wang, X.; Kong, Q.; Gu, X.; and Ninping, X. High-Flux MFI Zeolite Membrane Supported on YSZ Hollow Fiber for Separation of Ethanol/Water. *Ind. Eng. Chem. Res.*, 51, 2012: 12073–12080.

[5] Krishna, R. and van Baten, J.M. Comment on Comparative Molecular Simulation Study of CO_2/N_2 and CH_4/N_2 Separation in Zeolites and Metal-Organic Frameworks. *Langmuir*, 26, 2010: 2975–2978.

[6] Himeno, S.; Tomita, T.; Suzuki, K.; Nakayama, K.; Yajima, K.; and Yoshida, S. Synthesis and Permeation Properties of a DDR-Type Zeolite Membrane for Separation of CO_2/CH_4 Gaseous Mixtures. *Ind. Eng. Chem. Res.*, 46(21), 2007: 6989–6997.

[7] Schenk, M.; Vidal, S.L.; Vlugt, T.J.H.; Smit, B.; and Krishna, R. Separation of Alkane Isomers by Exploiting Entropy Effects During Adsorption on Silicalite-1: a Configurational-bias Monte Carlo Simulation Study. *Langmuir*, 17, 2001: 1558–1570.

[8] Gump, C.J.; Noble, R.D.; and Falconer, J.L. Separation of Hexane Isomers Through Nonzeolite Pores in ZSM-5 Zeolite Membranes. *Ind. Eng. Chem. Res.*, 38, 1999: 2775–2781.

[9] FUNKE, H.H.; ARGO, A.M.; FALCONER, J.L.; and NOBLE, R.D. Separations of Cyclic, Branched, and Linear Hydrocarbon Mixtures Through Silicalite Membranes. *Ind. Eng. Chem. Res.*, 36(1), 1997: 137–143.

[10] JAFAR, J.J. and BUDD, P.M. Separation of Alcohol/Water Mixtures by Pervaporation Through Zeolite a Membranes. *Micropor. Matt.*, 12, 1997: 305–311.

[11] KOEKKOEK, A.J.J.; KIM, W.; DEGIRMENCI, V.; XIN, H.; RYOO, R.; and HENSEN, E.J.M. Catalytic Performance of Sheet-Like Fe/ZSM-5 Zeolites for the Selective Oxidation of Benzene with Nitrous Oxide. *Journal of Catalysis*, 299(0), 2013: 81–89.

[12] VAN DEN BERGH, J.; NISHIYAMA, N.; and KAPTEIJN, F. *Novel Concepts in Catalysis and Chemical Reactors*, chapter Zeolite Membranes in Catalysis; What is New and How Bright is the Future? Wiley, New York, 2010, 211.

[13] DEN OUDEN, C.J.J.; SMIT, B.; WIELERS, A.F.H.; JACKSON, R.A.; and NOWAK, A.K. Computer Simulations in Zeolite Catalysis Research. *Mol. Sim.*, 4, 1989: 121–136.

[14] KÄRGER, J.; RUTHVEN, D.M.; and THEODOROU, D.N. *Diffusion in Nanoporous Materials*. Wiley, New York, 2012.

[15] BAERLOCHER, C.; MCCUSKER, L.B.; and OLSON, D.H. *Atlas of Zeolite Framework Types*. Elsevier, Amsterdam, 2007.

[16] D'ALESSANDRO, D.M.; SMIT, B.; and LONG, J.R. Carbon Dioxide Capture: Prospects for New Materials. *Angew. Chem.*, 49, 2010: 6058–6082.

[17] VAN DEN BERGH, J.; MITTELMEIJER-HAZELEGER, M.; and KAPTEIJN, F. Modelling Permeation of CO_2/CH_4, N_2/CH_4 and CO_2/Air Mixtures Across a DD3R Zeolite Membrane. *J. Phys. Chem. C*, 114, 2010: 9379–9389.

[18] KIM, J.; LIN, L.C.; SWISHER, J.A.; HARANCZYK, M.; and SMIT, B. Predicting Large CO_2 Adsorption in Aluminosilicate Zeolites for Postcombustion Carbon Dioxide Capture. *J. Am. Chem. Soc.*, 134(46), 2012: 18940–18943.

[19] Liu, B. and Smit, B. Molecular Simulation Studies of Separation of CO_2/N_2, CO_2/CH_4, and CH_4/N_2 by ZIFs. *J. Phys. Chem. C*, 114(18), 2010: 8515–8522.

[20] Smit, B. and Maesen, T.L.M. Molecular Simulations of Zeolites: Adsorption, Diffusion, and Shape Selectivity. *Chem. Rev.*, 108(10), 2008: 4125–4184.

[21] Choi, M.; Na, K.; Kim, J.; Sakamoto, Y.; Terasaki, O.; and Ryoo, R. Stable Single-Unit-Cell Nanosheets of Zeolite MFI as Active and Long-Lived Catalysts. *Nature*, 461, 2009: 246–249.

[22] Caro, J. and Noack, M. Zeolite Membranes — Recent Developments and Progress. *Micropor. Mesopor. Mater.*, 115, 2008: 215–233.

[23] J. Cejka, H. van Bekkum, A.C. and Schöth, F., editors. *Introduction to Zeolite Science and Practice*. Elsevier, 2007.

[24] van de Graaf, J.; Kapteijn, F.; and Moulijn, J. Modeling Permeation of Binary Mixtures Through Zeolite Membranes. *AIChE J.*, 45, 1999: 497–511.

[25] Coronas, J. and Santamaria, J. State-of-the-Art in Zeolite Membrane Reactors. *Topics in Catalysis*, 29, 2004: 29–44.

[26] Schenk, M.; Calero, S.; Maesen, T.L.M.; Van Benthem, L.L.; Verbeek, M.G.; and Smit, B. Understanding Zeolite Catalysis: Inverse Shape Selectivity Revised. *Angew. Chem. (Int. Ed.)*, 41, 2002: 2500–2502.

[27] Sanborn, M.J. and Snurr, R.Q. Diffusion of Binary Mixtures of CF_4 and *n*-Alkanes in Faujasite. *Sep. Pur. Tech.*, 20, 2000: 1–13.

[28] Salem, A.; Ghoreyshi, A.A.; and Jahanshahi, M. A Multicomponent Transport Model for Dehydration of Organic Vapors by Zeolite Membranes. *Desalination*, 193, 2006: 35–42.

[29] Kuhn, J.; Stemmer, R.; Kapteijn, F.; Kjelstrup, S.; and Gross, J. A Non-Equilibrium Thermodynamics Approach to Model Mass and Heat Transport for Water Pervaporation Through a Zeolite Membrane. *J. Mem. Sci.*, 330, 2009: 388–398.

[30] KRISHNA, R. and VAN BATEN, J.M. A Molecular Dynamic Investigation of the Diffusion of Methane-Ethane and Methane-Propane Mixtures in Zeolites. *Chem. Eng. Technol.*, 29, 2006: 1429–1437.

[31] KRISHNA, R. and PASCHEK, D. Separation of Hydrocarbon Mixtures Using Zeolite Membranes: a Modelling Approach Combining Molecular Simulations with the Maxwell-Stefan Theory. *Sep. Pur. Tech.*, 21, 2000: 111–136.

[32] KOEKKOEK, A.J.J.; XIN, H.; YANG, Q.; LI, C.; and HENSEN, E.J.M. Hierarchically Structured Fe/ZSM-5 as Catalysts for the Oxidation of Benzene to Phenol. *Micropor. Mesopor. Mater.*, 145(1–3), 2011: 172–181.

[33] ZIMMERMANN, N.E.R.; SMIT, B.; and KEIL, F.J. On the Effects of the External Surface on Equilibrium Transport in Zeolite Crystals. *J. Phys. Chem. C*, 114(1), 2010: 300–310.

[34] ZIMMERMANN, N.E.R.; SMIT, B.; and KEIL, F.J. Predicting Local Transport Coefficients at Solid–Gas Interfaces. *J. Phys. Chem. C*, 116, 2012: 18878–18883.

[35] INZOLI, I.; KJELSTRUP, S.; BEDEAUX, D.; and SIMON, J.M. Transport Coefficients of *n*-Butane Into and Through the Surface of Silicalite-1 From Non-Equilibrium Molecular Dynamics Study. *Micropor. Mesopor. Mater.*, 125, 2009: 112–125.

[36] ZIMMERMANN, N.E.R.; BALAJI, S.P.; and KEIL, F.J. Surface Barriers of Hydrocarbon Transport Triggered by Ideal Zeolite Structures. *J. Phys. Chem. C*, 116, 2012: 3677–3683.

[37] LEE, I. and JEONG, H.K. Synthesis and Gas Permeation Properties of Highly *b*-Oriented MFI Silicalite-1 Thin Membranes with Controlled Microstructure. *Micropor. Mesopor. Mater.*, 141, 2011: 175–183.

[38] INZOLI, I.; SIMON, J.M.; and KJELSTRUP, S. Surface Adsorption Isotherms and Surface Excess Densities of *n*-Butane in Silicalite-1. *Langmuir*, 25, 2009: 1518–1525.

[39] Inzoli, I.; Simon, J.M.; Kjelstrup, S.; and Bedeaux, D. Thermal Effects During Adsorption of *n*-Butane on a Silicalite-1 Membrane: a Non-Equilibrium Molecular Dynamics Study. *J. Colloid Interf. Sci.*, 313, 2007: 563–573.

[40] Røsjorde, A.; Fossmo, D.W.; Bedeaux, D.; Kjelstrup, S.; and Hafskjold, B. Nonequilibrium Molecular Dynamics Simulations of Steady-State Heat and Mass Transport in Condensation I. Local Equilibrium. *J. Colloid Interf. Sci.*, 232, 2000: 178–185.

[41] Røsjorde, A.; Kjelstrup, S.; Bedeaux, D.; and Hafskjold, B. Nonequilibrium Molecular Dynamics Simulations of Steady-State Heat and Mass Transport in Condensation. II. Transfer Coefficients. *J. Colloid Interf. Sci.*, 240, 2001: 355–364.

[42] Simon, J.M.; Kjelstrup, S.; Bedeaux, D.; and Hafskjold, B. Thermal Flux Through a Surface of *n*-Octane. a Non-Equilibrium Molecular Dynamics Study. *J. Phys. Chem. B*, 108, 2004: 7186–7195.

[43] Inzoli, I.; Kjelstrup, S.; Bedeaux, D.; and Simon, J.M. Thermodynamic Properties of a Liquid-Vapor Interface in a Two-Component System. *Chem. Eng. Sci.*, 65, 2010: 4105–4116.

[44] Inzoli, I.; Kjelstrup, S.; Bedeaux, D.; and Simon, J.M. Transfer Coefficients for the Liquid-Vapor Interface of a Two-Component Mixture. *Chem. Eng. Sci.*, 66, 2011: 4533–4548.

[45] Lervik, A.; Bresme, F.; Kjelstrup, S.; Bedeaux, D.; and Rubi, J.M. Heat Transfer in Protein-Water Interfaces. *Phys. Chem. Chem. Phys.*, 12, 2010: 1610–1618.

[46] Gibbs, J.W. *Scientific Papers: Thermodynamics*. Dover Publications, Inc, 1961.

[47] Kjelstrup, S. and Bedeaux, D. *Non-Equilibrium Thermodynamics of Heterogeneous Systems*. World Scientific, 2008.

[48] Savin, T.; Glavatskiy, K.S.; Kjelstrup, S.; Öttinger, H.C.; and Bedeaux, D. Local Equilibrium of the Gibbs Interface in Two-Phase Systems. *EPL (Europhysics Letters)*, 97(4), 2012: 40002.

[49] NA, K.; CHOI, M.; PARK, W.; SAKAMOTO, Y.; TERASAKI, O.; and RYOO, R. Pillared MFI Zeolite Nanosheets of a Single-Unit-Cell Thickness. *J. Am. Chem. Soc.*, 132, 2010: 4169–4177.

[50] DE GROOT, S.R. and MAZUR, P. *Non-Equilibrium Thermodynamics*. Dover Publications, Inc, New York, 1984.

[51] LIU, X.; MARTIN-CALVO, A.; MCGARRITY, E.S.; SCHNELL, S.K.; CALERO, S.; SIMON, J.M.; BEDEAUX, D.; KJELSTRUP, S.; BARDOW, A.; and VLUGT, T.J.H. Fick Diffusion Coefficients in Ternary Liquid Systems From Equilibrium Molecular Dynamics Simulations. *Ind. Eng. Chem. Res.*, 51, 2012: 10247–10258.

[52] KRISHNA, R. Problems and Pitfalls in the Use of the Fick Formulation for Intra-Particle Diffusion. *Chem. Eng. Sci.*, 48, 1993: 845–861.

[53] POLYAKOV, P.; MÜLLER-PLATHE, F.; and WIEGAND, S. Reverse Nonequilibrium Molecular Dynamics Calculation of the Soret Coefficient in Liquid Heptane/Benzene Mixtures. *J. Phys. Chem. B*, 112, 2008: 14999–15004.

[54] GLAVATSKIY, K.; PHAROAH, J.G.; and KJELSTRUP, S. Thermal Phenomena Associated with Water Transport Across a Fuel Cell Membrane: Soret and Dufour Effects. *J. Mem. Sci.*, 431, 2013: 96–104.

[55] NIETO-DRAGHI, C.; ÁVALOS, J.B.; and ROUSSEAU, B. Computing the Soret Coefficient in Aqueous Mixtures Using Boundary Driven Nonequilibrium Molecular Dynamics. *J. Chem. Phys.*, 122(11), 2005: 114503.

[56] ONSAGER, L. Reciprocal Relations in Irreversible Processes. I. *Phys. Rev.*, 37, 1931: 405–426.

[57] ONSAGER, L. Reciprocal Relations in Irreversible Processes. II. *Phys. Rev.*, 38, 1931: 2265–2279.

[58] XU, J.; KJELSTRUP, S.; BEDEAUX, D.; RØSJORDE, A.; and REKVIG, L. Verification of Onsager's Reciprocal Relations for Evaporation and Condensation Using Non-Equilibrium Molecular Dynamics. *J. Colloid Interf. Sci.*, 299, 2006: 452–463.

[59] Ikeshoji, T. and Hafskjold, B. Non-Equilibrium Molecular Dynamics Calculation of Heat Conduction in Liquid and Through Liquid-Gas Interface. *Mol. Phys.*, 81(2), 1994: 251–261.

[60] Hafskjold, B. and Ratkje, S.K. Criteria for Local Equilibrium in a System with Transport of Heat and Mass. *J. Stat. Phys.*, 78(1/2), 1995: 463–497.

[61] Simon, J.M.; Inzoli, I.; Bedeaux, D.; and Kjelstrup, S. Numerical Evidence for a Thermal Driving Force During Adsorption of Butane in Silicalite. *Mol. Sim.*, 33(9), 2007: 839–841.

[62] Frenkel, D. and Smit, B. *Understanding Molecular Simulations*. Academic press, 2002.

[63] Ermoshin, V.A.; Smirnov, K.S.; and Bougeard, D. *Ab Initio* Generalized Valence Force Field for Zeolite Modelling. 1. Siliceous Zeolites. *Chem. Phys.*, 202, 1996: 53–61.

[64] Calero, S.; Dubbeldam, D.; Krishna, R.; Smit, B.; Vlugt, T.J.H.; Denayer, J.F.M.; Martens, J.A.; and Maesen, T.L.M. Understanding the Role of Sodium During Adsorption: a Force Field For Alkanes in Sodium-Exchanged Faujasites. *J. Am. Chem. Soc.*, 126, 2004: 11377–11386.

[65] Dubbeldam, D.; Calero, S.; Vlugt, T.J.H.; Krishna, R.; Maesen, T.L.M.; Beerdsen, E.; and Smit, B. Force Field Parameterization Through Fitting on Inflection Points in Isotherms. *Phys. Rev. Lett.*, 93, 2004: 088302.

[66] Dubbeldam, D.; Calero, S.; Vlugt, T.J.H.; Krishna, R.; Maesen, T.L.M.; and Smit, B. United Atom Force Field for Alkanes in Nanoporous Materials. *J. Phys. Chem. B*, 108(33), 2004: 12301–12313.

[67] van Westen, T.; Vlugt, T.J.H.; and Gross, J. Determining Force Field Parameters Using a Physically Based Equation of State. *J. Phys. Chem. B*, 115, 2011: 7872–7880.

[68] Weerasinghe, S. and Smith, P.E. Kirkwood-Buff Derived Force Field for Mixtures of Acetone and Water. *J. Chem. Phys.*, 118(23), 2003: 10663–10670.

[69] WEERASINGHE, S. and SMITH, P.E. A Kirkwood-Buff Derived Force Field for Sodium Chloride in Water. *J. Phys. Chem.*, 119, 2003: 11342–11349.

[70] TUCKERMAN, M.E. *Statistical Mechanics: Theory and Molecular Simulation*. Oxford University Press, 2010.

[71] SCHNELL, S.K.; VLUGT, T.J.H.; SIMON, J.M.; BEDEAUX, D.; and KJELSTRUP, S. Thermodynamics of a Small System in a μT Reservoir. *Chem. Phys. Lett.*, 504, 2011: 199–201.

[72] SCHNELL, S.K.; LIU, X.; SIMON, J.M.; BARDOW, A.; BEDEAUX, D.; VLUGT, T.J.H.; and KJELSTRUP, S. Calculating Thermodynamic Properties From Fluctuations at Small Scales. *J. Phys. Chem. B*, 115, 2011: 10911–10918.

[73] SCHNELL, S.K.; VLUGT, T.J.H.; SIMON, J.M.; BEDEAUX, D.; and KJELSTRUP, S. Thermodynamics of Small Systems Embedded in a Reservoir: a Detailed Analysis of Finite Size Effects. *Mol. Phys.*, 110, 2012: 1069–1079.

[74] SCHNELL, S.K. and VLUGT, T.J.H. Thermal Conductivity in Zeolites Studied by Non-Equilibrium Molecular Dynamics Simulations. *Int. J. Thermophys.*, 34, 2013: 1197–1213.

[75] LIU, X.; SCHNELL, S.K.; SIMON, J.M.; BEDEAUX, D.; KJELSTRUP, S.; BARDOW, A.; and VLUGT, T.J.H. Fick Diffusion Coefficients of Liquid Mixtures Directly Obtained From Equilibrium Molecular Dynamics. *J. Phys. Chem. B*, 115, 2011: 12921–12929.

[76] FRENKEL, D. Simulations: The Dark Side. *Eur. Phys. J. Plus*, 128, 2013: 10.

[77] ALLEN, M. and TILDESLEY, D. *Computer Simulation of Liquids*. Clarendon Press, Oxford, 1987.

[78] VLUGT, T.J.H.; VAN DER EERDEN, J.P.J.M.; DIJKSTRA, M.; SMIT, B.; and FRENKEL, D. *Introduction to Molecular Simulation and Statistical Thermodynamics*. Available from: http://homepage.tudelft.nl/v9k6y/imsst/index.html, 2009.

[79] McQuarrie, D.A. *Statistical Mechanics*. University Science Books, Sausalito, California, 2000.

[80] Metropolis, N.; Rosenbluth, A.W.; Rosenbluth, M.N.; Teller, A.N.; and Teller, E. Equation of State Calculations by Fast Computing Machines. *J. Chem. Phys.*, 21, 1953: 1087–1092.

[81] Moore, G. Cramming More Components Onto Integrated Circuits. *Electronics Magazine*, 38, 1965: 4–8.

[82] Kirkwood, J.G. and Buff, F.P. The Statistical Mechnical Theory of Solutions. I. *J. Chem. Phys.*, 19(6), 1951: 774–778.

[83] Ruckenstein, E. and Shulgin, I. Entrainer Effect in Supercritical Mixtures. *Fluid Phase Equilibria*, 180, 2001: 345–359.

[84] Wedberg, R.; O'Connell, J.P.; Peters, G.H.; and Abildskov, J. Accurate Kirkwood-Buff Integrals From Molecular Simulations. *Mol. Sim.*, 36, 2010: 1243–1252.

[85] Wedberg, R.; O'Connell, J.P.; Peters, G.H.; and Abildskov, J. Total and Direct Correlation Function Integrals From Molecular Simulation of Binary Systems. *Fluid Phase Equilibria*, 302, 2011: 32–42.

[86] Maginn, E.J. Molecular Simulations of Ionic Liquids: Current Status and Future Opportunities. *J. Phys. Condens. Matter*, 21, 2009: 373101–373118.

[87] Krüger, P.; Schnell, S.K.; Bedeaux, D.; Kjelstrup, S.; Vlugt, T.J.H.; and Simon, J.M. Kirkwood-Buff Integrals for Finite Volumes. *J. Phys. Chem. Lett.*, 4, 2013: 235–238.

[88] Hill, T.L. *Thermodynamics of Small Systems, Part 1 and 2*. Benjamin, New York, 1963.

[89] Binder, K. Critical Properties From Monte Carlo Coarse Graining and Renormalization. *Phys. Rev. Lett.*, 47, 1981: 693–696.

[90] VLUGT, T.J.H.; GARCÍA-PÉREZ, E.; DUBBELDAM, D.; BAN, S.; and CALERO, S. Computing the Heat of Adsorption Using Molecular Simulations: the Effect of Strong Coulombic Interactions. *J. Chem. Theory Comput.*, 4(7), 2008: 1107–1118.

[91] KRISHNA, R. and WESSELINGH, J. The Maxwell-Stefan Approach to Mass Transfer. *Chem. Eng. Sci.*, 52(6), 1997: 861–911.

[92] KRISHNA, R. Describing the Diffusion of Guest Molecules Inside Porous Structures. *J. Phys. Chem. C*, 113, 2009: 19756–19781.

[93] FLOQUET, N.; SIMON, J.M.; COULOMB, J.P.; BELLAT, J.P.; WEBER, G.; and ANDRE, G. Heptane Adsorption in Silicalite-1: Molecular Dynamics Simulation. *Micropor. Mesopor. Mater.*, 122, 2009: 61–71.

[94] KARAVIAS, F. and MYERS, A.L. Isosteric Heat of Multicomponent Adsorption: Thermodynamics and Computer Simulations. *Langmuir*, 7, 1991: 3118–3126.

[95] SCHNELL, S.K.; ENGLEBIENNE, P.; SIMON, J.M.; KRÜGER, P.; BALAJI, S.P.; KJELSTRUP, S.; BEDEAUX, D.; BARDOW, A.; and VLUGT, T.J.H. How to Apply the Kirkwood-Buff Theory to Individual Species in Salt Solutions. *Chem. Phys. Lett.*, 582, 2013: 154–157.

[96] LIU, X.; SCHNELL, S.K.; KRÜGER, P.; SIMON, J.M.; VLUGT, T.J.H.; BEDEAUX, D.; and KJELSTRUP, S. Diffusion Coefficients From Molecular Dynamics Simulations in Binary and Ternary Mixtures. *Int. J. Thermophys.*, 34, 2013: 1169–1196.

[97] GANGULY, P. and VAN DER VEGT, N.F.A. Convergence of Sampling Kirkwood-Buff Integrals of Aqueous Solutions with Molecular Dynamics Simulations. *J. Chem. Theory Comput.*, 9, 2013: 1347–1355.

[98] LIU, X.; BARDOW, A.; and VLUGT, T.J.H. Multicomponent Maxwell-Stefan Diffusivities at Infinite Dilution. *Ind. Eng. Chem. Res.*, 50, 2011: 4776–4782.

[99] CHRISTENSEN, S.; PETERS, G.H.; HANSEN, F.Y.; O'CONNELL, J.P.; and ABILDSKOV, J. State Conditions Transferability of Vapor—Liquid Equilibria via Fluc-

tuation Solution Theory with Correlation Function Integrals From Molecular Dynamics Simulation. *Fluid Phase Equilibria*, 260, 2007: 169–176.

[100] Christensen, S.; Peters, G.H.; Hansen, F.Y.; O'Connell, J.P.; and Abildskov, J. Generation of Thermodynamic Data For Organic Liquid Mixtures From Molecular Simulations. *Mol. Sim.*, 33(4), 2007: 449–457.

[101] Nichols, J.W.; Moore, S.G.; and Wheeler, D.R. Improved Implementation of Kirkwood-Buff Solution Theory in Periodic Molecular Simulations. *Phys. Rev. E*, 80, 2009: 051203.

[102] Weeks, J.D.; Chandler, D.; and Andersen, H.C. Role of Repulsive Forces in Determining the Equilibrium Structure of Simple Liquids. *J. Chem. Phys.*, 54, 1971: 5237–5247.

[103] García-Pérez, E.; Parra, J.B.; Ania, C.O.; Dubbeldam, D.; Vlugt, T. J. H. Castillo, J.M.; Merkling, P.J.; and Calero, S. Unraveling the Argon Adsorption Processes in MFI-Type Zeolite. *J. Phys. Chem. C*, 112(27), 2008: 9976–9979.

[104] http://fluidproperties.org/third-challenge-overview.

[105] Simon, J.M. and Rubi, J.M. Temperature at Small Scales: a Lower Limit for a Thermodynamic Description. *J. Phys. Chem. B*, 115, 2011: 1422–1428.

[106] Vlugt, T.J.H.; Krishna, R.; and Smit, B. Molecular Simulations of Adsorption Isotherms for Linear and Branched Alkanes and Their Mixtures in Silicalite. *J. Phys. Chem. B*, 103, 1999: 1102–1118.

[107] van Baten, J.M. and Krishna, R. Entropy Effects in Adsorption and Diffusion of Alkane Isomers in Mordenite: an Intvestigation Using CBMC and MD Simulations. *Micropor. Mesopor. Mater.*, 84, 2005: 179–191.

[108] Krishna, R. and Paschek, D. Molecular Simulations of Adsorption and Siting of Light Alkanes in Silicalite-1. *Phys. Chem. Chem. Phys.*, 3, 2001: 453–462.

[109] SIMON, J.M.; FARDET-LEMAIRE, E.; BEZVERKHYY, I.; BELLAT, J.P.; and BARAS, F. Kinetics of Adsorption of Linear and Branched C6 Alkanes Onto ZSM-5 Zeolite — Experiments and Molecular Simulations. *Diffusion Fundamentals*, 2, 2005: 37.1–37.2.

[110] CHANDROSS, M.; WEBB III, E.B.; GREST, G.S.; MARTIN, M.G.; THOMPSON, A.P.; and ROTH, M.W. Dynamics of Exchange at Gas-Zeolite Interfaces. 1. Pure Component *n*-Butane and *i*-Butane. *J. Phys. Chem. B*, 105, 2001: 5700–5712.

[111] KORTUNOV, P.; VASENKOV, S.; CHMELIK, C.; KÄRGER, J.; RUTHVEN, D.; and WLOCK, J. Influence of Defects on the External Crystal Surface on Molecular Uptake Into MFI-Type Zeolites. *Chem. Mater.*, 16(18), 2004: 3552–3558.

[112] MYERS, A.L. and PRAUSNITZ, J.M. Thermodynamics of Mixed Gas Adsorption. *AIChE J.*, 11, 1965: 121–130.

[113] BEERDSEN, E.; SMIT, B.; and CALERO, S. The Influence of Non-Framework Sodium Cations on the Adsorption of Alkanes in MFI- and MOR-Type Zeolites. *J. Phys. Chem. B*, 106, 2002: 10659–10667.

[114] MARTIN, M.G. and SIEPMANN, J.I. Predicting Multicomponent Phase Equilibria and Free Energies of Transfer for Alkanes by Molecular Simulation. *J. Am. Chem. Soc.*, 119, 1997: 8921–8924.

[115] BEZUS, A.G.; KISELEV, A.V.; LOPATKIN, A.A.; and DU, P.Q. Molecular Statistical Calculation of the Thermodynamic Adsorption Characteristics of Zeolites Using the Atom-Atom Approximation. *J. Chem. Soc., Faraday Trans. II*, 74, 1978: 367–379.

[116] KISELEV, A.V.; LOPATKIN, A.A.; and SHULGA, A.A. Molecular Statistical Calculation of Gas Adsorption by Silicalite. *Zeolites*, 5, 1985: 261–267.

[117] VAN KONINGSVELD, H.; VAN BEKKUM, H.; and JANSEN, J.C. On the Location and Disorder of the Tetrapropylammonium (TPA) Ion in Zeolite ZSM-5 with Improved Framework Accuracy. *Acta. Cryst.*, B43, 1987: 127–132.

[118] Vlugt, T.J.H. and Schenk, M. Influence of Framework Flexibility on the Adsorption Properties of Hydrocarbons in the Zeolite Silicalite. *J. Phys. Chem. B*, 106, 2002: 12757–12763.

[119] Myers, A.L. Thermodynamics of Adsorption in Porous Materials. *AIChE J.*, 48(1), 2002: 145–158.

[120] Myers, A.L. and Monson, P.A. Adsorption in Porous Materials at High Pressure: Theory and Experiment. *Langmuir*, 18(26), 2002: 10261–10273.

[121] Krishna, R.; Calero, S.; and Smit, B. Investigation of Entropy Effect During Sorption of Mixtures of Alkanes in MFI Zeolite. *Chem. Eng. J.*, 88, 2002: 81–94.

[122] Du, Z.; Vlugt, T.J.H.; Smit, B.; and Manos, G. Molecular Simulation of Adsorption of Short Linear Alkanes and Their Mixtures in Silicalite. *AIChE J.*, 44, 1998: 1756–1764.

[123] Krishna, R.; Smit, B.; and Calero, S. Entropy Effects During Sorption of Alkanes in Zeolites. *Chem. Soc. Rev.*, 31, 2002: 185–194.

[124] Faungnawakij, K.; Tanaka, Y.; Shimoda, N.; Fukunaga, T.; Kawashima, S.; Kikuchi, R.; and Eguchi, K. Influence of Solid-Acid Catalysts on Steam Reforming and Hydrolysis of Dimethyl Ether for Hydrogen Production. *Applied Catalysis A: General*, 304(0), 2006: 40–48.

[125] de Jong, K.P.; Mesters, C.M.A.M.; Peferoen, D.G.R.; Brugge, P.T.M.; and de Groot, C. Paraffin Alkylation Using Zeolite Catalysts in a Slurry Reactor: Chemical Engineering Principles to Extend Catalyst Lifetime. *Chem. Eng. Sci.*, 51, 1996: 2053–2060.

[126] Limtrakul, J. and Tantanak, D. Cationic, Structural, and Compositional Effects on the Surface Structure of Zeolitic Aluminosilicate Catalysts. *Chem. Phys.*, 208, 1996: 331–340.

[127] Skorpa, R.; Bordiga, S.; Bleken, F.; Olsbye, U.; Arstad, B.; Tolchard, J.; Mathisen, K.; Svelle, S.; and Bjørgen, M. Assessing the Surface Sites of

the Large Pore 3-Dimensional Microporous Material H-ITQ-7 Using FT-IR Spectroscopy and Molecular Probes. *Micropor. Mesopor. Mater.*, 141, 2011: 146–156.

[128] GÓRA-MAREK, K. and J., D. IR Studies of OH Groups in Mesoporous Aluminosilicates. *Applied Catalysis A: General*, 302(1), 2006: 104–109.

[129] BUSCA, G.; RAMIS, G.; and LORENZELLI, V. FT-IR Study of the Surface Properties of Polycrystalline Vanadia. *Journal of Molecular Catalysis*, 50(2), 1989: 231–240.

[130] MARTUCCI, A.; CRUCIANI, G.; ALBERTI, A.; RITTER, A.; CIAMBELLI, P.; and RAPACCIUOLO, M. Location of Brønsted Sites in D-Mordenites by Neutron Powder Diffraction. *Micropor. Mesopor. Mater.*, 35–36(0), 2000: 405–412.

[131] ABOUELNASR, M.K.F. and SMIT, B. Diffusion in Confinement: Kinetic Simulations of Self- and Collective Diffusion Behavior of Adsorbed Gases. *Phys. Chem. Chem. Phys.*, 14, 2012: 11600.

[132] KRISHNA, R. and VAN BATEN, J.M. Insights Into Diffusion of Gases in Zeolites Gained From Molecular Dynamics Simulations. *Micropor. Mesopor. Mater.*, 109, 2008: 90–108.

[133] KRISHNA, R.; VAN BATEN, J.M.; GARCÍA-PÉREZ, E.; and CALERO, S. Diffusion of CH_4 and CO_2 in MFI, CHA and DDR Zeolites. *Chem. Phys. Lett.*, 429, 2006: 219–224.

[134] VAN DEN BERGH, J.; BAN, S.; VLUGT, T.J.H.; and KAPTEIJN, F. Modeling the Loading Dependency of Diffusion in Zeolites: the Relevant Site Model Extended to Mixtures in DDR-Type Zeolite. *J. Phys. Chem. C*, 113, 2009: 21856–21865.

[135] MAESEN, T.L.M.; KRISHNA, R.; VAN BATEN, J.M.; SMIT, B.; CALERO, S.; and SANCHEZ, J.M.C. Shape-Selective *n*-Alkane Hydroconversion at Exterior Zeolite Surfaces. *Journal of Catalysis*, 256, 2008: 95–107.

[136] WEITKAMP, J. Zeolites and Catalysis. *Solid State Ionics*, 131, 2000: 175–188.

[137] Vejka, J.; Centi, G.; Perez-Pariente, J.; and Roth, W.J. Zeolite-Based Materials For Novel Catalytic Applications: Opportunities, Perspectives and Open Problems. *Catal. Today*, 179(1), 2012: 2–15.

[138] Caro, J.; Noack, M.; and Kölsch, P. Zeolite Membranes: From the Laboratory Scale to Technical Applications. *Adsorption*, 11, 2005: 215–227.

[139] Perez-Ramirez, J.; Christensen, C.H.; Egeblad, K.; Christensen, C.H.; and Groen, J.C. Hierarchical Zeolites: Enhanced Utilisation of Microporous Crystals in Catalysis by Advances in Materials Design. *Chem. Soc. Rev.*, 37, 2008: 2530–2542.

[140] van Donk, S.; Janssen, A.H.; Bitter, J.H.; and de Jong, K. Generation, Characterization, and Impact of Mesopores in Zeolite Catalysts. *Catalysis Reviews-Science and Engineering*, 45, 2003: 297–319.

[141] Ban, S.; van Laak, A.N.C.; Landers, J.; Neimark, A.; de Jongh, P.E.; de Jong, K.P.; and Vlugt, T.J.H. Insight Into the Effect of Dealumination on Mordenite Using Experimentally Validated Simulations. *J. Phys. Chem. C*, 114, 2010: 2056–2065.

[142] Tao, Y.; Kanoh, H.; and Kaneko, K. ZSM-5 Monolith of Uniform Mesoporous Channels. *J. Am. Chem. Soc.*, 125, 2003: 6044–6045.

[143] Tao, Y.; Kanoh, H.; Abrams, L.; and Kaneko, K. Mesopore-Modified Zeolites: Preparation, Characterization, and Applications. *Chem. Rev.*, 106, 2006: 896–910.

[144] Egeblad, K.; Christensen, C.H.; Kustova, M.; and Christensen, C.H. Templating Mesoporous Zeolites. *Chem. Mater.*, 20, 2008: 946–960.

[145] Na, K.; Choi, M.; and Ryoo, R. Recent Advances in the Synthesis of Hierarchically Nanoporous Zeolites. *Micropor. Mesopor. Mater.*, 166, 2013: 3–19.

[146] García-Pérez, E.; Schnell, S.K.; Castillo, J.M.; Calero, S.; Kjelstrup, S.; Dubbeldam, D.; and Vlugt, T.J.H. External Surface Adsorption on Silicalite-1 Zeolite Studied by Molecular Simulation. *J. Phys. Chem. C*, 115, 2011: 15355–15360.

[147] LEW, C.M.; CAI, R.; and YAN, Y. Zeolite Thin Films: From Computer Chips to Space Stations. *Acc. Chem. Res.*, 43, 2010: 210–219.

[148] KÄRGER, J. Random Walk Through Two-Channel Networks: a Simple Means to Correlate the Coefficients of Anisotropic Diffusion in ZSM-5 Type Zeolites. *J. Phys. Chem.*, 95, 1991: 5558–5560.

[149] VAN DEN BERGH, J.; BAN, S.; VLUGT, T.J.H.; and KAPTEIJN, F. Modeling the Loading Dependency of Diffusion in Zeolites: the Relevant Site Model. *J. Phys. Chem. C*, 113, 2009: 17840–17850.

[150] SCHNELL, S.K.; VLUGT, T.J.H.; and KJELSTRUP, S. *Handbook on Membrane Reactors*, volume 1, chapter Non-Equilibrium Thermodynamics for the Description of Transport of Heat and Mass Across a Zeolite Membrane. Woodhead, 2013, 627–646.

[151] ARYA, G.; MAGINN, E.J.; and CHANG, H.C. Effect of the Surface Energy Barrier on Sorbate Diffusion in $AlPO_4$-5. *J. Phys. Chem. B*, 105, 2001: 2725–2735.

[152] ZIMMERMANN, N.E.R.; ZABET, T.J.; and KEIL, F.J. Transport Into Nanosheets: Diffusion Equations Put to Test. *J. Phys. Chem. C*, 117, 2013: 7384–7390.

[153] GUMMA, S. and TALU, O. Net Adsorption: a Thermodynamic Framework for Supercritical Gas Adsorption and Storage in Porous Solids. *Langmuir*, 26, 2010: 17013–17023.

[154] DÜREN, T.; SARKISOV, L.; YAGHI, O.; and SNURR, R. Design of New Materials for Methane Storage. *Langmuir*, 20(7), 2004: 2683–2689.

[155] STEWART, R.B. and JACOBSEN, R.T. Thermodynamic Properties of Argon From the Triple Point to 1200 K with Pressures to 1000MPa. *J. Phys. Chem. Ref. Data*, 18(2), 1989: 639–798.

[156] HENSEN, E.J.M. Personal Communication.

[157] Saito, A. and Foley, H.C. High-Resolution Nitrogen and Argon Adsorption on ZSM-5 Zeolites: Effects of Cation Exchange and Si/Al Ratio. *Micropor. Matt.*, 3, 1995: 543–556.

[158] McLeary, E.E.; Jansen, J.C.; and Kapteijn, F. Zeolite Based Films, Membranes and Membrane Reactors: Progress and Prospects. *Micropor. Mesopor. Mater.*, 90, 2006: 198–220.

[159] Naber, J.E.; de Jong, K.P.; Stork, W.H.J.; Kuipers, H.P.C.E.; and Post, M.F.M. Industrial Applications of Zeolite Catalysis. *Stud. Surf. Sci. Cat.*, 84, 1994: 2197–2219.

[160] Baker, R.W. and Lokhandwala, K. Natural Gas Processing with Membranes: an Overview. *Ind. Eng. Chem. Res.*, 47, 2008: 2109–2121.

[161] Hunt, H.K.; Lew, C.M.; Sun, M.; Yan, Y.; and Davis, M.E. Pure-Silica LTA, CHA, STT, ITW, and -SVR Thin Films and Powders for Low-*k* Applications. *Micropor. Mesopor. Mater.*, 130, 2010: 49–55.

[162] Hunt, H.K.; Lew, C.M.; Sun, M.; Yan, Y.; and Davis, M.E. Pure-Silica Zeolite Thin Films by Vapor Phase Transport of Fluoride for Low-*k* Applications. *Micropor. Mesopor. Mater.*, 128, 2010: 12–18.

[163] van den Bergh, J.; Ban, S.; Vlugt, T.J.H.; and Kapteijn, F. Diffusion in Zeolites: Extension of the Relevant Site Model to Light Gases and Mixtures Thereof in Zeolites DDR, CHA, MFI and FAU. *Sep. Pur. Tech.*, 73, 2010: 151–163.

[164] Vlugt, T.J.H.; Dellago, C.; and Smit, B. Diffusion of Isobutane in Silicalite Studied by Transition Path Sampling. *J. Chem. Phys.*, 113, 2000: 8791–8799.

[165] Vlugt, T.J.H.; Van den Bergh, J.; Dubbeldam, D.; and Kapteijn, F. Reconciling the Relevant Site Model and Dynamically Corrected Transition State Theory. *Chem. Phys. Lett.*, 495, 2010: 77–79.

[166] Krishna, R. and van den Broeke, L.J.P. The Maxwell-Stefan Description of Mass Transport Across Zeolite Membranes. *The Chemical Engineering Journal*, 57, 1995: 155–162.

[167] KRISHNA, R.; SMIT, B.; and VLUGT, T.J.H. Sorption-Induced Diffusion-Selective Separation of Hydrocarbon Isomers Using Silicalite. *J. Phys. Chem. A*, 102, 1998: 7727–7730.

[168] KRISHNA, R. Diffusion of Binary Mixtures in Zeolites: Molecular Dynamics Simulations Versus Maxwell-Stefan Theory. *Chem. Phys. Lett.*, 326, 2000: 477–484.

[169] KAPTEIJN, F.; MOULIJN, J.A.; and KRISHNA, R. The Generalized Maxwell-Stefan Model for Diffusion in Zeolites: Sorbate Molecules with Different Saturation Loadings. *Chem. Eng. Sci.*, 55, 2000: 2923–2930.

[170] CAHILL, D.G. Thermal Conductivity Measurement From 30 to 750 K: the 3Ω Method. *Rev. Sci. Instrum.*, 61, 1990: 802–808.

[171] COQUIL, T.; LEW, C.M.; YAN, Y.; and PILON, L. Thermal Conductivity of Pure Silica MEL and MFI Zeolite Thin Films. *J. Appl. Phys.*, 108(4), 2010: 044902.

[172] FANG, J.; HUANG, Y.; LEW, C.M.; YAN, Y.; and PILON, L. Temperature Dependent Thermal Conductivity of Pure Silica MEL and MFI Zeolite Thin Films. *J. Appl. Phys.*, 111, 2012: 054910.

[173] MURASHOV, V.V. and WHITE, M.A. Thermal Properties of Zeolites: Effective Thermal Conductivity of Dehydrated Powdered Zeolite 4A. *Materials Chemistry and Physics*, 75, 2002: 178–180.

[174] MURASHOV, V.V. and WHITE, M.A. Apparatus for Dynamical Thermal Measurements of Low-Thermal Diffusivity Particulate Materials at Subambient Temperatures. *Rev. Sci. Instrum.*, 69, 1998: 4198–4204.

[175] JAKUBINEK, M.B.; ZHAN, B.Z.; and WHITE, M.A. Temperature-Dependent Thermal Conductivity of Powdered Zeolite NaX. *Micropor. Mesopor. Mater.*, 103, 2007: 108–112.

[176] LIU, Z.Y.; RESTUCCIA, G.; and GIORDANO, N. Fast Simple and Accurate Measurement of Zeolite Thermal Conductivity. *Zeolites*, 10, 1990: 565–570.

[177] Callaway, J. Model For Lattice Thermal Conductivity at Low Temperatures. *Phys. Rev.*, 113, 1959: 1046–1051.

[178] Holland, M.G. Analysis of Lattice Thermal Conductivity. *Phys. Rev.*, 132, 1963: 2461–2471.

[179] McGaughey, A.J.H. and Kaviany, M. Phonon Transport in Molecular Dynamics Simulations: Formulation and Thermal Conductivity Prediction. In A.B.C. George A. Greene James P. Hartnett and Y.I. Cho, editors, *Advances in Heat Transfer*, volume 39 of *Advances in Heat Transfer*. Elsevier, 2006, 169–255.

[180] Greenstein, A.; Hudiono, Y.; Graham, S.; and Nair, S. Effects of Nonframework Metal Cations and Phonon Scattering Mechanisms on the Thermal Transport Properties of Polycrystalline Zeolite LTA Films. *J. Appl. Phys.*, 107(6), 2010: 063518.

[181] Hudiono, Y.; Greenstein, A.; Saha-Kuete, C.; Olson, B.; Graham, S.; and Nair, S. Effects of Composition and Phonon Scattering Mechanisms on Thermal Transport in MFI Zeolite Films. *J. Appl. Phys.*, 102(5), 2007: 053523.

[182] Greenstein, A.M.; Graham, S.; Hudiono, Y.C.; and Nair, S. Thermal Properties and Lattice Dynamics of Polycrystalline MFI Zeolite Films. *Nanoscale and Microscale Thermophysical Engineering*, 10, 2006: 321–331.

[183] Chen, C.Y. and Kopelevich, D.I. Phonon Interactions in Zeolites Mediated by Anharmonicity and Adsorbed Molecules. *Mol. Sim.*, 34(2), 2008: 155–167.

[184] McGaughey, A.J.H. and Kaviany, M. Thermal Conductivity Decomposition and Analysis Using Molecular Dynamics Simulations. Part I. Lennard-Jones Argon. *Int. J. Heat Mass Transfer*, 47, 2004: 1783–1798.

[185] McGaughey, A.J.H. and Kaviany, M. Thermal Conductivity Decomposition and Analysis Using Molecular Dynamics Simulations: Part II. Complex Silica Structures. *Int. J. Heat Mass Transfer*, 47, 2004: 1799–1816.

[186] MÜLLER-PLATHE, F. A Simple Nonequilibrium Molecular Dynamics Method for Calculating the Thermal Conductivity. *J. Chem. Phys.*, 106, 1997: 6082–6085.

[187] LOU, T. and LLOYD, J.R. Non-Equilibrium Molecular Dynamics Study of Thermal Energy Transport in Au-SAM-Au Junctions. *Int. J. Heat Mass Transfer*, 53, 2010: 1–11.

[188] REITH, D.; MÜLLER-PLATHE, F.; RYCKAERT, J.P.; and BELLEMANS, A. On the Nature of Thermal Diffusion in Binary Lennard-Jones Liquids. *J. Chem. Phys.*, 112(5), 2000: 2436–2444.

[189] BORDAT, P.; REITH, D.; and MÜLLER-PLATHE, F. The Influence of Interaction Details on the Thermal Diffusion in Binary Lennard-Jones Liquids. *J. Chem. Phys.*, 115, 2001: 8978–8982.

[190] TERAO, T.; LUSSETTI, E.; and MÜLLER-PLATHE, F. Nonequilibrium Molecular Dynamics Methods for Computing the Thermal Conductivity: Application to Amorphous Polymers. *Phys. Rev. E*, 75(5), 2007: 057701.

[191] LUSSETTI, E.; TERAO, T.; and MÜLLER-PLATHE, F. Nonequilibrium Molecular Dynamics Calculation of the Thermal Conductivity of Amorphous Polyamide-6,6. *J. Phys. Chem. B*, 111, 2007: 11516–11523.

[192] MÜLLER, T.J. and MÜLLER-PLATHE, F. Heat Transport Through a Biological Membrane—an Asymmetric Property? Technical Issues of Nonequilibrium Molecular Dynamics Methods. *International Journal of Quantum Chemistry*, 111, 2011: 1403–1418.

[193] INZOLI, I.; SIMON, J.M.; BEDEAUX, D.; and KJELSTRUP, S. Thermal Diffusion and Partial Molar Enthalpy Variations of *n*-Butane in Silicalite-1. *J. Phys. Chem. B*, 112(47), 2008: 14937–14951.

[194] NIETO-DRAGHI, C. and AVALOS, J.B. Non-Equilibrium Momentum Exchange Algorithm for Molecular Dynamics Simulation of Heat Flow in Multicomponent Systems. *Mol. Phys.*, 101, 2003: 2303–2307.

[195] Demontis, P.; Suffritti, G.B.; Quartieri, S.; Fois, E.S.; and Gamba, A. Molecular Dynamics Studies on Zeolites. 3. Dehydrated Zeolite A. *J. Phys. Chem.*, 92, 1988: 867–871.

[196] Griesinger, A.; Spindler, K.; and Hahne, E. Measurements and Theoretical Modelling of the Effective Thermal Conductivity of Zeolites. *Int. J. Heat Mass Transfer*, 42, 1999: 4363–4374.

[197] Inzoli, I. *Coupled Transports of Heat and Mass at the Surface of and Inside Silicalite*. Ph.D. thesis, Norwegian University of Science and Technology, 2008.

[198] Dunne, J.A.; Mariwala, R.; Rao, M.; Sircar, S.; Gorte, R.J.; and Myers, A.L. Calorimetric Heats of Adsorption and Adsorption Isotherms. 1. O_2, N_2, Ar, CO_2, CH_4, C_2H_6, and SF_6 on Silicalite. *Langmuir*, 12, 1996: 5888–5895.

[199] Langmuir, I. The Adsorption of Gases on Plane Surfaces of Glass, Mica and Platinum. *J. Am. Chem. Soc.*, 40(9), 1918: 1361–1403.

[200] Ge, J.; Kjelstrup, S.; Bedeaux, D.; Simon, J.M.; and Rousseau, B. Transfer Coefficients for Evaporation of a System with a Lennard-Jones Long-Range Spline Potential. *Phys. Rev. E*, 75, 2007: 061604.

[201] Kjelstrup, S.; Bedeaux, D.; Inzoli, I.; and Simon, J.M. Criteria for Validity of Thermodynamic Equations From Non-Equilibrium Molecular Dynamics Simulations. 33, 2008: 1185–1196.

[202] Taylor, R. and Krishna, R. *Multicomponent Mass Transfer*. John Wiley and Sons, New York, 1993.

Summary

In this thesis, the equilibrium and non-equilibrium thermodynamic description of heterogeneous systems is studied. As a model system the zeolite silicalite-1 was considered. The external surface was defined as a Gibbs surface. Molecular simulation techniques both at equilibrium (Molecular Dynamics, Monte Carlo) and non-equilibrium (non-equilibrium Molecular Dynamics) were used to determine surface pure component adsorption isotherms and mixture adsorption isotherms for the external surface. Non-equilibrium Molecular Dynamics simulations were used to to determine the thermal conductivities of zeolite frameworks.

In Chapter 2, a finite-size scaling method to compute thermodynamic factors and partial molar enthalpies in the thermodynamic limit from small scale subsystems was presented. The new method was also used to determine the Kirkwood-Buff (KB) coefficients for mixtures of Weeks-Chandler-Anderson (WCA) particles. The method turns out to be a powerful tool for determination of KB coefficients, especially at high densities. Inherent problems with integrating the pair correlation function (that are well-known from literature) are avoided. For anisotropic systems, there was a clear dependence of all properties on the structure of the system, *e.g.* for argon in silicalite-1 zeolite, the shape of the small subvolume must reflect the shape of the structure unit cell.

In Chapter 3, a mixture adsorption model (Ideal Adsorbed Solution Theory, IAST) was tested for adsorption of ethane and propane on the external surface of silicalite-1. The external surface can be a significant barrier to transport of heat and mass from a gas phase and into the zeolite phase. IAST significantly lowers the need for determining mixture adsorption isotherms, since predictions can be made from pure component isotherms. Pure component- and mixture isotherms

were determined using Grand-Canonical Monte Carlo (GCMC) simulations. Surface excess adsorption isotherms are calculated, and these shows a clear negative excess adsorption for low pressures. This is an indication that the surface is a significant barrier to transport of mass and heat. The IAST offers a simple and efficient way to obtain quantitative surface adsorption of the particular hydrocarbon mixture on the silicalite-1 surface. Our simulations indicate that the adsorbed phase behaves ideally at ambient temperature, and pressures below 10^6 Pa.

In Chapter 4, the adsorption of argon on external zeolite surfaces, modelled as zeolite nano-sheets, is studied. Surface adsorption isotherms obtained from simulations were compared with experimental results. The adsorption isotherms from experiments and simulations are comparable, even though the simulation results are systematically lower than experimental results for pressures below 10^4 Pa. As found in Chapter 3, the surface excess adsorption are negative for reasonable low pressures, typically below 10^4 Pa. Capillary condensation can be observed for layered nanosheet structures.

The thermal conductivity of zeolites was calculated using non-equilibrium molecular dynamics simulations in combination with the computationally efficient Demontis force field. This is reported in Chapter 5. The thermal conductivity was determined for different crystallographic directions, for zeolites with different loadings of *n*-hexane and argon. The adsorption of molecules in the system had little effect on the overall thermal conductivity. We found significant finite-size effects in the thermal conductivity. Using a second order expansion in the inverse system size, we were able to correct for finite-size effects. The thermal conductivities of typical zeolites are found to vary between 0.6 $W\,m^{-1}\,K^{-1}$, and 4 $W\,m^{-1}\,K^{-1}$. There were significant differences in the thermal conductivity in different crystallographic directions. For the FER-type framework, the thermal conductivity was three times higher in the crystallographic z-direction than in the x-direction. The high resistance can be related to the low number of silicon-oxygen bonds between or within unit cells. This was clear in the FER-type framework, where distinct steps in the temperature profile were observed. We could not observe a straightforward relation between unit cell properties and the thermal conductivity.

In Chapter 6, we derived a simple model for transport of *n*-butane across silicalite-1 interface using non-equilibrium thermodynamics. The model included the coupling of heat- and mass transfer at the surface of the zeolite. We found that

the transport was not well described using Fourier's and Fick's law in combination with the energy balance. The model shows the importance of treating the surface as a separate thermodynamic system.

The transport of heat and mass across the external surface of zeolites can be severely hampered by the surface itself. Resistances to transport can be related to the low surface excess density at the surface. Mixture adsorption isotherms on the surface are found to behave ideally, the same way as in bulk zeolite crystals. For transport across membranes, the resistance on the surface can be significant, and the thermal effects can be so large that they should not be neglected. For future work, the surface texture, and effect of surface groups should be studied closer. Especially transport of CO_2, water, and alcohols can be strongly effected by electrostatic interactions with OH-groups at the external zeolite surface, or other groups located on the external zeolite surface. This would require a force field parametrized to describing these interactions. The finite-size scaling method presented in Chapter 2 have proven to be a valuable asset for calculating Kirkwood-Buff integrals, and partial molar quantities, also directly from anisotropic systems. The application of this method to the external surface of zeolites could help in determining heats of adsorption, and transport properties along the surface.

Samenvatting

In dit proefschrift wordt de beschrijving van heterogene systemen volgend uit evenwicht- en niet-evenwicht thermodynamica bestudeerd. Als modelsysteem wordt het zeoliet silicalite-1 beschouwd. Het externe oppervlak is gedefinieerd als Gibbs-oppervlak. Moleculaire simulatie technieken zowel in evenwicht (Moleculaire Dynamica, Monte Carlo) en niet-evenwicht (niet-evenwicht Moleculaire Dynamica) zijn gebruikt om oppervlakte-adsorptie- en mengseladsorptie-isothermen te bepalen voor het externe oppervlak.

Als eerste belangrijke resultaat wordt in Hoofdstuk 2 een 'finite-size' methode gepresenteerd om de thermodynamische factor en partiële molaire enthalpie in de thermodynamische limiet te berekenen doormiddel van fluctuaties in een klein subsysteem. Deze nieuwe methode is ook gebruikt om Kirkwood-Buff (KB) coëfficiënten te berekenen voor mengsels bestaande uit Weeks-Chandler-Anderson deeltjes. Vooral bij hoge dichtheid blijkt de methode een krachtig hulpmiddel te zijn voor het bepalen van KB coëfficiënten. Inherente problemen met het integreren van de paarcorrelatie-functie over het volume (die welbekend zijn uit de literatuur) worden hiermee vermeden. Voor anisotrope systemen blijkt er een duidelijke afhankelijkheid van alle eigenschappen van de vorm van het subsysteem te zijn. Bijvoorbeeld, voor Argon in silicalite-1 zeoliet moet de vorm van het subvolume de vorm van de eenheidscel reflecteren.

In Hoofdstuk 3 wordt een mengseladsorptiemodel (Ideal Adsorbed Solution Theory, IAST) getest voor de adsorptie van ethaan en propaan op het externe oppervlak van silicalite-1. Het externe oppervlak kan een aanzienlijke barrière zijn voor het transport van warmte en massa vanuit een gasfase naar de zeolietfase. Dit model vermindert de behoefte aan het bepalen van mengselisothermen aangezien

voorspellingen voor het mengsel gedaan kunnen worden aan de hand van adsorptie isothermen van de pure componenten. Deze isothermen van de pure componenten zijn bepaald met behulp van Grand-Canonical Monte Carlo (GCMC) simulaties. De berekende oppervlakte-exces-adsorptie-isothermen hebben een negatieve waarde bij lage druk. Dit is een indicatie dat het oppervlak een significante barrière vormt voor het transport van warmte en massa. De IAST biedt een makkelijke en efficiënte manier om kwantitatieve resultaten te verkrijgen voor de adsorptie van het beschouwde koolwaterstofmengsel op het silicalite-1 oppervlak. Onze simulaties tonen aan dat de geadsorbeerde fase zich ideaal gedraagt bij de omgevingstemperatuur en een druk lager dan 10^6 Pa.

In Hoofdstuk 4 wordt de adsorptie van Argon op een zeoliet oppervlak (gemodelleerd als zeoliet nano-sheets) bestudeerd. Oppervlakte-adsorptie-isothermen verkregen vanuit simulaties worden vergeleken met experimentele resultaten. De adsorptie-isothermen zijn vergelijkbaar, alhoewel de simulatieresultaten systematisch lager uitvallen voor drukken lager dan 10^4 Pa. Zoals eerder gevonden in Hoofdstuk 3 blijken de oppervlakte-exces-adsorptie-isothermen een negatieve waarde te hebben voor redelijk lage druk (typisch lager dan 10^4 Pa). Capillaire condensatie kan geobserveerd worden voor gelaagde nano-sheet structuren.

De warmtegeleiding van zeolieten is berekend aan de hand van niet-evenwicht moleculaire dynamica simulaties gecombineerd met het efficiënt te gebruiken Demontis force field. Dit wordt gepresenteerd in Hoofdstuk 5. Voor zeolieten met een verschillende lading van *n*-hexaan en argon is de warmtegeleiding in de verschillende kristallografische richtingen van het zeoliet. De adsorptie van moleculen in het systeem heeft weinig effect op de totale warmtegeleiding. We hebben significante finite-size effecten gevonden voor de warmtegeleiding. Door gebruik te maken van een tweede-orde expansie in de inverse van de systeemgrootte is gecorrigeerd voor deze effecten. De warmtegeleidingscoëfficiënt van typische zeolieten varieert tussen 0.6 $\mathrm{W\,m^{-1}\,K^{-1}}$, en 4 $\mathrm{W\,m^{-1}\,K^{-1}}$. Er zijn significante verschillen in warmtegeleiding in de verschillende kristallografische richtingen gevonden. Voor het FER-type framework was de warmtegeleiding drie keer hoger in de z-richting dan in de x-richting. De hoge weerstand kan gerelateerd worden aan het lagere aantal chemische bindingen tussen- of binnen eenheidscellen. Dit is vooral duidelijk in het FER-type framework, waar duidelijke stapjes in het temperatuurprofiel worden waargenomen. Desalniettemin is er geen voor de hand liggende relatie tussen de

eigenschappen van de eenheidscel en warmtegeleidingscöefficiënt gevonden.

In Hoofstuk 6 wordt niet-evenwicht thermodynamica gebruikt om een simpel model af te leiden voor het transport van *n*-butaan over een silicalite-1 grensvlak. In het model wordt de koppeling van warmte- en massatransport over het zeolietoppervlak meegenomen. Er is gevonden dat het massatransport niet goed beschreven wordt door een combinatie van de wetten van Fick- en Fourier en de energiebalans. Dit model toont aan dat het oppervlak als apart thermodynamisch systeem beschouwd moet worden.

Het transport van warmte en massa over het externe oppervlak van zeolieten kan zwaar gehinderd worden door het oppervlak zelf. Weerstand tegen transport kan gerelateerd worden aan de lage oppervlakte-exces-dichtheid. Er is gevonden dat, net zoals in macroscopische zeolietkristallen, de adsorptie-isothermen van mengsels aan het oppervlak zich ideaal gedragen. Voor het transport van massa en warmte door membranen kan de weerstand aan het oppervlak significant zijn. Warmte-effecten kunnen zo groot worden dat ze niet meer te verwaarlozen zijn. Voor toekomstig werk zou het nuttig zijn om de textuur van het oppervlak en het effect van verschillende chemische groepen op het oppervlak nader te bestuderen. Vooral het transport van CO_2, water en alcoholen kan mogelijk sterk beïnvloed worden door elektrostatische interacties met OH-groepen- of andere groepen op het externe zeolietoppervlak. Om dit te bestuderen zou een force field geparameterizeerd voor het beschrijven van dergelijke interacties nodig zijn. De finite-size methode die is gepresenteerd in Hoofdstuk 2 is een waardevol hulpmiddel gebleken voor het berekenen van Kirkwood-Buff integralen en de partiële molaire enthalpie, ook direct vanuit anisotrope systemen. Het toepassen van deze methode op het externe zeolietoppervlak zou kunnen helpen in het bepalen van de enthalpie van adsorptie en transporteigenschappen aan het oppervlak.

Curriculum Vitae

The author of this work was born in the winter of 1984, in Kristiansund, Norway. He started on the path to his academic career by enrolling at the Norwegian University of Science and Technology in Trondheim, August 2004, the goal being a Master of Science in Chemical Engineering. He graduated in August 2009. During the last two years in Trondheim, he worked in the group of Non-equilibrium thermodynamics, under the supervision of Prof. Signe Kjelstrup. From January 2010 until end of 2013 he was working on the Ph.D. degree in the Engineering Thermodynamics group under the supervision of Prof. Thijs J. H. Vlugt and Prof. Signe Kjelstrup. The focus of the Ph.D. study has been molecular simulations, small systems thermodynamics, and transport through surfaces.

Publications by the Author

Publications included in this thesis are emphasis with an obelisk.

1. Schnell, S. K., Vlugt, T. J. H., Simon, J.-M., Bedeaux, D. and Kjelstrup, S.; Thermodynamics of a Small System in a μT Reservoir. *Chem. Phys. Lett.*, 504 (2011) 199–201.

2. †Schnell, S. K., Liu, X., Simon, J.-M., Bardow, A., Bedeaux, D., Vlugt, T. J. H. and Kjelstrup, S.; Calculating Thermodynamic Properties from Fluctuations at Small Scales. *J. Phys. Chem. B*, 115 (2011) 10911–10918.

3. Liu, X., Schnell, S. K., Simon, J.-M., Bedeaux, D., Kjelstrup, S., Bardow, A. and Vlugt, T. J. H.; Fick Diffusion Coefficients of Liquid Mixtures Directly Obtained From Equilibrium Molecular Dynamics. *J. Phys. Chem. B*, 115 (2011) 12921–12929.

4. †García-Pérez, E., Schnell, S. K., Castillo, J. M., Calero, S. Kjelstrup, S., Dubbeldam, D. and Vlugt, T. J. H.; External Surface Adsorption on Silicalite-1 Zeolite Studied by Molecular Simulation. *J. Phys. Chem. C*, 115 (2011) 15355–15360.

5. Skorpa, R., Voldsund, M., Takla, M., Schnell, S. K., Bedeaux, D., and Kjelstrup, S.; Assessing the Coupled Heat and Mass Transport of Hydrogen Through a Palladium Membrane. *J. Mem. Sci.*, 394–395 (2012) 131–139.

6. Schnell, S. K., Vlugt, T. J. H., Simon, J.-M., Bedeaux, D., and Kjelstrup, S.; Thermodynamics of Small Systems Embedded in a Reservoir: a Detailed Analysis of Finite Size Effects. *Mol. Phys.*, 110 (2012) 1069–1079.

7. LIU, X., MARTIN-CALVO, A., MCGARRITY, E. S., SCHNELL, S. K., CALERO, S., SIMON, J.-M., BEDEAUX, D., KJELSTRUP, S., BARDOW, A., AND VLUGT, T. J. H.; Fick Diffusion Coefficients in Ternary Liquid Systems From Equilibrium Molecular Dynamics Simulations. *Ind. Eng. Chem. Res.*, 51 (2012) 10247–10258.

8. KRÜGER, P., SCHNELL, S. K., BEDEAUX, D., KJELSTRUP, S. VLUGT, T. J. H., AND SIMON, J.-M.; Kirkwood-Buff Integrals for Finite Volumes. *J. Phys. Chem. Lett.*, 4 (2013) 235–238.

9. BALAJI, S. P., SCHNELL, S. K., MCGARRITY, E. S., AND VLUGT, T. J. H.; A Direct Method for Calculating Thermodynamic Factors for Liquid Mixtures Using the Permuted Widom Test Particle Insertion Method. *Mol. Phys.*, 111 (2013) 285–294.

10. BALAJI, S. P., SCHNELL, S. K., AND VLUGT, T. J. H.; Calculating Thermodynamic Factors of Ternary and Multicomponent Mixtures Using the Permuted Widom Test Particle Insertion Metod. *Thero. Chem. Acc.*, 132 (2013) 1333.

11. †SCHNELL, S. K., AND VLUGT, T. J. H.; Thermal Conductivity in Zeolites Studied by Non-Equilibrium Molecular Dynamics Simulations. *Int. J. Thermophys.*, 34 (2013) 1197–1213.

12. LIU, X., SCHNELL, S. K., KRÜGER, P., SIMON, J.-M., VLUGT, T. J. H., BEDEAUX, D., AND KJELSTRUP, S.; Diffusion Coefficients From Molecular Dynamics Simulations in Binary and Ternary Mixtures. *Int. J. Thermophys.*, 34 (2013) 1169–1196.

13. †SCHNELL, S. K., VLUGT, T. J. H. AND KJELSTRUP, S.; *Handbook on Membrane Reactors*, vol. 1, Chapter: 'Non-Equilibrium Thermodynamics for the Description of Transport of Heat and Mass Across a Zeolite Membrane', Woodhead, 2013, pp. 627–646.

14. SCHNELL, S. K., ENGLEBIENNE, P., SIMON, J.-M., KRÜGER, P., BALAJI, S. P., KJELSTRUP, S., BEDEAUX, D., BARDOW, A., AND VLUGT, T. J. H.; Kirkwood-Buff Theory of Individual Ionic Species in Salt Solutions. *Chem. Phys. Lett.*, 582 (2013) 154–157.

Acknowledgement

Working on a Ph.D.-thesis is interesting, at times confusing, and sometimes really difficult. I would like to thank my promotors Prof. Thijs J. H. Vlugt and Prof. Signe Kjelstrup for their help with this thesis. I appreciate the chance to work together with you, and I have learned a great many things from you in the four years leading up to this dissertation.

A special thanks as well to Dick Bedeaux and Jean-Marc Simon. The effort to understand small systems has been one of the most interesting intellectual challenges I have encountered. Hopefully, we have just found the first of many new advances in the field of small systems, and small systems thermodynamic.

Finally, I would like to thank my many colleagues, both former and present. Without discussions (especially non-work related discussions) and regular coffee breaks, the office would be a much duller place.